Structural and functional studies of a ferredoxin/flavodoxin $NADP^+$-oxidoreductase mutant from *Bacillus cereus.*

Anne Kristine Rugtveit

Master thesis in Molecular Biology and Biochemistry

30 credits

Department of Biosciences

Faculty of Mathematics and Natural Sciences

UNIVERSITY OF OSLO

June 2021

Acknowledgements

The laboratory work presented in this thesis has been performed in the laboratory of the Structural Redox Biochemistry group at the Department of Biosciences, University of Oslo.

I am forever thankful to my supervisors Marta Hammerstad and Hans-Petter Hersleth for giving me the opportunity to work and learn in a warm and welcoming environment this spring, and for all the help and guidance they have offered during this project. Their knowledge, availability, kindness, and interest in the project has been critical to my progress and learning, and for this, I am incredibly grateful.

I would also like to thank my dear friends Silje and Nora, for all the encouragement and memories during the past five years, and Sondov, for many hours of laughter and hard work at the laboratory. I am also deeply grateful for all the support provided by Fredrick and my family, who have motivated and supported me through both good and bad times. A special thanks goes to my parents for teaching me the importance of education, hard work, and for encouraging me to be curious and positive, even during stressful times.

Oslo, June 2021

Anne Kristine Rugtveit

Abstract

The reduction of ribonucleotides to deoxyribonucleotides by ribonucleotide reductase (RNR) is of importance to all organisms that require building blocks for DNA replication and repair. In the pathway leading to activation of the class Ib RNRs in *Bacillus cereus*, the flavodoxin (Fld)-like protein NrdI has proven to be an important reductant, allowing for the assembly of a Mn^{III}_2-tyrosyl radical (Y•) cofactor in the NrdF subunit of the class Ib RNRs, before subsequent reduction of ribonucleotides. Three ferredoxin/flavodoxin $NADP^+$-oxidoreductases (FNRs) identified in *B. cereus* has been found to reduce NrdI in this pathway.

Of the identified FNRs (FNR1-3) in *B. cereus*, FNR2 has previously proven to be the most efficient reductant of Flds and Fld-like NrdI. FNR1 and FNR2 differ in an active site residue stacking opposite the FAD cofactor, with histidine being the FAD-stacking residue in FNR2, while FNR1 has valine in this position. This study has been based on the investigation of the structure and activity of a cross-mutation between the two FAD-stacking residues found in FNR1 and FNR2. The FNR2 His326Val mutated protein ($FNR2_{mut}$) was expressed and purified before performing activity measurements and solving the $FNR2_{mut}$ structure by X-ray crystallography. In this study, the main aim has been to investigate if the different FAD-stacking residues in FNR1 and FNR2 are the reason for the difference in their catalytical activity. The results obtained in this study indicate that other structural features, in addition to the FAD-stacking residue, most likely play a role in the activity of the FNR1 and FNR2 enzymes in *B. cereus*.

In addition to obtaining kinetic parameters providing information about the activity of the $FNR2_{mut}$ enzyme, interesting findings has been made when solving the mutant structure. Although different domain rotations have been observed for this class of FNRs in previous studies, this study presents a new type of domain rotation, where the $FNR2_{mut}$ structure constitutes an asymmetric dimer, accompanied by the loss of the FAD-cofactor in one monomer.

Table of contents

1. Introduction

1.1 *Bacillus cereus* ribonucleotide reductase activation system

All organisms require deoxyribonucleotides for DNA replication and repair[1]. Enzymes known as ribonucleotide reductases (RNRs) catalyse the reduction of ribonucleotides to generate deoxyribonucleotides and are therefore crucial for obtaining DNA building blocks [2, 3]. RNRs are divided into three classes based on the identity of their radical initiator subunit, which is required for reduction of nucleotides. All these classes of RNRs make use of an active site cysteinyl radical (S•) to conduct the catalysis but show differences in identity of metallocofactors and structures [2, 4]. The most studies RNRs, referred to as class I RNRs, contains two subunits: the α_2 subunit known as the catalytical subunit, and the β_2 subunit that contains, in most cases, the metallocofactor for initiation of nucleotide reduction. Class I RNRs are further subdivided into subclasses Ia, Ib, Ic, Id, and Ie, based on their cofactors. Class Ia contains an $Fe^{III}Fe^{III}$-tyrosyl radical (Y•), class Ib has a dimanganese $Mn^{III}Mn^{III}$-Y•, class Ic is proposed to contain a $Mn^{IV}Fe^{III}$ cofactor, class Id a $Mn^{III}Mn^{IV}$ cofactor, and class Ie is metal free with a 3,4-dihydroxyphenylalanine radical (DOPA•) for nucleotide reduction. RNR classes II and III enzymes show structural similarities to the class I enzymes but differ in terms of allosteric regulation, oxygen dependency, sequence similarity and type of cofactor utilized to generate the S• [1-5]. A common feature in all RNRs is the involvement of a radical initiator in the oxidation of an active site cysteine, to generate the S•, which will further initiate a radical mediated reduction of the ribonucleotides. In the case of classes Ia and Ib RNRs, the metallocofactor, or metal centre, is the site for generation of a Y• upon reaction with dioxygen. This radical is further shuttled through the catalytic subunit (α_2) to generate the S• that is essential to reduce ribonucleotides [1, 3, 4].

The pathway leading to activation of the oxygen-dependent class Ib RNR have been studied in several bacterial species, including *Bacillus cereus* (*B. cereus*). The class Ib RNRs has shown to function with both Fe^{III}_2-Y• and Mn^{III}_2-Y• cofactors, where the former can self-assemble from Fe^{2+} ions and O_2, but the latter cannot. The manganese form of the metallocofactor is more active than the diferric form, and studies have shown that the Mn^{III}_2 cofactor in many cases is the one which is bound to the β_2 subunit when expressed in bacteria [6]. To utilize the dimanganese metallocofactor, and activate the class Ib RNR, the formation of active Mn^{III}_2-Y• cofactor in the β_2 subunit, called NrdF, is essential. The assembly of this active cofactor is made

possible by the action of NrdI, which is a flavodoxin (Fld)-like protein found in the RNR operon in bacteria encoding the class Ib RNR [1, 3, 7].

The Fld-like protein NrdI has been found in all organisms that have the class Ib RNR [1]. NrdI uses a flavin mononucleotide (FMN) cofactor, and this cofactor acts as a reductant in the pathway leading to activation of class Ib RNR. The reduced form of NrdI ($NrdI_{hq}$) reacts with O_2 to give superoxide or O_2• and the reactive oxygen species is further channelled from NrdI to the dimanganese metal cluster in the NrdF subunit of the RNR, a process that is required for the metallocofactor oxidation and generation of the Mn^{III}_2-Y• [1, 3, 7]. For NrdI to be able to reduce O_2 in this activation pathway, NrdI itself must be in the reduced state. The search for a potential NrdI reductase has led to the identification of three different ferredoxin/flavodoxin $NADP^+$-oxidoreductases (FNRs) in *B. cereus* [3].

1.2 Electron transfer proteins

Oxidation-reduction reactions (redox reactions) are processes involving transfer of electrons, oxygen atoms or hydrogen atoms, and are accompanied by a change in the oxidation number of the chemical species involved [8]. Electron transfer reactions between proteins are important in many biological processes such as photosynthesis, respiration, and DNA repair, and many energy transduction pathways depend on shuttling of electrons, mediated by different proteins [9-11].

Electron transfer proteins or redox proteins, with RNRs and their redox partners being an example, are involved in redox reactions and transfer of electrons between redox enzymes. Redox proteins contain redox-active cofactors, or redox sites, often localized close to the protein surface, where some common examples are iron-sulfur clusters, hemes, flavins and quinones. These redox sites facilitate transfer of electrons between redox centres of different proteins, and electron flow between redox proteins is mediated *via* these catalytic sites connected by redox chains [10, 12].

Redox reactions between proteins are mediated by protein-bound cofactors or via amino acid residues in the protein, or in many cases, both. The redox active amino acids involved in electron transfer are tyrosine (Tyr), tryptophane (Trp), and cysteine (Cys), and these amino acids can form one-electron oxidized radicals and serve as electron-transfer intermediates. [9, 13-15]. Electron transfer between proteins mostly occur in the range of 4 Å to 14 Å, and these reactions typically occur between cofactors bound to the proteins [16]. A free electron localized on a redox centre has a wavefunctions, and this wavefunction extends in all directions beyond

the cofactor. As these wavefunctions come in contact with other redox centres nearby, the electron is allowed to tunnel between the redox centres with a rate which decreases exponentially the distance between the centres [14, 15].

Electron transfer reactions are facilitated by complex formation between proteins prior to electron transfer, and the rate of electron transfer between proteins is an important characteristic. The rate of electron transfer is determined by the rate constant, which is dependent on a prefactor A and the activation energy (ΔG˚). This prefactor A measures the orbital overlap (wavefunction) between the electron donor and electron acceptor within the protein complex and will decrease exponentially with distance. As the free energy of the reaction increases, so does the rate of electron transfer, and the rate of electron transfer reaches a maximum when ΔG˚ equals the reorganization energy (λ). The driving force of the reaction also depends on the redox centre, while the reorganization energy depends on the structure of the protein and the electron transfer complex [8, 17, 18].

1.3 Flavoproteins

Flavoproteins are a common type of redox proteins that catalyse redox reactions by utilizing flavin cofactors. FMN or flavin adenine dinucleotide (FAD) cofactors are the most common flavins in flavoproteins, with FAD being utilized by the majority (75%) of all flavoenzymes rather than FMN (figure 1.1). Flavoproteins, or flavoenzymes, catalyse a wide range of reactions and have central roles in many biological activities, including aerobic metabolism, photosynthesis, apoptosis, oxygen activation and DNA repair [15, 19, 20]. The FMN and FAD cofactors in flavoproteins are normally non-covalently bound to the apoprotein in a Rossmann-like fold [19, 21, 22].

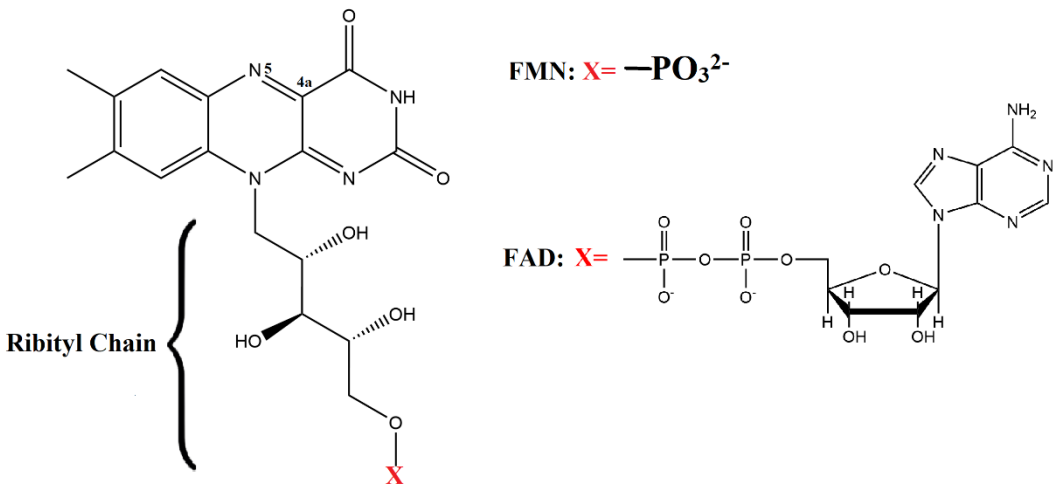

Figure 1.1. Chemical structure of FMN and FAD cofactors

The precursor of flavin is riboflavin (vitamin B_2), and this yellow vitamin is synthesized by many bacteria and plants before converted to FAD or FMN [15, 21]. In addition to a ribityl chain, both FMN and FAD cofactors have a redox active isoalloxazine ring system, which is the basis of the biochemical utilization of these cofactors. The reactivity of the isoalloxazine ring system is associated with the reactive atoms N5 and C4a (figure 1.1), and this makes the flavins one of the most versatile cofactors, being capable of undergoing reversible reduction and accept one or two electrons. By virtue of the possible various oxidation states of the flavins, they are said to sit in crossroads of one- and two-electron chemistry [15, 19, 23].

Due to the isoalloxazine ring system being able to transfer both one and two electrons, flavoproteins can exist in three different oxidation states. These states are referred to as oxidised (ox), one-electron reduced semiquinone (sq), and two-electron reduced hydroquinone (hq) states [20]. The different oxidation states of the isoalloxazine ring are shown in figure 1.2.

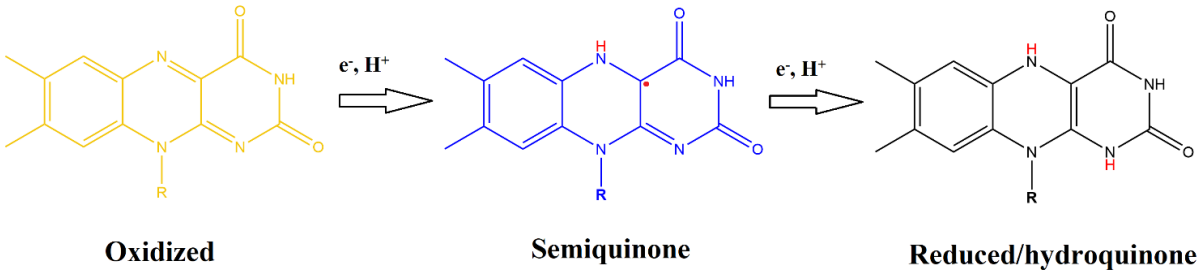

Figure 1.2. Different redox states of the isoalloxazine ring system

1.4 Flavodoxins

Electron-transfer proteins known as Flds were discovered in cyanobacteria in the 1960s, where they could replace the iron-containing proteins known as ferredoxins (Fds) in several reactions [24]. Flds are small electron-shuttling flavoproteins with a non-covalently bound FMN cofactor that functions as the redox-active protein component. These small proteins are useful electron donors for many different bacterial redox enzymes, such as RNR, nitric oxide synthase and biotin synthase [16, 24].

With a few exceptions in eukaryotic algae, flavodoxins are mainly found in bacteria and they are widely distributed among different bacterial phyla. Despite being bacterial proteins, some Fld-homologous domains have been discovered in multidomain eukaryotic proteins [24, 25]. Flds are acidic proteins consisting of around 140-180 amino acid residues, and are divided into two classes depending on the presence of a 20-residue loop with unknown function, where

proteins containing this loop are referred to as long-chain Flds, and others as short-chain Flds [24].

Two short-chain Flds known as Fld1 and Fld2, and one Fld-like protein called NrdI, have been identified in *B. cereus* (figure 1.3). Comparing the crystal structures of Fld1 and Fld2 indicates that the Flds are similar in both three-dimensional structure and active site, having a three-layer αβα sandwich consisting of five-stranded β-sheet surrounded by α-helices (Rossmann fold). NrdI, not classified as a Fld, do not share the same sequence similarity with the Flds. A study published by Gudim et al. compared the redox potentials and kinetic parameters of these three flavoproteins in reactions with the three identified Fld/NrdI reductases identified in *B. cereus* called ferredoxin/flavodoxin-$NADP^+$ oxidoreductases (FNRs). The study showed that all three FNRs (FNR1-3) could successively reduce both the Flds and NrdI, but with different rates [3, 16].

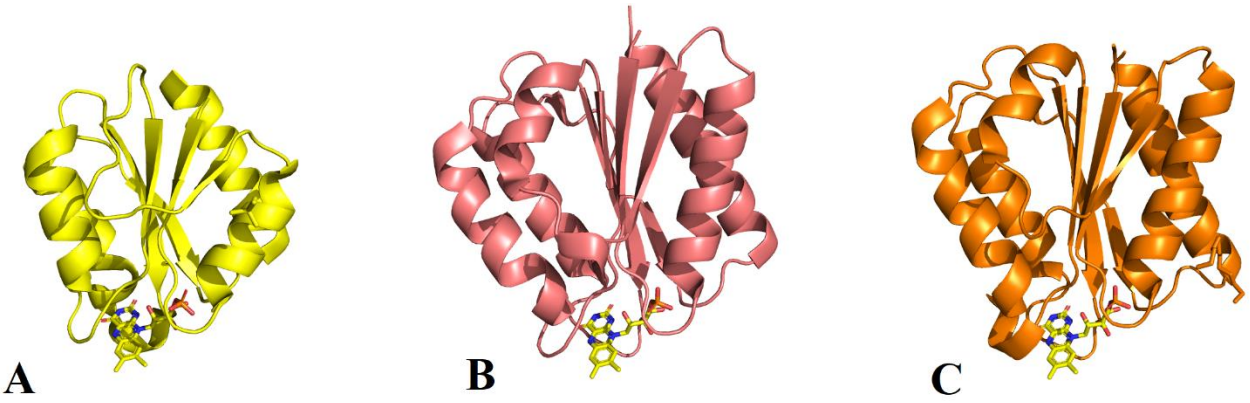

Figure 1.3. Different Fld/Fld-like proteins from *B. cereus*. A) Flavodoxin-like protein NrdI (PDBid:2X2O). B) Fld1 (PDBid:6FSG). C) Fld2 (PDBid:6GAQ).

1.5 Ferredoxin/flavodoxin-$NADP^+$ oxidoreductases (FNRs)

FNRs are FAD-containing flavoenzymes that catalyse reversible transfer of electrons between NADPH and Fd or Fld. [3, 26-28]. FNRs participate in several electron transfer reactions, including electron transfer chains in photosynthesis, detoxification, oxidative stress response and various biosynthetic pathways, and they are found in a wide range of organisms [27-29].

FNRs are normally divided into two different families referred to as plant-type FNRs and glutathione reductase (GR)-like FNRs, which are structurally and phylogenetically unrelated to each other [16, 27]. FNRs of both these families display a two-domain organization, where the active site is at the interface between the two domains, called the FAD-binding domain and the NADPH-binding domain. The FAD-binding domain in plant-type FNRs is formed by the N-

terminal part of the polypeptide chain, while in GR-like FNRs, two discontinuous segments make up the FAD-binding domain [27, 28].

The thioredoxin reductase (TrxR)-like FNRs make up a subfamily of the GR-like FNRs. These enzymes were first isolated from the green sulfur bacterium *Chlorobaculum tepidum*, and later from different bacteria, such as gram-positive *Bacillus subtilis*, thermophile *Thermus thermophilus* and the non-sulfur bacterium *Rhodopseudomonas palstris* [30]. The TrxR-like FNRs share high sequence identity with TrxR, but despite this sequence homology, the TrxR-like FNRs does not have the CXXC catalytic motif essential to TrxR catalysis. For this reason, TrxR-like FNRs are not able to reduce the TrxR substrate thioredoxin (Trx), and thus cannot be classified as TrxRs [3, 16, 29]. TrxR-like FNRs are, like TrxR, homodimeric, which is a contrast to other FNRs who are monomeric with only a few exceptions. The TrxR-like FNR protomers contain two domains which display a Rossmann-like three-layer ββα sandwich nucleotide binding folds for FAD and NADPH. The NADPH-binding domain in the TrxR-like FNRs is connected to the FAD-binding domain by a hinge region of antiparallel β-sheet (figure 1.4). Another feature that is unique for this class of FNRs is the ability of the domains to rotate relative to each other. Domain rotation is also observed during TrxR catalysis, but the domain rotation seen in TrxR-like FNRs are different from the TrxR rotation [16, 22, 27, 29].

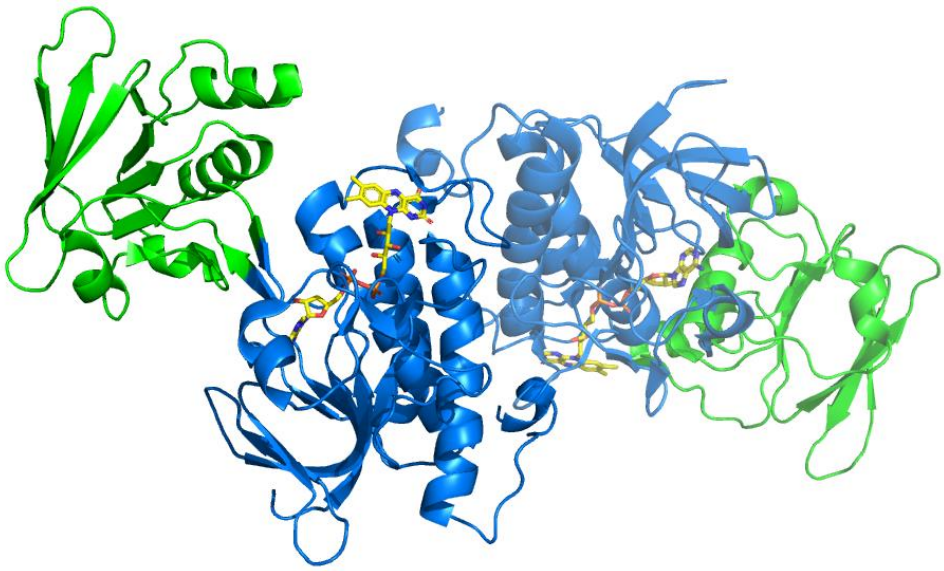

Figure 1.4. TrxR-like FNR2 from *B. cereus* (PDBid:6GAS). NADPH-binding domains shown in green, FAD-binding domains shown in blue. Monomer 1 shown in bright colours, and monomer 2 shown in paler colours. The FAD cofactor is shown in sticks.

1.5.1 FNRs in *B. cereus*:

For NrdI to be able to reduce O_2 in the class Ib RNR activation pathway in *B. cereus*, NrdI itself must be in the reduced state, called the hydroquinone (hq) state. Lofstad et al. published an article in 2016 that aimed to identify potential redox proteins responsible for reduction of NrdI in *B. cereus*, so that NrdI can further generate activated oxygen in the RNR activation pathway. In this study, three potential Fld reductases were identified. The *B. cereus* genome was found to contain three homologous proteins, called FNR1 (BC0385), FNR2 (BC4926) and FNR3 (BC1495), that could successively reduce the Fld-like NrdI, but with different reduction rates. The identified FNRs in *B. cereus* share sequence identity with TrxR, and therefore belongs to the class of TrxR-like FNRs. The three FNRs also share sequence identity with FNRs in several other organisms, and some known examples are *Bacillus subtilis* YumC, *Bacillus anthracis* FNR2, and *Lactococcus lactis* TrxB2 [3].

Studies on the *B. cereus* FNRs show that all three enzymes can interact with, and reduce, NrdI. Kinetic parameters for the reduction of NrdI, Fld1 and Fld2 with the different FNRs have been obtained and both Flds from *B. cereus*, as well as NrdI, showed higher turnover rates with FNR2 than with FNR1. The FNR2/Fld2 and FNR2/Fld1 pairs was concluded to be the best redox pair of the nine different pairs investigated by Gudim *et. al*., even under aerobic conditions, with 91-fold and 28-fold higher rate than the third most efficient FNR2/NrdI pair. Lofstad et al. concludes that FNR2 is the most efficient redox partner for NrdI in *B. cereus*, with >10-fold and >30-fold higher NrdI reduction rate than FNR1 and FNR3, respectively. FNR3, being a poor Fld- and NrdI-reductase, has recently been shown to catalyse the reduction of oxidized bacillithiol in Firmicutes [31], and will not be discussed further in this thesis [3, 16].

The big differences in both reaction kinetics and redox potentials between the FNRs in *B. cereus* have been investigated to search for features that may explain the results obtained by Gudim et al [16]. In the same study, the crystal structures of FNR1 and FNR2 were compared to identify key differences that may have an impact on the catalytic rate and redox potentials of the two enzymes. From the crystal structures of FNR1 and FNR2 it became clear that the two proteins have crystallized in different conformations (figure 1.5). FNR1 crystallized in a more closed conformation than FNR2, which crystallized in an open conformation. In addition, the NADPH-binding domain of FNR1 is rotated 60˚ relative to the same domain in FNR2.

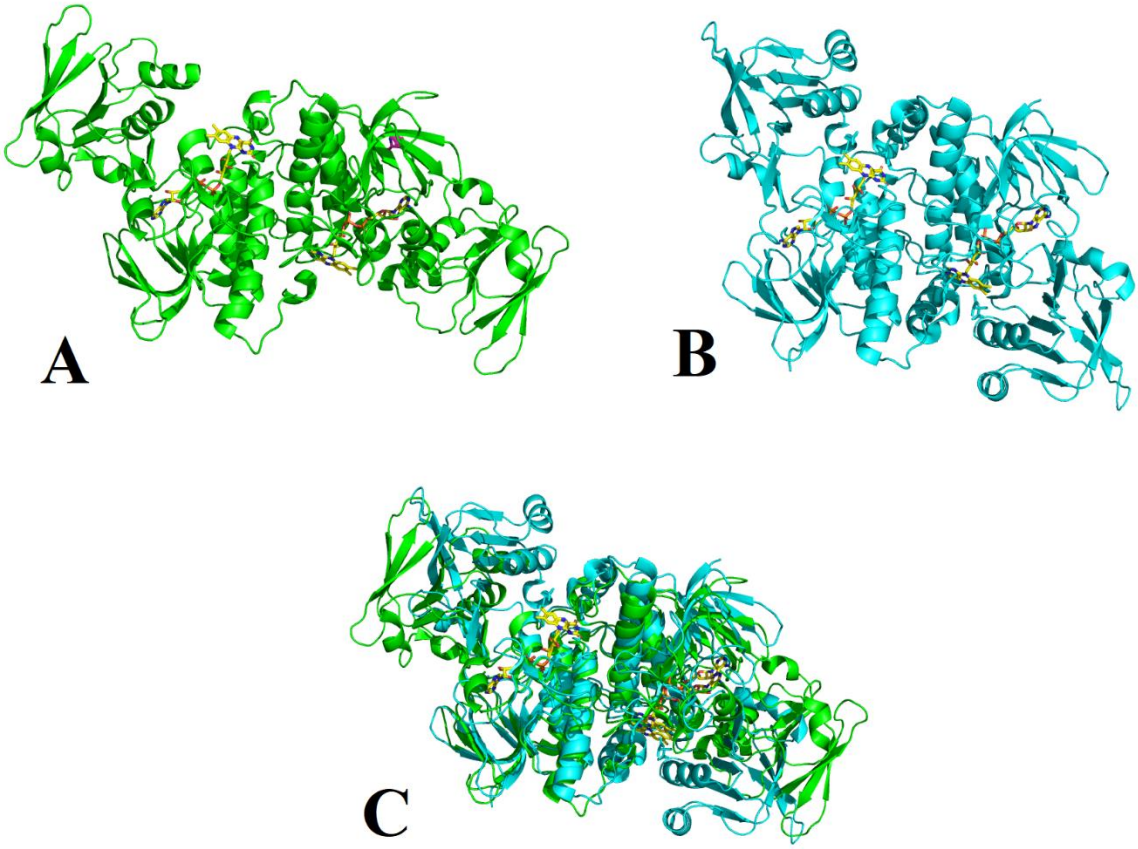

Figure 1.5. Structure of FNR1 (PDBid:6GAR) and FNR2 in *B. cereus.* A) FNR2. B) FNR1. C) Overlay of FNR1 and FNR2 structure.

A domain rotation, although different from what is observed for the *B. cereus* FNR structures, has also been observed in some TrxRs (low M_r TrxR), which can exist in two different conformations, called the flavin-oxidizing (FO) and flavin-reducing (FR) conformation, depending on the FAD oxidation state. [16, 22, 32, 33]. In addition to these open and closed conformations, it has been shown with overlays that TrxR-like FNRs can crystallize in several different conformations. By docking the NADPH-molecule into the structures based on the binding site in *B. subtilis* YumC, neither the closed or open conformations displayed by FNR1 and FNR2 allows for productive hydride transfer [16]. Hydride transfer from NADPH to the FAD-cofactor can occur at distances up to 2 Å, while electron tunneling can occur at distances between 4-14 Å. This is because the protons are more massive than electrons, and require much shorter distances between donor and acceptor [34]. In the structures of FNR1 and FNR2, the NADPH is 10,2 Å and 16,9 Å away from the FAD-cofactor, respectively. These observations suggests that, like for TrxRs, a large-scale conformational change is essential for FAD-reduction by NADPH. Although the closed FNR1 conformation is the one that approaches the

conformation required for hydride transfer, there must still be a conformational change to accommodate the binding of Fld. From the open conformation of FNR2, one can easily see how Fld can fit for productive transfer of electrons, because the Fld docks closer to the FAD-cofactor [16].

Another interesting difference between FNR1 and FNR2, also found by Gudim et al., is the electrostatic surface potentials. Flds are acidic proteins with acidic residues close to the FMN-cofactor, and the FNRs have basic residues with different distributions one the protein surface [16, 24]. FNR1 have small patches of basic residues distributed on the surface while in FNR2, there is one larger basic patch close to the FAD-cofactor. This have been thought to stabilize productive complex formation between FNR2 and the Flds, and may have implications on the higher turnover displayed by FNR2 [16].

Investigations of the conserved residues surrounding the FAD-binding site have led to the discovery of another interesting difference between FNR1 and FNR2 in *B. cereus*. For a long time, it has been thought that three residues in the C-terminal subdomain are conserved in all TrxR-like FNRs. These residues are one aromatic residue (His, Tyr or Phe) and two aliphatic hydroxyl-containing residues (Thr or Ser), and these three residues stabilizes the FAD-cofactor by hydrogen-bonding and π-π interactions [16, 35]. In FNR2, a histidine residue is stacking opposite the FAD on the *re* face (figure 1.6AB), while in FNR1, this aromatic FAD-stacking residue is replaced by valine (figure 1.6A). Furthermore, it was found that this Val residue is conserved in some other FNRs as well. Based on these differences, it has been concluded that FNR1 and FNR2 belong to different classes of FNRs: one where a residue with aromatic character (His, Tyr or Phe) is stacked opposite the FAD-cofactor, and one class where Val is on the FAD *re* face. The latter class of FNRs also have a longer C-terminal helix than the former. This interchange of FAD-stacking residue might give an explanation for the different turnovers displayed by FNR1 and FNR2 [16].

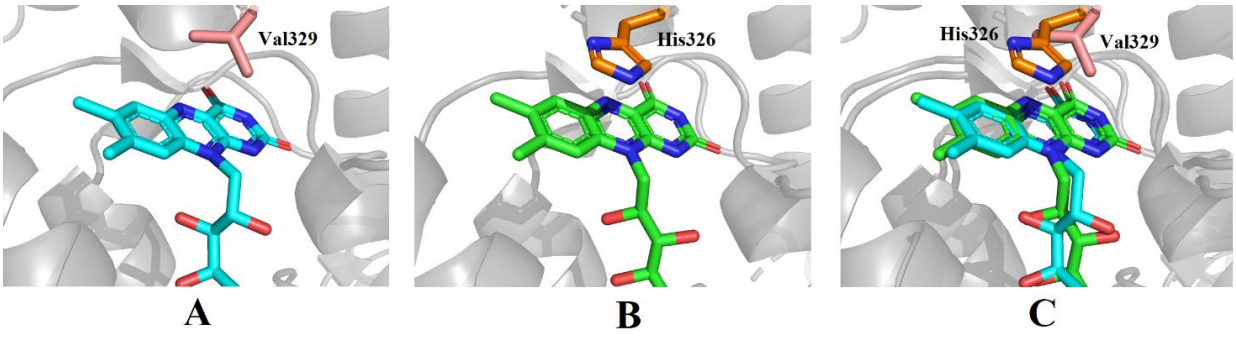

Figure 1.6. The FAD-stacking residue in FNR1 and FNR2. A) FAD and stacking Val329 in FNR1. B) FAD and stacking His326 in FNR2. C) Overlay of FAD cofactor and FAD-stacking residues in FNR1 and FNR2.

1.6 Aim of the study

This project will be based on FNR2 from *B. cereus*, which is a more efficient redox partner for Flds and Fld-like NrdI, than FNR1 and FNR3. The identified conserved aromatic residue (His326) that is stacking opposite the FAD cofactor in the active site of FNR2, is different from FNR1, which has Val in this position [16]. The significance of this amino acid residue for the efficiency of electron transfer in FNR2 will be investigated by making a cross-mutation of this specific residue between FNR2 and FNR1 (His326Val). If this mutation of His326 to Val reduces the activity of FNR2 so that it corresponds to the activity of FNR1, this could give a possible explanation for the difference in the catalytical activity of FNR1 and FNR2 in Fld reduction.

The study will involve transformation of competent *Escherichia coli* (*E. coli*) cells that will be used for overexpression of the FNR2 His326Val mutant protein ($FNR2_{mut}$). The $FNR2_{mut}$ will be purified, and the activity and efficiency of the enzyme will be investigated anaerobically to obtain information about the ability to reduce Fld-like NrdI and Fld1 from *B. cereus*. The resulting kinetic parameters will be used to compare the $FNR2_{mut}$ activity to the wild type FNR1 ($FNR1_{wt}$) and FNR2 ($FNR2_{wt}$) enzymes, and the information obtained in this study will be used to evaluate how the mutation of the active site His326 residue affects the protein's ability to transfer electron in the *B. cereus* RNR activation pathway. In addition, an attempt will be made to crystallize the $FNR2_{mut}$ and solve the structure by X-ray crystallography.

While the main focus of this project will be on the $FNR2_{mut}$ activity and structure, an attempt will also be made to co-crystallize the $FNR1_{wt}$ protein with $NADP^+$ as an additional project, since previous attempts to obtain a FNR1 structure including NADPH has not been successful.

2 Methods

2.1 DNA preparations

In DNA cloning, a gene of interest is inserted into a vector, often a plasmid, to obtain a recombinant DNA molecule. Plasmids are circular DNA molecules that exists naturally in many bacterial species, and often contain genes that gives the host bacteria a useful characteristic. A plasmid contains an origin of replication and can therefore multiply within the cell independently of the bacterial chromosome [36-38]. Vectors can be designed for different purposes and are useful tools in gene cloning. A gene of interest can be cloned into a plasmid vector by using restriction endonucleases and ligases. Restriction endonucleases are bacterial enzymes that cut double-stranded DNA at specific recognition sequences, and this will allow for selection and insertion of new DNA fragments into a specific area in the vector [36, 39]. Plasmid vectors used in gene expression include a promoter system suitable for overexpressing the inserted gene and includes additional genes that confers antibiotic resistance on the host cell that takes up the plasmid [36, 40].

Procedure:

Plasmids containing the His326Val mutated *B. cereus* FNR2 (BC4926) codon optimized sequence were ordered from GenScript. By using restriction endonucleases NdeI and HindIII, the gene sequence was inserted into a pET-22b(+) plasmid vector without any protein-tags. The pET-22b(+) vector contains a gene conferring resistance against ampicillin on the host bacterium, and carries a T7 promoter-based system for protein expression. The DNA and protein sequences of both wildtype *B. cereus* FNR2 and mutated FNR2 (His326Val) are listed in Appendix 1, with the mutated amino acid marked in red.

Plasmid solutions of the pET-22b(+) containing the FNR2 His326Val gene were prepared. The plasmids (4µg) were dissolved in Milli-Q water (mqH_2O) to concentration 200 ng/µl. This plasmid solution was further diluted to 50 ng/µl, which was used in transformation of competent *E. coli* cells.

2.2 Transformation of competent BL21 *E. coli* cells (DE3)

Transformation is a form of horizontal gene transfer and is one of three methods for bacterial acquisition of DNA from other organisms [41, 42]. Transformation is a process of internalization of exogenous DNA and, in many cases, integration of new DNA into the bacterial genome by homologous recombination. This allows for bacteria to obtain new genetic

traits and has been important in bacterial adaption and promotion of beneficial characteristics such as antibiotic resistance. Bacteria that is able to take up exogenous DNA are said to be competent, and certain conditions are normally required for bacteria to develop competence [43]. The fact that bacteria can take up DNA from their growth medium has proven important in biological and genetic research. Normally, bacteria only take up limited amounts of foreign genetic material, but transformation can be made efficient by making the cells competent by physical or chemical treatment, often with ice-cold calcium chloride [36].

When transforming competent bacteria with plasmids containing a gene of interest, it is normal for the plasmid construct to include genes conferring resistance against antibiotics to the transformed cell. This makes it possible to distinguish successful transformants from non-transformants because transformed cells, now having genes encoding antibiotic resistance, will be able to grow and divide on a medium containing antibiotics, while non-transformants will not [36].

Procedure:

The pET-22b(+) vectors containing the FNR2 Hid326Val gene were transformed into competent One Shot^{TM} BL21 (DE3) chemically competent *E. coli* cells (Invitrogen). Different transformation reactions were performed, with varying amount of plasmid (50-150 ng), all with 10 µl cells. One of the reactions included a control plasmid for positive control (pUC19), and one reaction was performed without plasmid as a negative control. The cells were transformed using the heat shock method by using the following protocol.

1. Competent cells were thawed on ice.
2. Five transformation reactions were set up as listed in table 2.1.
3. Transformation reactions were incubated on ice for 5 minutes.
4. Incubation at 42˚C for 45 seconds (heat shock).
5. Incubation on ice for 2 minutes.
6. Addition 125 µl of LB-medium to the transformation reactions.
7. Incubation at 37˚C with shaking (225-250 rpm) for 1 hour.

After incubation, the transformation reactions were plated onto LB agar plates containing 100 µg/ml ampicillin using a sterile spreader. The petri dishes were wrapped in parafilm and incubated overnight at 37˚C. The next day, the plates were inspected for colonies containing successfully transformed cells.

Table 2.1. Transformation reactions

Reaction	Cells (BL21 *E. coli*)	Plasmid
1	10 µl	50 ng
2	10 µl	100 ng
3	10 µl	150 ng
4	10 µl	50 ng control plasmid
5	10 µl	No plasmid (neg. control)

2.3 Overexpression of FNR2 His326Val mutant

Expression of the $FNR2_{mut}$ in transformed BL21 (DE3) *E. coli* cells were induced when the cells were in a phase of exponential growth. The protein was expressed by having the inserted gene under the control of the T7 RNA polymerase expression system, which is a system originally derived from bacteriophage lambda.

T7 RNA polymerase can synthesize RNA with higher rate than *E. coli* RNA polymerase and are highly selective for its own promoter, in addition to being resistant to antibiotics that would otherwise inhibit *E. coli* RNA polymerase [44]. The T7 RNA polymerase-based expression system (T7RNAP) is an efficient system to achieve high-level production of proteins and is well suited for directing high-level expression of genes in *E. coli*. The bacteria strain used (BL21) contains a copy of the T7 RNA polymerase gene under control of the inducible *lac* UV5 promoter. Upon induction of protein expression, addition of Isopropyl β-D-1-thiogalactopyranoside (IPTG) will induce the production of the T7 RNA polymerase. IPTG is a lactose analogue which will allosterically bind the LacI protein (*lac* repressor protein), and results in its release from the *lac* operator. By inserting a gene of interest under the control of this *lac* promoter, addition of IPTG and subsequent production of T7 RNA polymerase will result in transcription of the inserted gene [44-46].

Procedure:

Before large scale expression of the $FNR2_{mut}$, the protein expression in the transformed cells were tested to ensure that the cells would overexpress the protein. This was confirmed by running an SDS-PAGE after small scale bacterial growth and induction of protein expression. After confirming successful protein overexpression, a colony of transformed cells were picked from the agar plates and inoculated into 5 ml LB medium with 100 µg/ml ampicillin

concentration, followed by incubation overnight at 37˚C with shaking (225-250 rpm). The overnight cultures were then diluted 20x in 100 ml LB medium with 100 µg/ml ampicillin before further incubation at 37˚C with shaking (225-250 rpm) for ~6 hours. After incubation, the day cultures were further diluted 100x into 1 L terrific broth (TB) medium containing 100 µg/ml ampicillin, before incubation at 30˚C with 225-250 rpm shaking until the optical density at 600 nm (OD_{600}) had reached ~0.7, indicating that the cells are in an exponential growth phase. The cultures where then cooled on ice for 1-2 minutes before induction of protein expression with 0.5 mM IPTG, and then incubated at 18.5-22˚C with shaking (225-250 rpm) overnight (~17 hours). The bacteria were harvested by centrifugation at 5000 g in JA-10 rotor for 10 minutes at 4˚C.

2.4 Protein purification

2.4.1 Bacterial lysis

Sonication, or ultrasonication, is one of the most effective ways of lysating cells and has a smaller impact on proteins than methods based on enzymatic digestion and hydrolysis. Sonication is a way of lysing cells by using ultrasonic sound waves with high frequency (18 kHz-1MHz). The ultrasonic waves result in production of small bubbles which will grow bigger and collapse in a process called cavitation. The collapse of the gas bubbles will convert sonic energy to mechanical energy in the form of shock waves in the liquid and the energy of these shock waves will create motions in the cells, which will disintegrate when the kinetic energy becomes bigger than the strength of the cell wall. Resulting disruption of the cell wall will destroy the cell and release the cell content into the suspension [47].

Procedure:

Between 20-30 g of cells were suspended in lysis buffer (Buffer J, Appendix 3) to a total ratio of 1:4 w/v. The cells were then sonicated at 50% amplitude with 4 bursts of 20 seconds and 40 second intervals in 50-60 ml aliquots by using VC-750 Viba-Cell Ultrasonic Liquid Processor. The cell suspension was kept on ice during sonication procedure to cool down between the bursts. After the sonication, the cell lysate was centrifuged using JA-25.50 rotor at 48400 g for 30 minutes at 4˚C. The resulting supernatant, now containing the proteins, was collected for further purification of the $FNR2_{mut}$ protein.

2.4.2 Protein precipitation with ammonium sulfate

The solubility of proteins is affected by ions. Most proteins require small amounts of salt to remain folded and stable because the ions can neutralize the charges on the protein surface, and thereby prevent aggregation [48]. The interaction between proteins and the solvent, and the effects of ionic strength on protein solubility, can be utilized to precipitate proteins by a process known as salting out. The solubility of proteins will normally increase by addition of small concentrations of salt, because the salt will stabilize the charged groups on the protein surface. However, if large amounts of salt are added, the high ionic strength will result in reduced solubility, protein aggregation and precipitation. High salt concentrations will interfere with the interactions between the protein surface and the solvation shell of water molecules because less water will be available to keep the proteins in solution. As the interactions between water and protein is reduced, the protein will aggregate and precipitate from the solution [49, 50].

Protein precipitation with ammonium sulfate ($(NH_4)_2SO_4$) is a common approach for precipitation of proteins based on solubility. Ammonium sulfate is suitable because the proteins are precipitated due to aggregation as a result of reduced solubility, not denaturation [51]. Different proteins contain different amounts of hydrophilic and hydrophobic areas, and thus will precipitate at different concentrations of ammonium sulfate. As a general rule, low molecular weight proteins require higher salt concentrations to precipitate than large proteins and protein complexes. Because of the differences in salt concentration required to precipitate different proteins, salting out can be included as a step of protein purification [48, 49].

Procedure:

The volume of the supernatant containing soluble proteins after bacterial lysis was noted and, based on supplementary information from previous studies of the $FNR2_{wt}$ from *B. cereus* [3], precipitation with different amounts of ammonium sulfate was tested to discover at which concentration of salt the $FNR2_{mut}$ would precipitate (0.2 g/ml – 0.4 g/ml). The salt was slowly added to the supernatant with continuous stirring, followed by centrifugation using JA-25.50 rotor at 48400 g for 20 minutes at 4˚C. Precipitation of the $FNR2_{mut}$ was observed at 0.2 g/ml ammonium sulfate in the form of a bright yellow protein pellet corresponding to the FAD cofactor, while resulting protein pellet at 0.4 g/ml ammonium sulfate did not have a yellow colour and was therefore discarded. The protein pellet resulting from precipitation with 0.2 g/ml salt was stored at -20˚C before further purification.

2.4.3 Purification by chromatography

Purification of proteins based on their chemical and physical characteristics is an important biophysical technique that allows for separation, purification, and identification of proteins of interest contained in a mixture. By using chromatography methods, it is possible to purify proteins based on different characteristics, such as size, charge, hydrophobicity, and ligand affinity [52]. A common principle of column chromatography is the use of a liquid-solid system, where different biomolecules can adhere to a solid stationary phase. Different components of a mixture will interact differently with the column stationary phase, and therefore migrate through the column with different rates. The stationary phase used should be chemically inert and stable under the chromatographic conditions used [50].

2.4.3.1 Ion-exchange chromatography

Ion-exchange chromatography (IEX chromatography) is a common method used for separating proteins based on the net charge, and takes advantage of electrostatic interactions between charges on the protein and the column stationary phase [52]. Proteins carry charge on their surface depending on the pH of the environment and the protein isoelectric point (pI), where the pI corresponds to the pH where the protein carries a net zero charge. At pH values below a proteins pI value, the protein will be net positively charged, while at pH values above the pI value, it is net negatively charged [53]. The charge of the protein depends on the amino acid sequence and protein fold and can therefore be used to separate proteins of interest from other proteins with different charges. The principle of IEX chromatography is the exchange of proteins for small ions, where the stationary phase of the columns is bound to chemical groups which can be exchanged for proteins or ions. Anion-exchangers exchange anions while cation-exchangers exchange cations, and the choice of ion-exchanger is based on the charge of the protein to be purified. These ion exchangers can be attached to different types of solid supports, for example cellulose, agarose or vinylbenzene [50].

The protein of interest is eluted by reversing the adsorption to the column stationary phase. The elution process is normally carried out by applying a continuous gradient of salt containing a counterion that will be exchanged for the protein, resulting in the protein being released from the stationary phase into the mobile phase, and leave the column. Proteins with different net charge will bind to the column with a variety of strengths, and therefore require different concentration of salt to elute. Thus, the proteins that have adsorbed to the column will elute at different times after application of the salt gradient. Another important point is that the protein sample applied onto the column should be of very low salt concentration to prevent salt ions

from being exchanged by the ion exchangers instead of the protein of interest, which would then not be able to bind the column [50, 52, 53].

2.4.3.2 Gel filtration chromatography

The principle of gel filtration (GF) chromatography, also referred to as size-exclusion chromatography (SEC), is separation of proteins based on their molecular size. This method can be used to determine molecular weight of proteins, remove smaller molecules such as salt ions from mixtures, and purify proteins based on size [52]. GF chromatography takes advantage of different protein sizes by retaining proteins and fractionating them according to their mass. The stationary phase of the column is a matrix consisting of beads with pores of a specific size range that will retain proteins and ions with sizes smaller than the pores, referred to as the exclusion limit of the stationary phase. Then, only molecules of a specific size will diffuse into the pores of the stationary phase, and thereby be retained for a longer time. Bigger molecules will not be able to diffuse through the pores and will not be retained by the stationary phase. These large molecules will be transported through the column by the running buffer and elute as a single peak, while molecules within the fractionation range will be retained for a time that is inversely proportional to their mass [50, 52, 54].

Chromatography procedures:

The protein precipitated with ammonium sulfate was dissolved in Buffer A and filtrated using a sterile 0.45µm filter (Sarstedt) and a 20 ml syringe (BD Plastipak). Before purification by IEX chromatography the protein sample was desalted to remove any excess of salt. The desalting process was preformed using SEC with HiTrap Desalting column (GE Healthcare) on Äkta-purifier system with Buffer A. Alternatively the protein sample was desalted with dialysis in the last round of purification using Buffer G (Appendix 3). The desalted protein fractions with absorption at 280 nm and 450 nm was collected for further purification.

Desalted protein was purified by IEX chromatography using a HiTrap Q HP anion exchange column (GE Healthcare) on the Äkta-purifier system. In each run of IEX chromatography, 5-12 ml of desalted protein sample was applied on the column with Buffers A, D and G and eluted with a linear gradient of 0-45% Buffers B, E and H over 20 column volumes (Appendix 3). All the fractions with absorption at 450 nm was collected, analyzed by SDS-PAGE, and concentrated using Amicon Ultra Centrifugal Filters (30 kDa NMWL, Merck Millipore) by centrifugation at 5000 g in JA-25.50 rotor at 4˚C.

The concentrated protein sample collected after IEX chromatography was further purified by GF chromatography using a Superose 12 10/300 column GL (GE Healthcare) and with Buffers C, F and I as running buffers (Appendix 3). For each run, 120-150µl of concentrated protein sample was loaded on the column. All fractions showing absorption at 450 nm was collected, analyzed by SDS-PAGE, and concentrated using Amicon Ultra Centrifugal Filters (30 kDa NMWL, Merck Millipore) by centrifugation at 5000 g in JA-25.50 rotor at 4˚C. The purified and concentrated protein sample were frozen in liquid nitrogen and stored at -80˚C.

Due to significant protein precipitation during the purification and concentration procedures, alternative purification conditions were tested to investigate whether the $FNR2_{mut}$ would be more stable with different buffers, reductants or at a different pH. Successive rounds of purification were performed using different conditions as listed in table 2.2, with buffers A-I described in Appendix 3. An attempt was done to investigate protein stability by nanoDSF, but the results were inconclusive (data not included).

Table 2.2. Overview of the different buffers and conditions used for three purification rounds of the FNR2 mutant.

Purification condition (nr).	IEX	GF	Reductant	pH
1	50 mM Tris-HCl (Buffer A) and 50 mM Tris-HCl, 1M KCl (Buffer B)	50 mM HEPES, 100 mM KCl (Buffer C)	DTT	8.0
2	50 mM Tris-HCl (Buffer D) and 50 mM Tris-HCl, 1M KCl (Buffer E)	50 mM HEPES, 100 mM KCl (Buffer F)	TCEP	7.5
3	50 mM HEPES (Buffer G) and 50 mM HEPES, 1M KCl (Buffer H)	50 mM HEPES, 100 mM KCl (Buffer I)	DTT	7.5

2.5 Sodium dodecyl sulfate polyacrylamide gel electrophoresis

One of the most commonly used methods for obtaining analytical separation of proteins with high resolution is sodium dodecyl sulfate polyacrylamide gel electrophoresis (SDS-PAGE). This technology is used for investigation of purity of protein samples, as well as for estimating protein molecular mass. SDS-PAGE is a type of denaturing electrophoresis in which the proteins are denatured by the addition of sodium dodecyl sulfate (SDS), a detergent consisting

of a hydrophobic 12-carbon chain and a sulfated polar head. The hydrophobic chain will intercalate into hydrophobic parts of the proteins and disrupt the folded three-dimensional structure, thereby denaturing the proteins. In addition, SDS will impart to all the proteins a negative charge that is proportional to the molecular mass. The interaction between SDS and the protein to be analyzed is followed by electrophoresis, in which the negative charges on the proteins will cause them to migrate through a porous acrylamide gel matrix towards the anode when an electric field is applied. As the negative charge driving the migration of the polypeptides is proportional to the polypeptide mass, the proteins will be separated based on their molecular mass [50, 55].

Procedure:

In this project, SDS-PAGE was primarily used for identification of $FNR2_{mut}$ overexpression in transformed *E. coli* cells, and for inspection of purity during and after protein purification steps. The collected protein samples to be analyzed was mixed 1:4 with NuPAGE LDS sample buffer (4X) (Invitrogen), and the mixtures were incubated on heat block at 96˚C for 5-10 minutes before 5-10 seconds of vortex. 5-10 µl of sample was loaded on a NuPAGE Bolt 4-12 % Bis-Tris, 1.0 mm, Mini Protein Gel (Invitrogen) placed in NuPAGE MOPS SDS running buffer (Invitrogen). The SDS-PAGE was run at 200 V for 20 minutes (Bolt Mini Gel Tank), and the gels were then stained using InstantBlue Coomassie Protein Stain (Expedeon) for 1-2 hours. After rinsing off the protein stain with water, the results were analyzed by observation of protein bands around 36 kDa, compared with SeeBlue Plus2 Pre-Stained Protein Standard (Invitrogen).

2.6 Native polyacrylamide gel electrophoresis

Many proteins form natural protein complexes and protein-protein interactions in their native state, and obtaining information considering the oligomerisation and interaction between proteins is an important step to understanding protein function and regulation. Native polyacrylamide gel electrophoresis (NativePAGE) is a method commonly used for determination of native protein oligomeric states and protein masses, as well as characterization of protein-protein interactions. This method is a form of nondenaturing electrophoresis where proteins are separated in native conformations according to their hydrodynamic shape and size by migration in a polyacrylamide matrix [50, 55, 56]. In blue nativePAGE, the protein sample is mixed with Coomassie G-250, which binds to the proteins and confers a negative charge without denaturation of the proteins. This will allow migration of the proteins through the gel

when an electric field is applied, and the length of the migration will be determined by the proteins size and shape [57].

Procedure:

Prior to loading the protein onto the polyacrylamide gel for nativePAGE analysis, the purified $FNR2_{mut}$ protein sample (57 mg/ml) were diluted 1:2 and 1:4 in mqH_2O before addition of NativePAGE Sample Buffer (4X) (Invitrogen). The anode buffer was prepared by making a 1x dilution using NativePAGE Running Buffer (20X) (Invitrogen) with mqH_2O, while the cathode buffer, containing Coomassie G-250, was also diluted to 1x by mixing NativePAGE Running Buffer (20X) and NativePAGE Cathode Additive (20X) (Invitrogen) with mqH_2O. The diluted protein samples were loaded on a NativePAGE 4-16% Bis-Tris, 1.0 mm Mini Protein Gel (Invitrogen) in a Xcell SureLock Mini-Cell chamber (Life Technologies), with the cathode buffer (dark blue) in the inner chamber and anode buffer in the outer chambers. The nativePAGE electrophoresis was run at 150 V for 120 minutes using Pharmacia Biotech EPS 600, before the gel was treated with a Fix solution (40% methanol, 10% acetic acid) for 15 minutes at room temperature. After treatment with Fix solution, the gel was placed in a destain solution (8% acetic acid) and incubated 3 hours, also at room temperature. All buffers and solutions used in nativePAGE is described in Appendix 3.

2.7 Protein crystallization

2.7.1 Principle of protein crystallization

The process of protein crystallization is highly dependent on the purity of the protein sample and conditions of the crystallization experiment such as concentration of precipitant solution, pH, and temperature. The principle of achieving a crystalline state is to recruit protein molecules from a liquid phase into a highly ordered solid phase. This is achieved by increasing the concentration of protein and precipitants (polyalcohols, salt, organic solvents, polymers) and thereby creating a supersaturated protein solution in which the protein will be forced out of solution to form small critical nuclei from which a crystal can grow [50, 58].

Proteins will stay dissolved in solution up to a specific concentration and exceeding this concentration, also known as the solubility limit, will result in phase changes which can give crystal formation [59]. The phase diagram for protein crystallization (figure 2.1) represents the state of a protein solution as a function of relevant variables such as protein concentration, temperature, pH, and characteristics of the precipitant solution. The phase diagram can be divided into four different areas corresponding to different states of the crystallization

experiment. In the precipitation zone, the supersaturation is too high, and the protein will precipitate without forming any crystals. The nucleation zone corresponds to moderate supersaturation where the protein will be forced out of solution to form stable nuclei. This process is called nucleation, and supersaturation is essential for nucleation due to the activation energy barrier, which is the energy required to create small nuclei from which crystals can grow. At lower supersaturation, below the nucleation zone, is the metastable zone where the supersaturation is too low for formation of new nuclei, but already formed nuclei can grow into larger crystals. The last area of the phase diagram is located below the solubility curve and is called the undersaturated zone, where protein is dissolved and will not form crystals [59, 60].

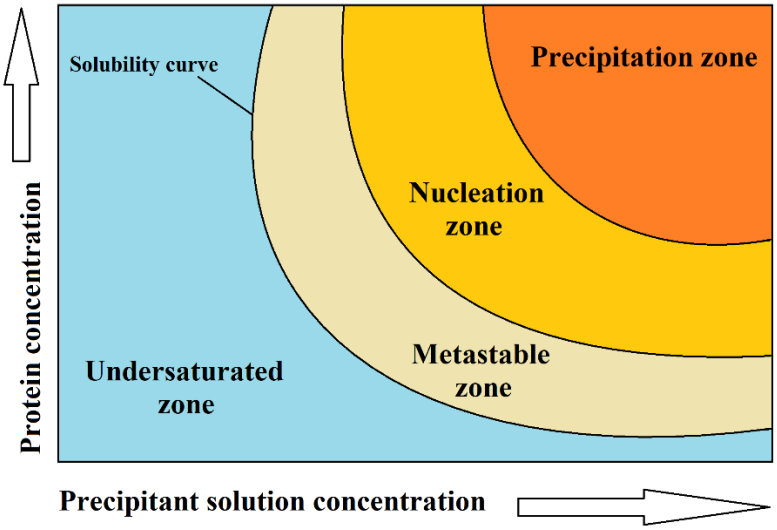

Figure 2.1. Phase diagram for protein crystallization showing the state of the protein solution as a function of protein concentration and precipitant solution concentration.

2.7.1.1 Vapor diffusion:

Vapor diffusion is one of the most widely used methods for protein crystallization, and is based on slow equilibration between a bulk precipitant solution and a drop of concentrated protein sample until the conditions in the drop and precipitant solution are identical [50, 60]. The protein drop in vapor diffusion can either be hanging from a glass slide over the precipitant solution reservoir, called hanging drop, or sit in a depression placed in the vapour phase of the precipitant solution in a sitting drop experiment.

The protein solution is typically mixed in a 1:1 ratio with the precipitant solution, and because of the vapour pressure being lower in the precipitant solution due to higher concentration, there will be a net transfer of water out of the protein drop. This elimination of water from the drop will result in supersaturation, bringing the drop past the metastable point to trigger nucleation and crystal formation. As the nucleation proceeds in the drop, the protein concentration will

consequently be reduced and thereby lower the degree of supersaturation, bringing the experiment into the metastable zone for crystal growth [61, 62].

Procedure:

By using the purified protein samples of the $FNR2_{mut}$, several crystallization screens using the sitting drop method were performed to search for conditions in which the protein would form crystals satisfactory for X-ray diffraction. Crystallization screens were performed after three separate rounds of protein purification, using a Mosquito crystallization robot (SPT Labtech) with crystallization screens Morpheus (Molecular Dimensions), JCSG+ (Molecular Dimensions), PGA (Molecular Dimensions) and Index (Hampton Research), and with protein concentrations between 9-57 mg/ml. For each crystallization screen, one or two protein conditions (1x and 2x) were set up as shown in table 2.3.

Table 2.3. Overview of the crystallization screen experiments showing the crystallization conditions used with the corresponding protein concentrations and drop sizes.

Crystallization screening trial	Number of drops per screen condition	[$FNR2_{mut}$]	Screen	Drop size
1	1	9.72 mg/ml	Morpheus, JCSG+, Index	250nl+250nl
2	2	24.1 mg/ml + 12.2 mg/ml	Morpheus, JCSG+	250nl+250nl
3	1	57 mg/ml	Morpheus	250nl+250nl

After the screening, selected conditions from the Morpheus screen where protein crystals had formed was used for optimization in attempts to grow larger crystals. The optimization was performed using the sitting drop method with protein drops (1.0 µl protein + 1.0 µl precipitant solution) over a reservoir of 100 µl precipitant solution with varying concentrations (100-70%) and two drops for each of the precipitant solution concentrations, as shown in table 2.4. All crystallization experiments were performed and stored at room temperature. A selection of the resulting crystals was isolated and frozen in liquid nitrogen to be used for X-ray diffraction. Crystals resulting from the Morpheus screen, already being in cryo-solution, were frozen directly.

Table 2.4. Overview of the optimization of crystallization using different conditions from the Morpheus screen (Molecular Dimensions).

Morpheus condition	Number of drops	[$FNR2_{mut}$]	[Precipitant solution]	Drop size
D11	16	24.1 mg/ml + 12.2 mg/ml	100-70%	1.0µl + 1.0µl
E11	16	24.1 mg/ml + 12.2 mg/ml	100-70%	1.0µl + 1.0µl
H11	16	24.1 mg/ml + 12.2 mg/ml	100-70%	1.0µl + 1.0µl
D10	8	57 mg/ml	100-70%	1.0µl + 1.0µl
F10	8	57 mg/ml	100-70%	1.0µl + 1.0µl

The procedure describing the co-crystallization of $FNR1_{wt}$ with $NADP^+$ is described in Appendix 6.

2.8 Protein X-ray crystallography

Determination of three-dimensional structure is an important field in the study of proteins, as the function of proteins are determined by their structures. The secondary structural elements of proteins can often be predicted based on the amino acid sequence, while the folded three-dimensional structure is generally not possible to predict from the primary structure alone. Protein crystallography enables us to investigate and solve the folded structure of proteins, and thereby obtain information considering function and interaction with other proteins, substrates, and cofactors [60, 63, 64].

X-ray crystallography is used in the study of protein structure by investigating X-ray diffraction patterns obtained from protein crystals. The basis of this technique is that the X-rays are scattered by the electrons of the atoms in a protein, and the X-rays will diffract to give a pattern that is dependent on the location of individual atoms in the three-dimensional structure. X-rays have wavelengths around 1 Å, which is of the same order of magnitude as interatomic distances (chemical bonds) in a molecule, enabling us to observe structural details on the atomic level. From the resulting X-ray diffraction patterns, it is possible to solve the structure and thereby visualize the proteins [50, 58]. Contribution of many atoms to the diffraction pattern is important to detect diffracted X-rays with high sensitivity. For this reason, to get an enhanced signal, the protein molecule should be present in a highly ordered three-dimensional array known as a crystal. Protein crystals are repeating three-dimensional arrays of molecules held together by weak interactions, such as van der Waals interactions and hydrogen bonds [50].

The unit cell can be characterized as the basic building blocks of the crystal. The unit cell is the smallest repeating unit of the crystal lattice, and can be described as having six faces with lengths a, b, and c, as well as three angles denoted α, β and γ. For a given protein crystal, several different unit cells may be chosen, but normally the chosen unit cell is the smallest one with the highest symmetry. The translation of the unit cell in the three lattice directions will reproduce the entire structure of the crystal. A unit cell also contains a unique part called an asymmetric unit, which is the smallest part of a unit cell that does not have internal symmetry but can be translated by symmetry operations within the unit cell [50, 65]. Crystals are normally divided into groups called crystal systems according to their symmetry, and it is possible to describe a crystal by combining several symmetry elements. One specific combination of such symmetry elements is known as a space group [50]. As the unit cell is repeated throughout the entire crystal structure, the scattering of the incoming X-rays will be enhanced in some directions but extinguished in others, governed by the unit cell and X-ray wavelength. As a result, the structure of the crystal will be encoded in the obtained diffraction pattern. From the X-ray diffraction data, we can obtain a map of the electron density of the crystal, called an electron density map, from which it is possible to model in the individual atoms and amino acid residues of the protein structure [65].

2.8.1 Diffraction data collection

Electrons moving at relativistic speeds in a ring-shaped accelerator will emit electromagnetic radiation when forced by a magnetic field to follow curved trajectories. This emitted radiation is called synchrotron radiation and is a form of high energy X-ray radiation commonly used to obtain diffraction patterns from protein crystals. The synchrotron radiation will interact with the electrons in the crystal, making them oscillate and emit secondary radiation with identical wavelength and frequency as the incident X-ray, and thereby making it possible to obtain a diffraction pattern corresponding to the location of different atoms in a protein crystal [50, 66].

When many electrons diffract X-rays, the waves of the diffracted radiation will often combine and result in a phenomenon known as interference. The interference between the diffracted waves may result in either reinforcement, called constructive interference, or weakening of the wave amplitude, called destructive interference. The interference pattern observed is dependent on the atom distribution in the protein crystal, and therefore, the interference pattern will encode information related to three-dimensional locations of atoms in the crystal [50].

According to Braggs' model, a protein crystal can be regarded as consisting of planes cutting through the crystal lattice in three dimensions, acting as mirrors reflecting the incoming X-rays.

One such lattice plane in the crystal will reflect only a fraction of the incoming X-ray radiation, while the rest of the beam will be reflected by other underlying planes. The different lattice planes present in the crystal is commonly numbered using Miller indices (h, k, l). As the incident radiation passes through successive lattice planes, the reflected waves must travel a longer distance than the reflected waves from the overlying planes. For constructive interference to occur between the diffracted waves from successive planes, the path length difference of the waves must be an integral number of wavelengths (nλ). Two such waves, with path length difference equal to an integral number of wavelengths, are said to be in phase and will be amplified by each other due to constructive interference and result in a reflection in the obtained diffraction pattern. This phenomenon can be described by Braggs law (Equation 1).

$$n\lambda = 2d\ sin\theta \qquad (1)$$

where n is an integral number, λ is the wavelength of the diffracted wave, d is the distance between two planes in the crystal lattice, and θ is the angle between the lattice plane and the diffracted wave. The value of θ may be varied by rotation of the crystal commonly 0.1-1.0˚ between X-ray beam exposure, and such rotation will allow detection of a distinct reflection pattern for each rotation. In total, a crystal is normally rotated 180˚, because the intensity of reflections from the opposite face of the lattice planes will be equal [50, 67, 68].

Procedure:

The diffraction data was collected at Beamline ID30B at the European Synchrotron Research Facility (ESRF) in Grenoble, France. During data collection, a grid search was performed (MxCube) to find the most optimal part of the crystal for diffraction. A complete dataset was collected to 4.90 Å based on this suggested grid.

2.8.2 Solving the structure

Interpretation of the diffraction data obtained from X-ray diffraction is an important step in finding the position of the individual atoms in the asymmetric unit and solving the protein structure. As a first step in analyzing the diffraction data, the unit cell is determined, and each reflection is assigned Miller indices (h, k, l) in a process called indexing. From the unit cell, the computer software can assign the symmetry and the space group of the crystal [50, 65].

The reflections in the diffraction data are often spread over several images, due to mosaic spread and rotation of the crystal between beam exposures, and these need to be summed. This process is known as integration and will result in a list of hkl-values with the corresponding intensity

of the diffraction spots. In addition, each of the reflections have been collected several times and therefore must be scaled and merged, referred to as scaling, to obtain a set of unique reflections. Reflections who are symmetry related must also be merged.

The quality of the data after indexing, integration and scaling is indicated by the value of R_{meas}, which compare the reflections that should be equal, as well as indicating if the correct space group has been assigned. There are several quality criteria that should be analyzed to obtain information about the quality of the diffraction data. Among these are the completeness, redundancy, I/σ(I) and $CC_{1/2}$ [50, 65].

To obtain an electron density map by Fourier synthesis, showing the location of the atoms in the crystal, the intensities of the reflections is converted into a structure factor (F_{hkl}). Being interested in the three-dimensional location of the atoms in the protein crystal, the amplitude and wavelength is not sufficient to fully describe the diffracted X-rays. Because the reflections result from a combination of diffracted wavelengths by different atoms, the different reflections have different phase angles. The phase angles must therefore be determined to calculate the electron density map. This information cannot be obtained from the reflections directly, and therefore, this is referred to as the phase problem. There are three common methods that may be used for indirect estimation of the phases: direct methods, molecular replacement, and different types of special-atom methods. Molecular replacement, being the most common method for solving structures from diffraction patterns, make use of an already solved structure with homology to the protein of interest, and the phases from the already known structure is used to determine the phases of the protein structure to be solved. With the phase problem solved, the model may be adjusted through cycles of modelling and refinement to obtain a structure who is in agreement with the diffraction data [50, 65, 68].

Procedure:

Indexing and integration of the obtained diffraction data was done by auto-processing at the synchrotron (XDS)[69]. Further processing of the diffraction data was performed using the CCP4 software, where scaling and merging was done in Aimless to check the space group and obtain quality parameters. To solve the structure, molecular replacement was used with the wild type FNR2 from *B. cereus* as starting model (Phaser). The $FNR2_{mut}$ structure was modelled into the electron density using Coot with cycles of refinements using REFMAC5, while monitoring the *R*-factor and R_{free} values. Validation of the structure between refinements were performed by investigating the Ramachandran plot and geometry validations in Coot. Modelling of the

$FNR2_{mut}$ structure included adjustments of rotamers of side chains and mutation of the His326 residue to Val326. The resulting protein structure was visualized using PyMOL (Schrödinger, LCC) [69-71].

The procedure used when solving the structure of FNR1 co-crystallized with $NADP^+$ is described in Appendix 6.

2.9 UV-visible spectroscopy

Light is a form of electromagnetic radiation, which spans over a wide range of the electromagnetic spectrum. Each part of the electromagnetic spectrum can be characterized by a specific interval of wavelengths, and radiation with different wavelengths will interact with biomolecules in different ways, and thereby give information about the features of the molecule [50, 72].

Light in the ultraviolet/visible (UV-vis) part of the electromagnetic spectrum (200-900 nm) can be passed through a sample of proteins in solution, and thereby promote excitation of electrons from the ground state due to absorption of energy corresponding to specific wavelengths by the electrons. The absorbed wavelength is dependent on the energy difference between the molecular orbitals of the electron excitation, a feature specific for different types of atoms and biomolecules. Molecules capable of absorbing light are called chromophores, and the particular wavelengths absorbed by the electrons are affected by both the structure and the environment of the chromophore. Therefore, different structures will absorb different frequencies and can provide useful information in the study of proteins [50, 73].

Spectroscopy is the study of how light interact with matter, and UV-visible spectroscopy is a measure of the electronic transition of electrons due to absorption of energy from electromagnetic radiation. The absorption of energy can be quantified by the Beer-Lambert law which considers the intensity of the incident (I_0) and transmitted (I) light, as well as the molar concentration (c) and length of the light path (l) (Equation 2).

$$\varepsilon cl = \log \frac{I_0}{\mathrm{I}} = A \qquad (2)$$

Where Ɛ is the molar extinction coefficient of the protein, which corresponds to how strongly the chromophores of the protein absorb light at a specific wavelength. In addition, log(Io/I) is equal to the absorbance at a particular wavelength (A_λ). Since the absorbance is directly dependent on the molar protein concentration, Beer-Lambert law is frequently used to calculate

the concentration of a protein sample by measuring the absorbance at a particular wavelength [50].

In the study of proteins, the absorbance of some wavelengths is particularly useful. The aromatic amino acids (tryptophan and tyrosine) show strong absorbance at 280 nm, and different types of cofactors often have a characteristic absorption at specific wavelengths. In addition, protonation and deprotonation effects resulting from redox reactions or changes in pH will often change the distribution of electrons in the chromophore, resulting in differences between the absorption spectra of the protonated and deprotonated forms [50, 73].

Concentration measurement procedure:

In this project, UV-visible spectroscopy (Agilent Cary 60 spectrophotometer) was used for determination of protein concentration in the purified protein samples before crystallization. First, a baseline using 800 µl Buffer A was recorded in a 1 ml quartz cuvette, before 2-4 µl of the protein sample was added. Absorption maxima was then investigated at λ_{max} = 460 nm corresponding to the absorption of the FAD cofactor, and Beer-Lambert law was used to calculate the protein concentration using molar extinction coefficient 11.1 $mM^{-1}cm^{-1}$ [3] and standard cuvette length of 1 cm.

2.9.1 Enzyme kinetics

Enzymes work as catalysts in biochemical reactions by reducing the activation energy barrier for product formation, and thereby enhancing the rate of the reaction. As a first step in catalysis, the enzyme forms a complex with the specific substrate (ES complex), and the resulting interaction made between the enzyme active site and substrate leads to a release of free energy, and thereby an increase in the energy available for converting the substrate into products. By investigating different kinetic parameters of an enzyme-catalysed reaction, it is possible to obtain insight in the function and efficiency of the enzyme catalysis [11, 74].

The catalytical rate of a reaction (V_0) is defined as the amount of product formed per unit of time. As the substrate concentration ([S]) increases, the rate will also increase as long as [S] is small, but the rate will be independent of the substrate concentration when [S] is large due to saturation of the enzyme active sites. Therefore, by performing reactions with increasing [S], it is possible to obtain a linear relationship between the initial rate of the reaction and the substrate concentration, giving data that may be used in determination of the rate of the enzyme-catalysed reaction. At low substrate concentration, the initial rate of the reaction will increase when [S] is increased. As the substrate concentration is increased further, the increase in reaction rate

will decline until the [S] has little effect on the initial rate of the enzyme-catalysed reaction. At this point, the enzyme is said to be close to substrate saturation, and this corresponds to the maximal velocity of the enzyme, V_{max} [74, 75]. This variation in enzyme activity as a function of substrate concentration is described by Equation 3.

$$V_0 = V_{max} \frac{[S]}{[S]+Km} \qquad (3)$$

Where K_M is called the Michaelis-Menten constant and corresponds to the substrate concentration where the reaction rate is half of V_{max} ($V_{max}/2$). The value of K_M is unique for a specific enzyme and partially describes the features of the enzyme-substrate interactions. A low value of K_M indicates that only a small amount of substrate is required for saturation of the enzyme, while a high K_M shows that the enzyme requires higher concentrations of substrate to become saturated [11, 75].

The maximal rate of an enzyme-catalysed reaction, V_{max}, reveals the enzymes` turnover number, which is defined as the number of substrate molecules converted per time unit when the enzyme is saturated with substrate. This value is equal to the rate constant of product formation, also called k_{cat}. When [S] is much larger than the K_M value of the enzyme, the rate of catalysis will be equal to the turnover number (k_{cat}). A high value of k_{cat} indicates that the enzyme can convert many substrate molecules per time unit [11, 74, 75].

Activity measurement procedure:

In addition to protein quantification, UV-visible spectroscopy was used in activity measurements of both the $FNR2_{wt}$ and the $FNR2_{mut}$ in reactions with NrdI and Fld1 as substrates. The wild type protein and substrates were not expressed or purified as a part of this project, but were previously purified and stored at -80˚C.

Prior to the anaerobic assays, the buffer was degassed using argon 5.0 (99.99%) for 2-3 hours, while the protein/NADPH samples were degassed by using cycles of 5x4 minutes alternating between vacuum and argon, leaving the samples under argon pressure and eliminating any oxygen. All reactions were performed using 50 mM HEPES, 50 mM KCl buffer with pH 7.5, and with a total volume of 800 µl in a 1 ml quartz cuvette with stirring, and the reactions were activated by the addition of the $FNR2_{mut/wt}$ enzyme. In addition, all reactions were performed under anaerobic conditions in a glove box (91% N_2, 9% H_2, AGA) (Plas-Labs Anaerobic Chamber 855-AC with Agilent 8453 diode-array UV-vis spectrophotometer) to avoid spontaneous reoxidation of NrdI/Fld1 during the experiments. Spectrophotometric data was

recorded using an Agilent 8453 UV-visible spectrophotometer at 25˚C. The reactions were mostly carried out as described by Lofstad *et. al*. and Gudim *et. al*. [3, 16], but with some modifications considering variations in substrate concentration.

In the first experiment, six reactions were set up with NrdI concentration ranging from 1-70 µM and NADPH- and enzyme concentrations kept constant at 0.2 mM and 0.5 µM, respectively, to investigate the efficiency of the NrdI reduction by the $FNR2_{mut}$ with NADPH. During the experiments, the reduction of NrdI by the $FNR2_{mut}$ enzyme was monitored by the appearance of the reduced $NrdI_{sq}$ state (λ_{max}= 574 nm), and the disappearance of the oxidized $NrdI_{ox}$ state (λ_{max}= 447 nm), as well as monitoring the consumption of NADPH by decrease at λ_{max} = 340 nm [16]. After obtaining the activity measurements for the $FNR2_{mut}$ with NrdI, the same reactions were performed using the $FNR2_{wt}$ enzyme to compare the activity of the mutant with the wild type protein.

In the second activity measurement experiment, six reactions were set up with Fld1 concentrations ranging from 1-30 µM and NADPH- and $FNR2_{mut}$ concentrations kept constant at 0.2 mM and 0.5 µM, respectively. The Fld1 reduction was monitored by investigating the disappearance of the $Fld1_{ox}$ state at λ_{max} = 461 nm and the appearance of the $Fld1_{sq}$ state at λ_{max} = 594 nm. Again, the consumption of NADPH was monitored by the decrease at λ_{max} = 340 nm [16].

All the obtained data from the activity measurements was processed and plotted using Origin (OriginLab Corp., Northampton, MA, USA). The initial reduction rates were determined by plotting the reduction of NrdI/Fld1 (447/461 nm) as a function of time. The steady-state kinetic parameters of the reactions were determined by using curve fitting to the Michaelis-Menten model (Equation 3), and the catalytic rate of the reactions were determined by calculating k_{cat}, using Equation 4.

$$k_{cat} = \frac{V_{max}}{[E]} \qquad (4)$$

Where [E] is the molar enzyme concentration used in the activity measurements.

3 Results and discussion

The aim of this project has been to study the effect of a His326Val mutation in the FNR2 protein from *B. cereus*, to investigate possible explanations for the difference in the activity of the FNR1 and FNR2 wild type enzymes in respect to their different FAD-stacking residue. The mutated FNR2 gene was cloned into competent *E. coli* cells and overexpressed before purification, activity assays and attempts to crystallize the protein for X-ray diffraction. As an additional project in this thesis, an attempt was made to co-crystallize the $FNR1_{wt}$ with $NADP^+$ to see if this would lead to any structural changes, after previous attempts has failed to find any electron density corresponding to NADPH in the previous structure of *B. cereus* FNR1 or FNR2.

Protein purification of the $FNR2_{mut}$ were performed in three rounds, using different buffers, pH values and reductants. In addition, two different colonies of transformed bacteria were used in protein expression. Figure 3.1 present the workflow from protein expression to crystallization.

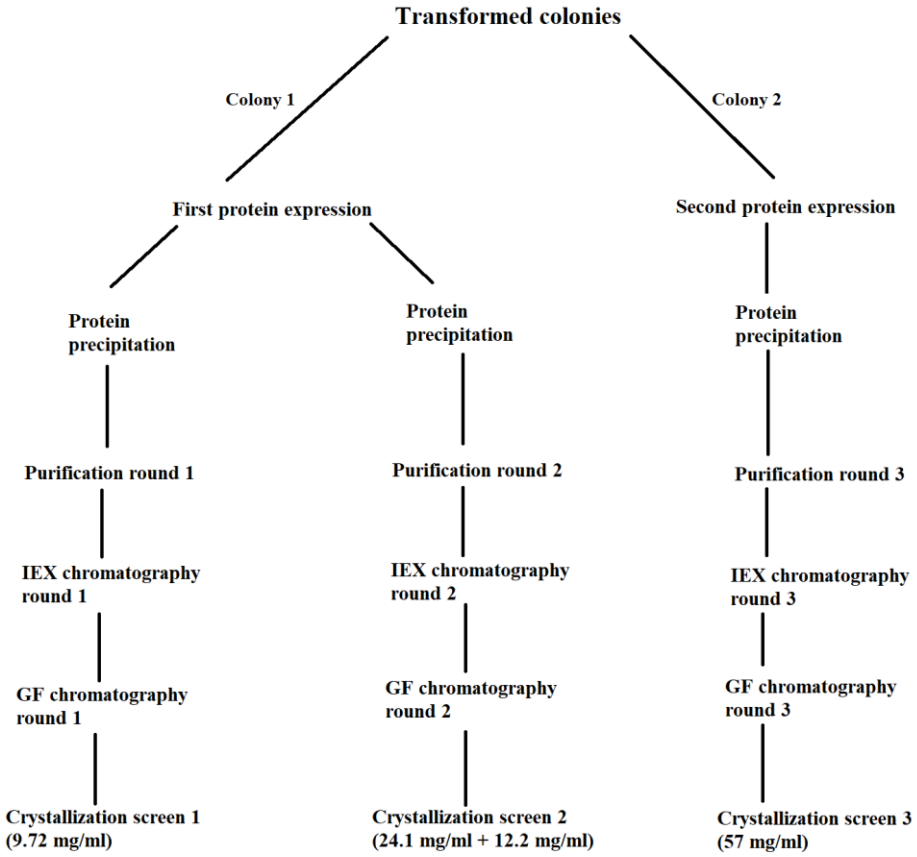

Figure 3.1. Flowchart showing the workflow from transformed colonies to crystallization screening. Protein expression was performed using two different colonies, followed by three rounds of protein precipitation with ammonium sulfate and purification by chromatographic procedures.

3.1 Transformation and overexpression of the FNR2 mutant

The transformation of the recombinant plasmids containing the FNR2 mutation into the competent BL21 (DE3) *E. coli* cells was controlled by plating the cells out on LB-plates containing ampicillin. Since the plasmids transformed into the bacteria contained genes conferring ampicillin resistance onto the cells, growth of many colonies indicated successful transformation. Protein expression in eight of the resulting colonies was tested by SDS-PAGE analysis after induction of the cell cultures with IPTG, and the results shown in figure 3.2 confirms successful overexpression of the $FNR2_{mut}$ in all the colonies analyzed.

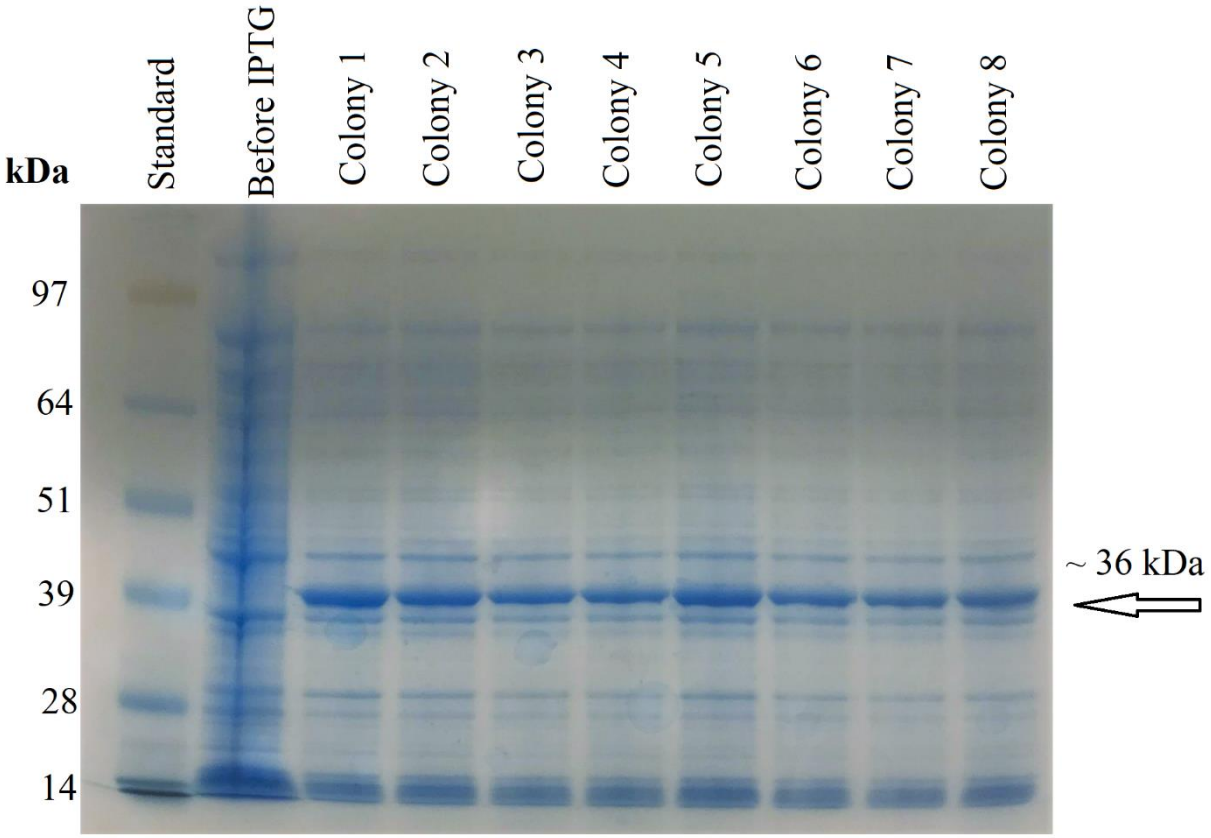

Figure 3.2. SDS-PAGE analysis of protein expression in the transformed cells from different colonies. Arrow indicating the overexpressed protein of interest, with molecular weight 36 kDa.

After confirming successful overexpression of the $FNR2_{mut}$ in the transformed cells by a clear appearance of a protein band around ~36 kDa, one of the colonies was picked for large-scale bacterial growth and expression of the protein for further purification.

3.2 Protein purification

Previous studies have shown that the $FNR2_{wt}$ from *B. cereus* will precipitate at 0.2 g/ml ammonium sulfate during salting out experiments [3]. For the $FNR2_{mut}$, two different concentrations of salt were used to investigate the precipitation of the protein. After cell lysis and centrifugation to remove cellular matter, salting out was performed on the supernatant with ammonium sulfate concentration 0.2 g/ml, before further salting out to total concentration 0.4 g/ml. From the yellow colour of the resulting protein pellet, it was clear that the $FNR2_{mut}$ had precipitated at 0.2 g/ml. The lack of yellow colour in the resulting protein pellet after precipitation at 0.4 g/ml led to the conclusion that most of the protein had precipitated at 0.2 g/ml. The protein pellet from precipitation with 0.2 g/ml ammonium sulfate was collected for further purification, while the pellet from precipitation with 0.4 g/ml was discarded. SDS-PAGE analysis was performed using both the supernatant and protein pellets after both steps of protein precipitation to confirm the presence of the protein, but due to loading of too much sample onto the gel, no conclusions could be drawn from the SDS-PAGE results alone. The conclusion that the $FNR2_{mut}$ precipitated at 0.2 g/ml ammonium sulfate is thereby based on observation of bright yellow colour, indicating the presence of the FAD cofactor in the protein pellet. Although the yellow colour of the protein pellet confirmed the presence of the mutant protein, additional optimization of the concentration at which the $FNR2_{mut}$ would precipitate could be helpful to remove many other proteins before further purification by chromatographic methods.

In the first round of IEX chromatography using Buffer A, the protein eluted at 17-23% (~25 mS/cm) buffer B (60-72 ml) as indicated by the overlap of peaks corresponding to both 280 nm and 450 nm shown in figure 3.3.

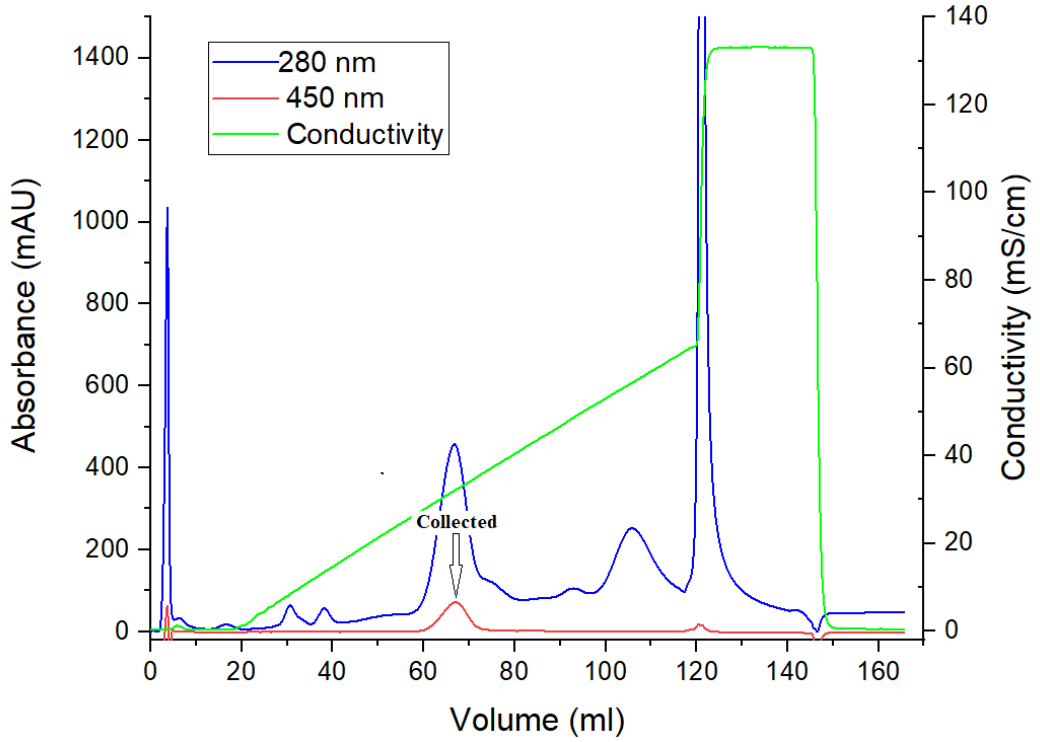

Figure 3.3. Chromatogram from the first round of IEX chromatography using Buffers A and B. Black arrow indicating the collected peak.

After the first run, the linear gradient was adjusted from 45% to 30% maximum concentration of Buffer B while the length of the gradient was kept constant and was run over 20 CV in attempts to improve the peak separation in the area of FNR2 elution.

The collected fractions were kept separate after the first two runs, and an SDS-PAGE analysis was performed on all the collected fractions corresponding to 450 nm absorption to confirm elution of the $FNR2_{mut}$. Due to a minor absorption at 450 nm in the flowthrough fraction, the flowthrough fraction from the first run was also analyzed. From the yellow colour of the collected 450 nm fractions and from the SDS-PAGE results shown in figure 3.4, it was confirmed that an excess of the $FNR2_{mut}$ was present in all the collected fractions except the flowthrough fraction.

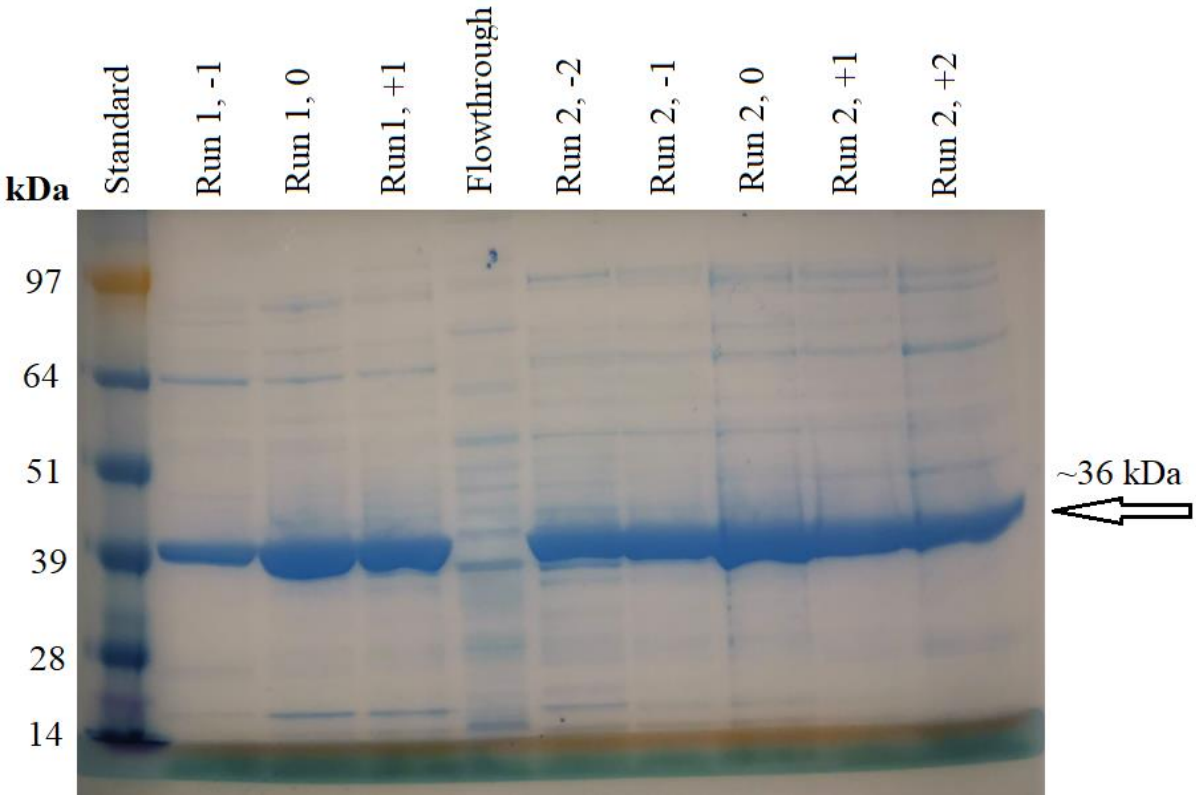

Figure 3.4. SDS-PAGE results after the first round of purification by IEX (runs 1+2). Numbers (-2, -1, 0, +1 and +2) represent fractions collected before and after the peak maximum, with 0 being the fraction corresponding to peak maximum. All fractions collected after 60 ml. Excess of the $FNR2_{mut}$ in the fractions indicated by arrow at ~36 kDa.

The collected fractions from IEX chromatography were concentrated by centrifugation in Amicon Ultra Centrifugal Filters (30 kDa NMWL, Merck Millipore). During the concentration process, the protein started precipitating extensively from the solution, and proved difficult to concentrate due to instant clogging of the tube filters. This precipitation could indicate poor stability of the $FNR2_{mut}$, and that optimization of the expression and/or purification conditions would be necessary to investigate at which conditions the protein would be more stable.

After attempting to concentrate the fractions from IEX chromatography, the sample was purified further by GF chromatography, with Buffer C as running buffer, to obtain a purer sample of the $FNR2_{mut}$. The resulting chromatogram from this purification step is shown in figure 3.5, and it is clear, by the overlapping absorbance at 280 nm and 450 nm, that the protein eluted as a single peak.

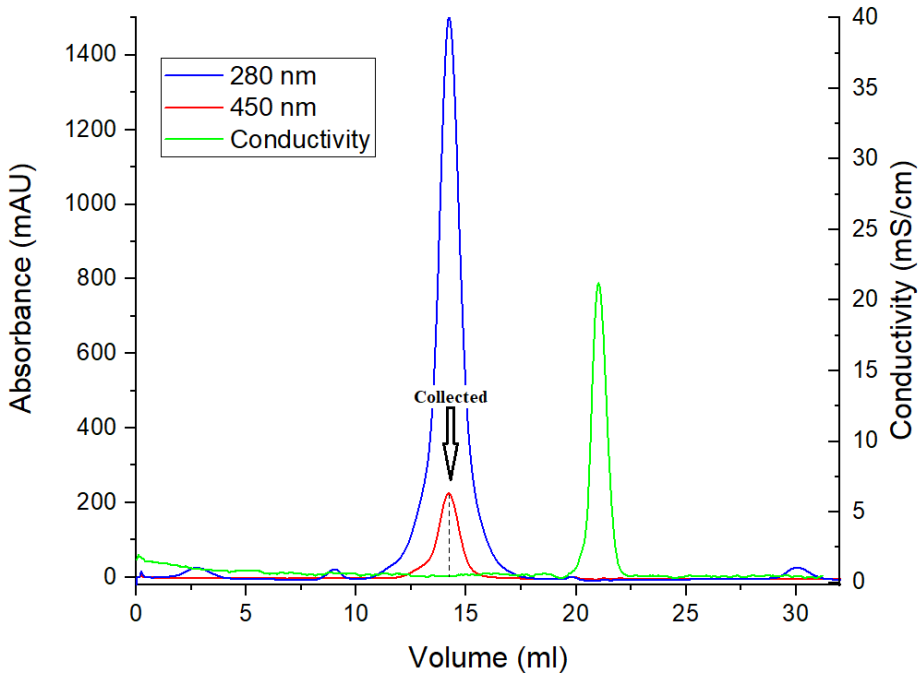

Figure 3.5. Chromatogram from the first round of GF chromatography. Arrow indicating the collected peak, which was split in two halves for SDS-PAGE analysis.

When collecting the fractions corresponding to the $FNR2_{mut}$ elution, the peak was split in two parts corresponding to the first and second halves of the peak and kept separate for SDS-PAGE analysis and concentration. The results from the SDS-PAGE analysis are shown in figure 3.6.

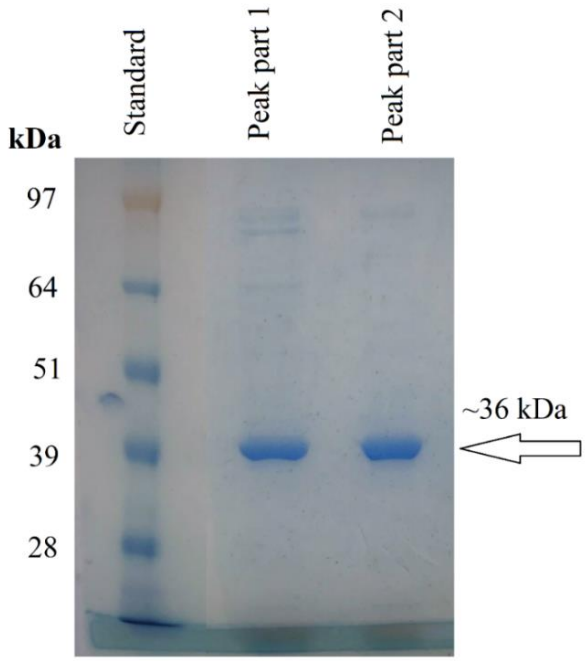

Figure 3.6. SDS-PAGE results after first round of GF chromatography. Eluted protein peak was split in two parts, peak part 1 and peak part 2. Arrow indicating the molecular weight corresponding to the $FNR2_{mut}$.

The SDS-PAGE results show that the $FNR2_{mut}$ is present in both halves of the peak, as expected, and the purity of the two parts appear mostly similar with an estimation of 1-2% more contamination in the first half of the peak. The purity of the protein sample after IEX and GF chromatography was estimated to be 95-99%, which corresponds to a clear excess of the $FNR2_{mut}$ and a very pure sample. In order to obtain an even purer sample, an additional step of purification could be included, or the chromatographic procedures could be further optimized. Due to loss of protein because of precipitation during the purification and concentration, no further purification procedures were performed. After the GF chromatography procedure, another attempt was made to concentrate the protein sample by centrifugation, this time with less precipitation. After purification and concentration of the sample, the $FNR2_{mut}$ concentration was estimated to be 9.72 mg/ml, using UV-vis spectroscopy and Beer-Lambert law.

To investigate if the protein would be more stable at a different pH, the rest of the protein from the first round of bacterial growth and precipitation was purified using the same procedures, however, by adjusting the pH of all buffers from 8.0 to 7.5 (D-F, Appendix 3). In addition, instead of DTT, TCEP was used as reductant in all buffers. Figure 3.7 shows the resulting chromatogram from this second round of IEX chromatography.

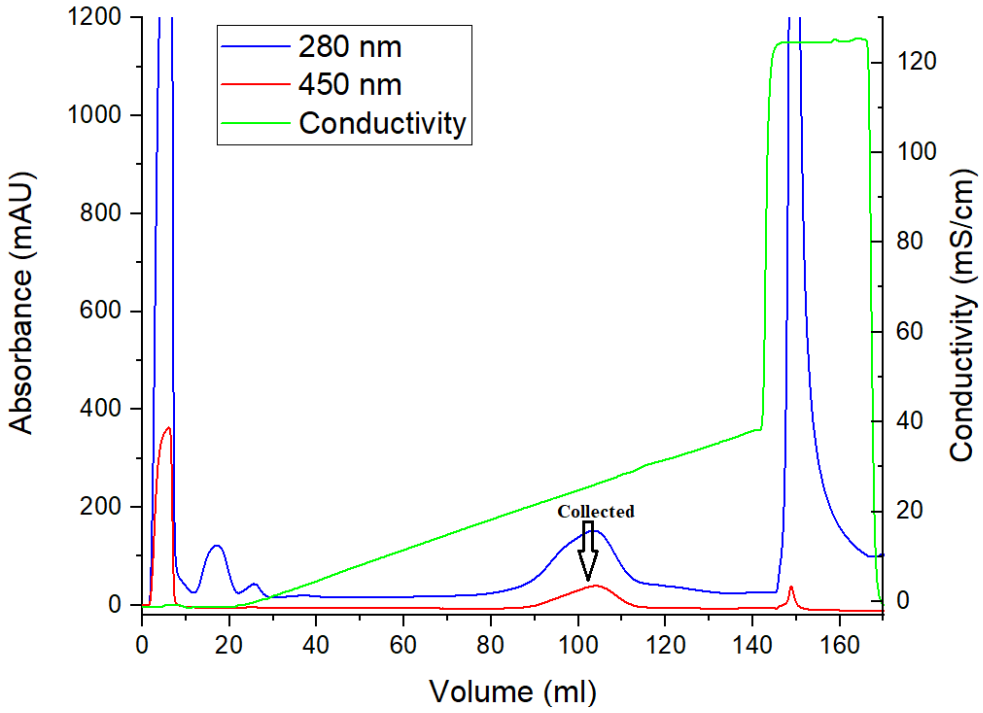

Figure 3.7. Chromatogram from the second round of IEX chromatography using Buffers D and E. Black arrow indicating the collected peak.

In this second round of IEX chromatography, the $FNR2_{mut}$ eluted at 21-27% buffer E (90-113 ml). The chromatogram indicates that less contaminant protein bound to the column when adjusting the pH, with the flowthrough peak being much higher than for the first IEX chromatogram for both 280 nm and 450 nm. After the first two runs of IEX chromatography, as for the first purification procedure, an SDS-PAGE analysis was performed to investigate the flowthrough and the collected fractions (figure 3.9A). The collected fractions from all IEX chromatography runs were again concentrated by centrifugation, and there was no change in the extent of protein precipitation. The sample could therefore not be concentrated to the preferred degree, and much of the protein was lost during the concentration process. It was also observed that the protein continued to precipitate during the GF chromatography procedure, and therefore had to be filtrated several times during the GF chromatography procedure to avoid application of precipitated protein onto the GF chromatography column. These observations indicate that the $FNR2_{mut}$ did not show any increased stability at this pH, nor by changing the type of reducing agent. The SDS-PAGE results in figure 3.9A confirm elution of the protein in the collected fractions from IEX chromatography, with mostly the same number of contaminants as for the first round of purification, but with appearance of a small and clear band closer to the FNR2 size.

Figure 3.8 shows the resulting GF chromatogram using the collected fractions from the second round of IEX chromatography. This chromatogram is different from the first GF purification round by the appearance of two peaks corresponding to absorption at 450 nm.

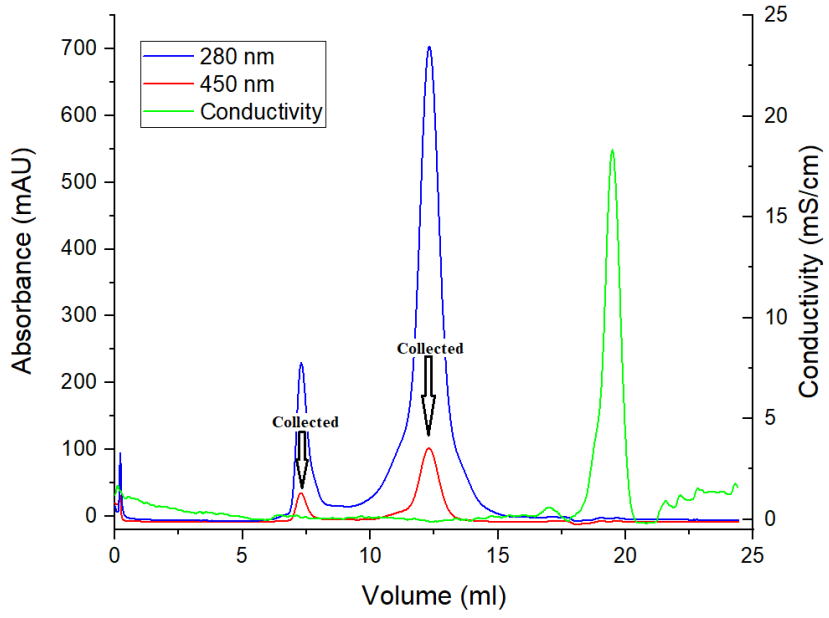

Figure 3.8. Chromatogram from the second round of GF chromatography using Buffer F. Arrows indicating the collected peaks corresponding to 450 nm absorption.

Fractions including both peaks in figure 3.8 were collected and analyzed by SDS-PAGE with results shown in figure 3.9B. It is clear that there is a large excess of the $FNR2_{mut}$ in the collected fractions, but the amount appears to be smaller in the first peak than in the second larger peak. The first peak consists of proteins too large to be retained by the column material, and most likely include aggregates and multimers of denatured $FNR2_{mut}$ protein.

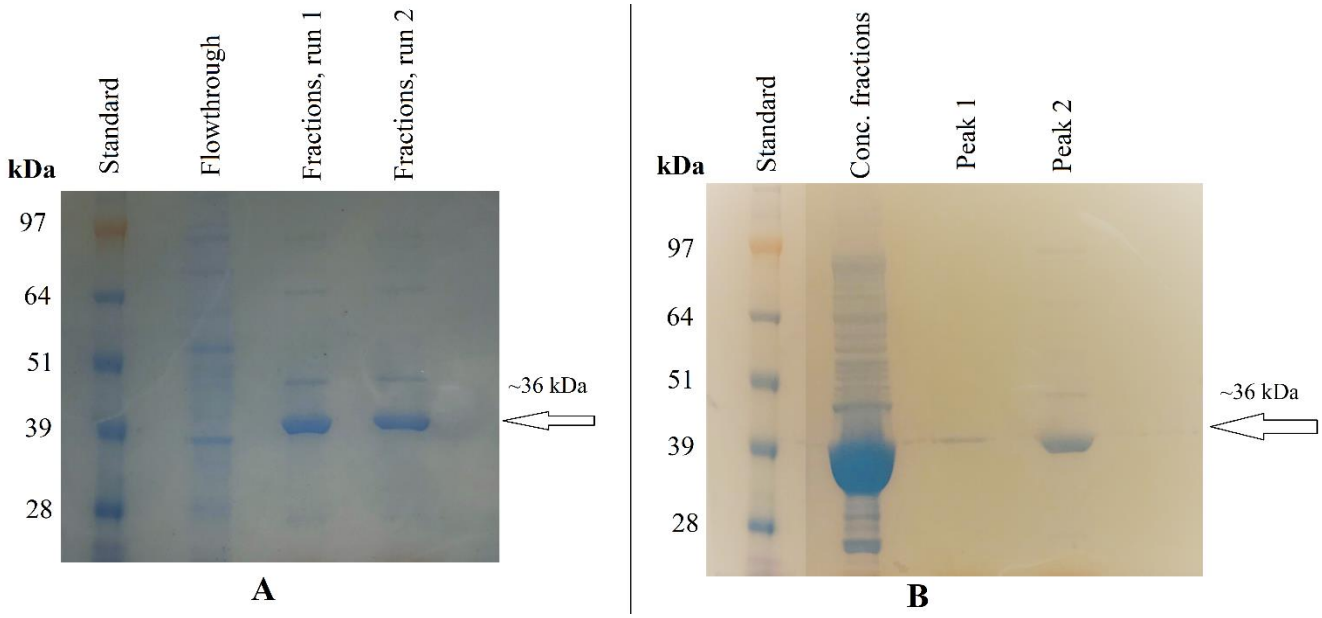

Figure 3.9. Results from the SDS-PAGE analysis performed after the second round of protein purification, using buffers with pH 7.5 and TCEP as reducing agent. A) SDS-PAGE results using fractions collected from run 1 and run 2 of IEX chromatography. B) SDS-PAGE results from GF chromatography, with the two collected 450 nm peaks separate, and conc. fractions corresponding to the concentrated fractions corresponding to peak 2.

After purifying the protein with GF chromatography, the collected fractions from both peaks were concentrated by centrifugation separately, and as for the first round of protein purification, there was less precipitation of protein during concentration after GF chromatography. The reason for the reduced precipitation after the last purification step remains unknown, but one possible explanation could be that some other contaminants in the sample contributed to the $FNR2_{mut}$ instability, and could have been removed during GF chromatography, leading to a small increase in the stability of the protein. Another possible explanation for the low stability of the protein could be the successive freezing of the sample between the different purification steps. After the purification procedures and concentration, the $FNR2_{mut}$ concentration in the sample was estimated to be 24.1 mg/ml. After these two rounds of protein purification, using protein expressed in the same round of bacterial growth, the $FNR2_{mut}$ yield was estimated to be 2.03 mg/L cell culture.

In an attempt to get answers regarding the stability of the $FNR2_{mut}$, nanoscale differential scanning fluorimetry (nanoDSF) was performed on the resulting purified protein after the first round of purification. NanoDSF is a method for determination of melting points/thermal stability of proteins, where the stability is given by the proteins' resistance against denaturation by thermal unfolding [76]. Because of the *B. cereus* FNR2 normally existing as a dimer, it could not be concluded from the nanoDSF results if the melting points indicated was due to actual denaturation of the protein, or the separation of protein dimers. Therefore, the results were inconclusive and is not included in this thesis.

In the last attempt to find better conditions for protein purification, another colony of transformed bacteria was picked for a new round of protein expression. The same procedure for bacterial growth and protein overexpression was used, but the expression cultures was incubated at lower temperatures (18.5˚C) overnight. After harvesting and lysating the bacteria, the $FNR2_{mut}$ was again precipitated at 0.2 g/ml ammonium sulfate before further purification by IEX and GF chromatography. The resulting protein pellets after precipitation appeared to have a stronger yellow colour than the pellets obtained after the first round of bacterial growth and protein precipitation. This could indicate that more holoprotein had been expressed under these growth conditions, and that reducing the temperature in the expression cultures led to the protein production not being too efficient compared to the FAD production. The resulting protein pellets were dissolved in Buffer G and desalted by dialysis overnight using Thermo Scientific SnakeSkin Dialysis Tubing filters (10K MWCO).

For the third and last round of protein purification, all Tris-HCl buffers were replaced with HEPES-KOH, pH 7.5. Because of the apparent increase in $FNR2_{mut}$ stability after GF chromatography in the previous purification rounds, using HEPES in the buffers, an attempt was made to see if maybe the protein would be more stable with the use of HEPES buffers during the whole purification process. In addition, and attempt was made to avoid freezing of the protein between the purification steps.

The last round of IEX chromatography was performed using Buffers G and H (Appendix 3), containing HEPES and with pH 7.5. The protein eluted at 16-23% Buffer H (85-110 ml) and the absorbance at 450 nm seemed to contain two possible overlapping peaks, as shown in figure 3.10. For this round of IEX chromatography, the 450 nm absorption is higher than for the second purification round (150 mAU vs. 50 mAU), while the peaks in the IEX chromatograms stretches

over approximately the same volume (~25 ml vs. 23 ml). This may indicate presence of more protein than for the first and second rounds of purification.

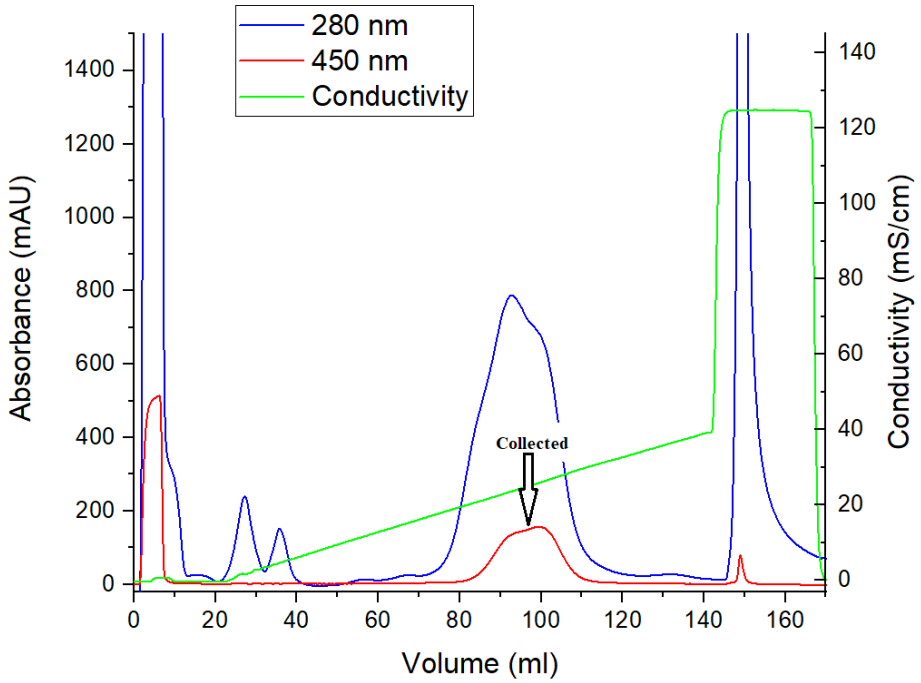

Figure 3.10. Chromatogram from the third round of IEX chromatography using Buffers G and H. Black arrow indicating the collected peak.

The collected fractions from IEX chromatography were concentrated by centrifugation, and again, extensive precipitation was observed, indicating that the use of HEPES buffers did not contribute considerably to the stability of the $FNR2_{mut}$ protein. Instead of freezing the protein sample in liquid nitrogen and storage at -80˚C, the resulting protein sample was kept thawed on ice in a cold room (~4˚C) overnight before continuing with GF chromatography.

Before starting the last round of GF chromatography, the protein sample was filtrated by centrifugation before application onto the GF chromatography column. The extensive precipitation made it difficult to get the protein sample through the filters, and a lot of protein was lost during the filtration and purification procedures. The protein sample was then loaded onto the GF chromatography column with Buffer I (Appendix 3) as running buffer. The chromatogram in figure 3.11 shows that the protein eluted as a single peak, but it is clear from the absorption at 280 nm that there is an overlapping peak present on the left side of the 450 nm absorption, that could lead to inclusion of contaminant proteins in the collected fractions. Therefore, when collecting the fractions corresponding to 450 nm absorption, the peak was split in two halves and analyzed by SDS-PAGE (figure 3.12).

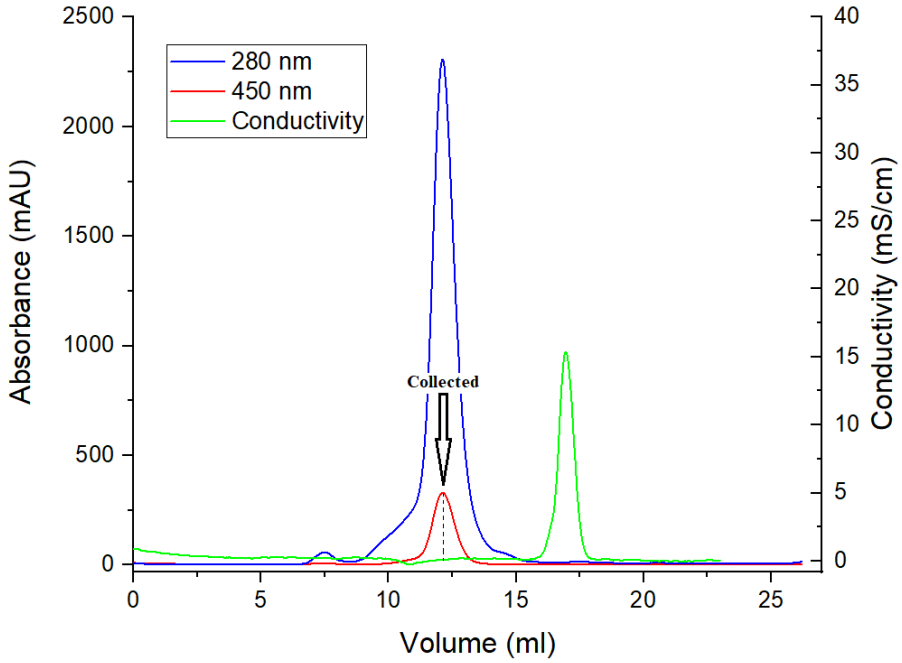

Figure 3.11. Chromatogram from the third round of GF chromatography with Buffer I, using the collected fractions from the third round of IEX chromatography. Arrow indicating the collected peak, which was split in two halves for an SDS-PAGE analysis.

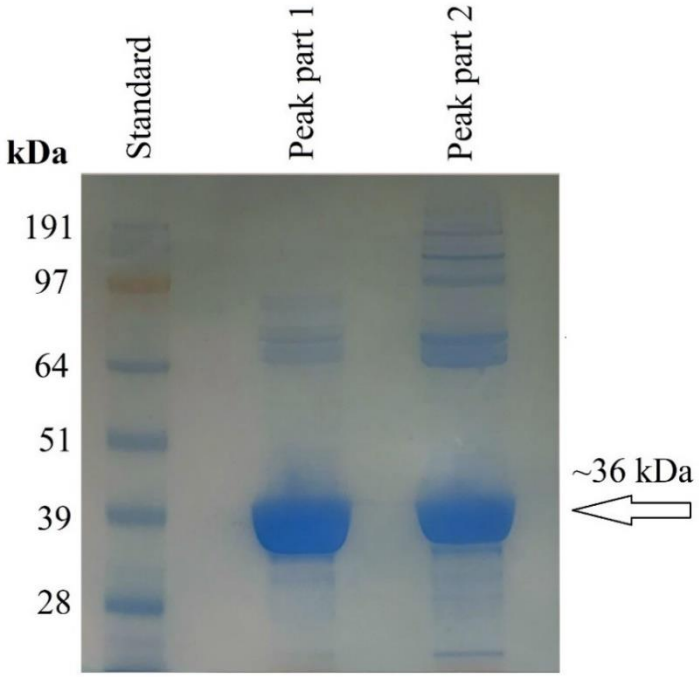

Figure 3.12. SDS-PAGE results after the last round of GF chromatography. The resulting protein peak was split in two halves, referred to as part 1 and part 2, respectively.

From the SDS-PAGE results shown in figure 3.12, it is clear from the large bands corresponding to ~36 kDa, that the protein sample contain an excess of the $FNR2_{mut}$. While the chromatogram in figure 3.11 indicates an overlapping peak that might include more contaminant proteins in the first half of the peak, the SDS-PAGE results show the opposite. Both halves of the protein

peak show satisfactory purity, but the second half of the peak contain some more contaminants than the first. The reason for more contaminant proteins eluting in the second half of the peak cannot be explained from the chromatogram or the SDS-PAGE results.

The collected fractions were concentrated, and again, the $FNR2_{mut}$ seemed to be more stable with less precipitation during the concentration process. After the purification and concentration procedures, the $FNR2_{mut}$ concentration was estimated to be 56.9 mg/ml, resulting in a protein yield of 7.9 mg/L cell culture after this second round of protein expression. This concentration and protein yield is considerably higher than seen after the two first rounds of protein purification and may indicate that the protein is, in fact, slightly more stable using only HEPES buffers since less protein has been lost to precipitation compared to the first two purification rounds. The higher protein yield could also indicate that more protein was expressed in the second round of protein expression, using lower temperatures. The purified protein sample was again stored in ice at ~4˚C overnight before an attempt was made to set up crystal screens.

During the last purification procedure, one sample was collected after each purification step to perform a nativePAGE analysis, hoping to obtain information considering the oligomerisation state of the FNR2 mutant. These results are shown in figure 3.13

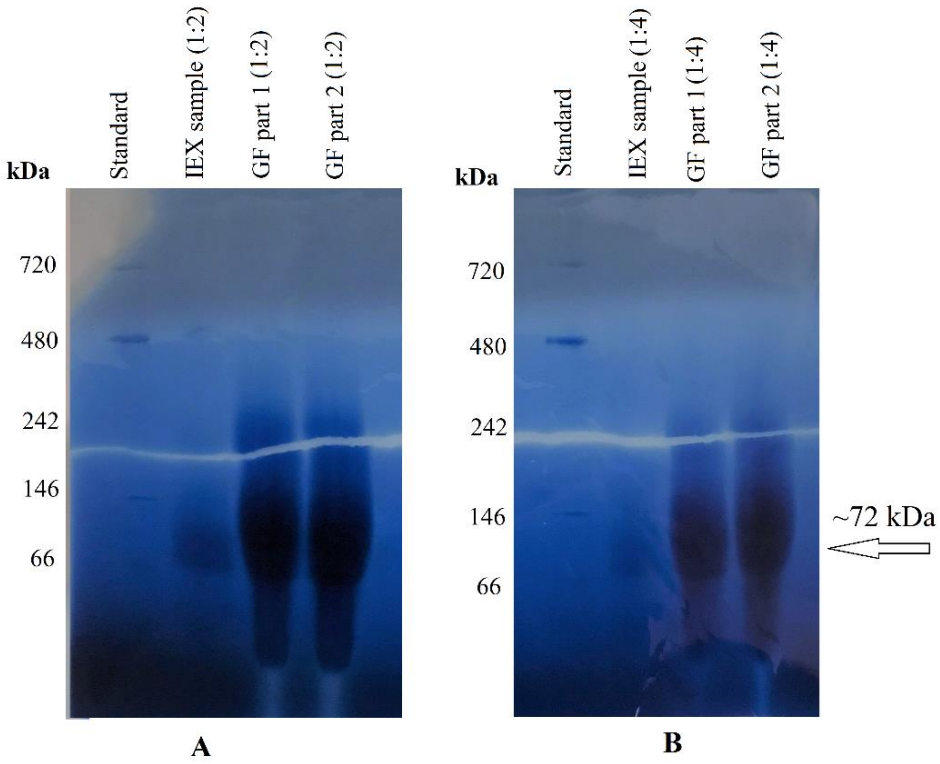

Figure 3.13. NativePAGE results using protein sample after the last round of purification. Protein peak collected from GF chromatography is split in two parts, called GF part 1 and GF part 2. A) All protein samples diluted 1:2, B) All protein samples diluted 1:4.

The nativePAGE results indicate some overloading, despite all protein samples being diluted (1:2 and 1:4) before loading onto the gel. The results show that there is a large excess of protein with molecular weight between 66 and 146 kDa, corresponding to the FNR2 dimer size (~72 kDa). There is no apparent difference between the two parts of the peak collected after GF chromatography. However, diluting the sample even more before nativePAGE could have given clearer results and could indicate more clearly if there also is FNR2 monomers present in the samples. Despite the overloading of the gel, it is clear that the centre of the band corresponding to the FNR2 is of the expected dimer size.

3.3 Protein crystallization

After purification of the $FNR2_{mut}$ and estimation of protein concentration by UV-vis spectroscopy, the protein samples were further used for setting up crystal screens in attempts to obtain protein crystals suitable for X-ray diffraction. An overview of the different screening experiments, including the corresponding $FNR2_{mut}$ concentration, type of crystallization screen and hits, are shown in table 3.1.

Table 3.1. Overview showing the different crystallization screen experiments.

Purification round	Protein conc.	Screen	Hits
1	9.72 mg/ml	Morpheus, JCSG+, Index, PGA	No hits
2	24.1 mg/ml	Morpheus, JCSG+	Morpheus: D10, D11, E10, E11, F10, F11, H11 Needles
2	12.2 mg/ml	Morpheus, JCSG+	Morpheus: D10, D11, E10, E11, F10, F11, H11 Needles
3	57 mg/ml	Morpheus	Morpheus: B10, D10, E10, F10, H11 Needles

The first purified protein sample had $FNR2_{mut}$ concentration 9.72 mg/ml, and because of the concentration being relatively low, only one protein condition was used to set up crystals after this round of purification. After several weeks, none of the crystal screens showed any crystal formation by using this concentration. It was suspected that the lack of crystal formation could be due to the apparent protein instability observed during the purification procedures.

The resulting $FNR2_{mut}$ concentration after the second round of protein purification was estimated to be 24.1 mg/ml. When setting up crystal screens using this purified sample, two different conditions (24.1 mg/ml and 12.2 mg/ml) were used to investigate if the protein would crystallize at lower concentrations despite no crystals being formed in the first screen using low $FNR2_{mut}$ concentration. After 1-2 weeks, small needle shaped crystals were observed for both protein concentrations in the Morpheus conditions (Appendix 4) listed in table 3.1. A selection of the resulting crystals after this crystal screen is shown in figure 3.14.

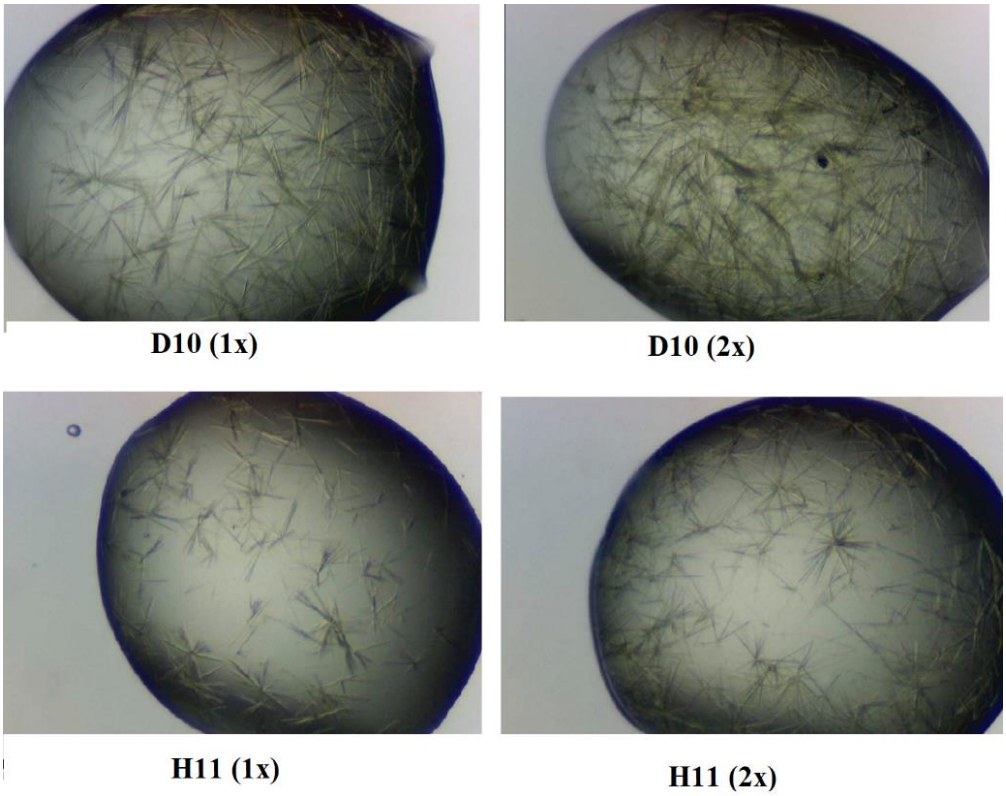

Figure 3.14. A selection of protein crystals resulting from the Morpheus screen after the second crystallization screen. 1x corresponds to crystallization without dilution of the purified sample. 2x corresponds to 50:50 dilution of the purified sample with mqH_2O.

After a new round of protein expression and purification, the resulting purified and concentrated protein sample had an estimated $FNR2_{mut}$ concentration of 57 mg/ml. Since small crystals had been obtained with low protein concentrations in the previous crystal screen, an attempt was made to crystallize the $FNR2_{mut}$ at a higher concentration. One protein condition was therefore used in a crystallization screen using only the Morpheus screen, and after 1-2 weeks, crystals was observed in the crystallization conditions listed in table 3.1. These results gave crystal hits in many of the same conditions as for the previous screening, and a selection of the resulting crystals from the last screening is shown in figure 3.15. There are no clear differences in the type of crystals formed or the crystal size in the different precipitant solutions, with all the

resulting crystals having a needle-shape and with the largest crystals estimated at size ranging from 10-60 µm.

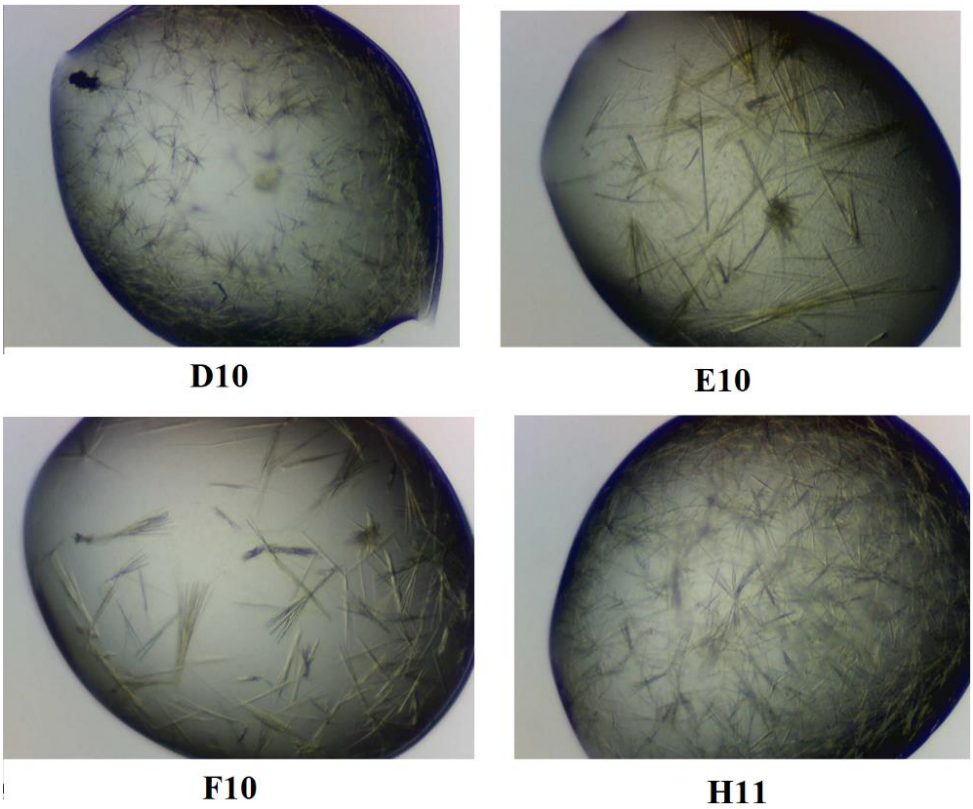

Figure 3.15. A selection of protein crystals resulting from the third crystallization screen, using only one protein condition (57 mg/ml). All results are from the Morpheus screen (Molecular Dimensions).

By looking at the content of the crystallization conditions resulting in crystals (table 3.2) there are some similarities between the different conditions, as well as some differences. The $FNR2_{mut}$ crystallized in the presence of halogens, alcohols, ethylene glycols, monosaccharides, and amino acids, so no conclusion considering the most suitable additives/ligands for $FNR2_{mut}$ crystallization can be drawn from these results. Among the different precipitant mixes, the protein crystallized by using precipitant mix 2 and 3, containing ethylene glycols with PEG 8000 and glycerol with PEG 4000, respectively. Both precipitant mixes have 40% v/v additive as well as 20% w/v PEG solution, but otherwise few similarities that may be used to explain the successful crystallization in these specific mixes. All the conditions resulting in crystal formation have pH 8.5 and include buffer system 3 (Appendix 4). This buffer system contains Tris, and there are no crystals resulting from buffer systems containing HEPES (Buffer system 2). This could point in the direction of concluding that the reason for the $FNR2_{mut}$ instability was not the use of Tris-buffers, strengthening the observations that exchanging all Tris-buffers for HEPES-buffers in the last purification round did not improve the stability of the protein considerably.

Table 3.2. Overview of the crystallization conditions resulting in $FNR2_{mut}$ crystal formation.

Well	Conc	Ligands	[Ligands]	Buffer	[Precipitant]	pH	Precipitant
B10	0.09 M	Halogens	0.1 M	Buffer system 3	30 % v/v	8.5	Precipitant mix 2
D10	0.12 M	Alcohols	0.1 M	Buffer system 3	30 % v/v	8.5	Precipitant mix 2
D11	0.12 M	Alcohols	0.1 M	Buffer system 3	30 % v/v	8.5	Precipitant mix 3
E10	0.12 M	Ethylene glycols	0.1 M	Buffer system 3	30 % v/v	8.5	Precipitant mix 2
E11	0.12 M	Ethylene glycols	0.1 M	Buffer system 3	30 % v/v	8.5	Precipitant mix 3
F10	0.12 M	Monosaccharides	0.1 M	Buffer system 3	30 % v/v	8.5	Precipitant mix 2
F11	0.12 M	Monosaccharides	0.1 M	Buffer system 3	30 % v/v	8.5	Precipitant mix 3
H11	0.1 M	Amino acids	0.1 M	Buffer system 3	30 % v/v	8.5	Precipitant mix 3

From a selection of the screening conditions resulting in crystals, and optimization experiment was set up in attempts to obtain bigger $FNR2_{mut}$ crystals more suitable for X-ray diffraction (table 2.4). None of the optimization experiments resulted in crystal formation. The reason for the lack of crystals formation in the optimization experiments is unknown, but possible reasons for the lack of results could be the additional freezing and thawing of the protein samples, presence of precipitated protein in the samples, or because of the precipitation solutions not being optimal for nucleation and crystal growth.

The resulting crystals from the screenings were not of the preferred size and shape for X-ray diffraction, and often, crystals obtained from crystallization screenings are insufficient for data collection without any optimization [77]. An alternative solution to these problems could be to perform a seeding experiment on the already obtained small crystals, and thereby obtain bigger crystals more suitable for X-ray diffraction. Seeding is a technique commonly used when nucleation is slow, to increase the size of crystals or when crystals grow in clusters as can be seen in the crystal figures (figure 3.12 and 3.13). In seeding, a small crystal can be isolated and used as a growth surface, resulting in a bigger crystal without the need of new nuclei being formed. Because of the nucleation process being a kinetically demanding step, molecules may prefer to accumulate one the introduced small crystal [78]. Due to time considerations, no seeding experiments were performed in this project, and the crystals obtained from Morpheus

conditions H11 (second screening) and F10 (third screening) was frozen directly in liquid nitrogen, since the Morpheus conditions are already cryo-conditions, and used for X-ray diffraction.

3.3.1 Solving the FNR2 mutant structure

After freezing the $FNR2_{mut}$ crystals resulting from the Morpheus conditions F10 and H11, diffraction data was collected at The European Synchrotron Radiation Facility (ESRF) in Grenoble, France. The protein crystals gave poor diffraction, probably due to the small size and shape, but the diffraction data was still used further in attempts to solve the $FNR2_{mut}$ structure.

The diffraction data was auto-processed (indexed and integrated) with autoPROC and XDS through the MxCube software system at the ESRF [69]. From the resulting auto-processed diffraction data obtained from the different crystals, the one with the best apparent resolution was chosen for data reduction process using Aimless (CCP4 software package)[70]. To obtain acceptable scaling statistics, the resolution was cut at 4.90 Å, and both the space group $P2_12_12$ and $P2_12_12_1$ was suggested with an R_{meas} value of 0.169. From the attempts of solving the structure with molecular replacement it was concluded that the correct space group was $P2_12_12_1$.

An attempt was made to solve the structure by basic Molecular Replacement with Phaser [71], searching for four copies of the entire protein structure with the $FNR2_{wt}$ as a model, as the unit cell content analysis indicated 4-5 monomers. The software failed to identify the structures from the diffraction data, leading to a new attempt to solve the structure by using Expert Mode Molecular Replacement with Phaser, here, searching for four copies each of the single domains (FAD-binding and NADPH-binding domains). From these results, it could be observed by visualization in PyMOL that the different domains displayed different orientations, with both the previously observed FNR2 rotation (here referred to as the classical FNR2 rotation) as well as a new orientation of the NADPH-binding domain within the same crystal (figure 3.16).

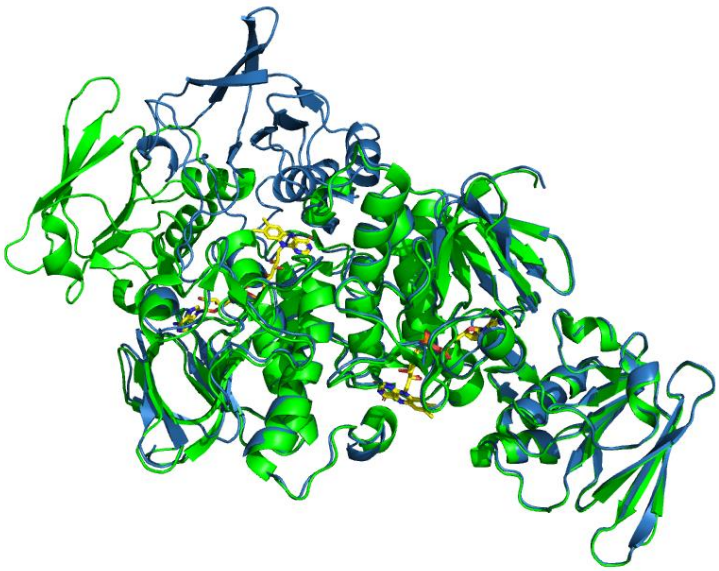

Figure 3.16. Overlay of the $FNR2_{mut}$ and the $FNR2_{wt}$ structures, illustrating the difference in NADPH-binding domain orientation in one of the monomers. The $FNR2_{mut}$ is shown in marine blue and the $FNR2_{wt}$ is shown in green.

After manually connecting the NADPH-binding domain showing the new orientation with the corresponding FAD-binding domain, making a new alternative protein monomer, another round of Expert Molecular Replacement was performed by searching for two copies of the alternative monomer and two copies of the classical FNR2 monomer. Resulting *R*-factor and R_{free} was 0.334 and 0.396, respectively.

The four monomers were not oriented as biological dimers in the asymmetric unit, so the asymmetric unit was adjusted by using symmetry equivalents in PyMOL. This updated structure was used for a round of refinement in REFMAC5 with 20 cycles [79], using both jelly-body restraints and non-crystallographic symmetry restraints, resulting in *R*-factor 0.35 and R_{free} 0.43. Model building was performed using Coot [80], and positive difference electron density was observed in the FAD binding site of the monomers with the classical orientation of the NADPH-binding domain, while there was no positive difference density corresponding to the FAD cofactor in the alternative monomers with a different rotation of the NADPH-binding domain. This indicates that some of the protein in the crystal was in fact apoprotein. As a consequence of these observations, the FAD cofactor was not included in the monomers with the new NADPH-domain rotation due to lack of FAD density. Figure 3.17 shows the area where the FAD cofactor was expected to bind in the monomer with the alternative rotation. From figure 3.17A, showing the electron density map as well as the difference maps, it can be observed that the density corresponding to the FAD cofactor is missing. Figure 3.17B shows the expected placement of the FAD cofactor in the alternative monomer, if present.

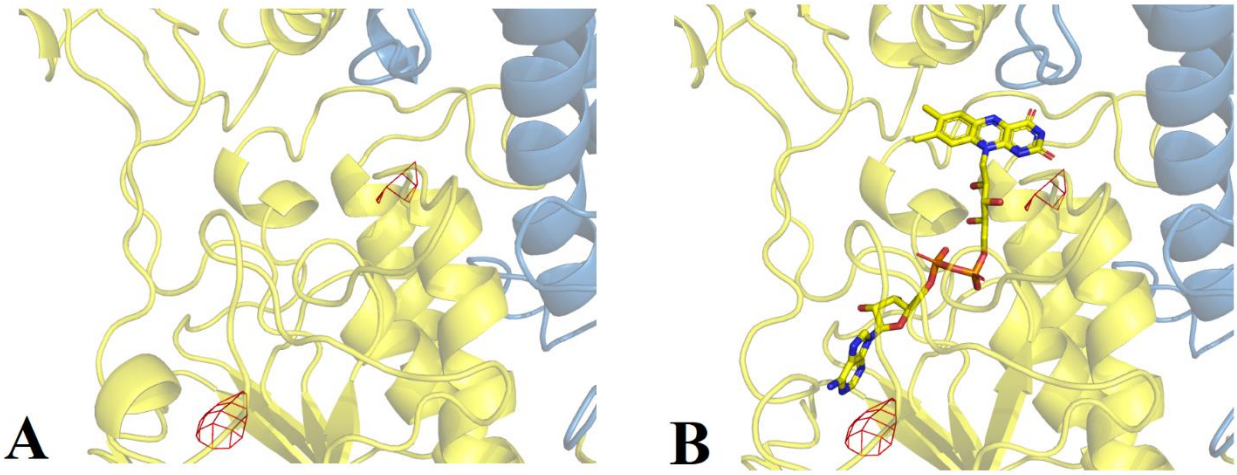

Figure 3.17. FAD-binding domain in monomer with alternative rotation of the NADPH-binding domain of the $FNR2_{mut}$ structure. Figure shows the electron density map contoured at 1σ and the electron difference density maps (fo-fc) coloured in green and red respectively and contoured at +3σ and -3σ around the FAD cofactor A) The missing density corresponding to the FAD cofactor in the alternative monomer. B) The expected placement of the FAD cofactor in the alternative monomer, if present.

After a new refinement using the updated structure, the resulting *R*-factor and R_{free} was 0.29 and 0.40 respectively, which is a reduction in the values indicating that the $FNR2_{mut}$ structure is now a better fit to the diffraction data than the initial structure.

Further, the amino acids were checked to investigate for potential wrong rotamers or if adjustment were required to fit the structure into the electron density. In addition, His326 was manually mutated into Val in the $FNR2_{mut}$ structure, although the resolution was too low to distinguish the difference in density between His and Val. Due to the low quality of the diffraction data, some areas of the protein structure had poor electron density and the low resolution made it difficult observe the correct position of the amino acid side chains. Therefore, making a structure with perfect fit to the electron density proved difficult.

As a last step in the structure solving, water was added, and the structure was validated by investigating the Ramachandran plot and geometry analysis. In the final structure, the Ramachandran plot showed 85.80% in preferred regions, 11.73% in allowed regions, while 2.47% of the residues were outliers without any clear adjustment possible. There were no geometry violations in the final structure. After the last refinement, the resulting *R*-factor and R_{free} values were 0.28 and 0.38, respectively. As the *R*-factor of well-refined structures is generally expected to be 0.2 or lower, depending on the resolution, it is clear that the $FNR2_{mut}$ structure was solved based on poor diffraction data with low resolution [65]. The solved structure of the FNR2 His326Val mutant is shown in figure 3.18, and the data collection parameters as well as the refinement statistics are listed in table 3.3.

Table 3.3. $FNR2_{mut}$ crystal data collection and refinement statistics

Data collection	**$FNR2_{mut}$**
X-ray source	ID30B (ESRF)
Wavelength (Å)	0.9763
Space group	$P2_12_12_1$
a, b, c, (Å)	71.9, 105.1, 216.9
α, β, γ (degrees)	90, 90, 90
Resolution range (Å)	94.6 – 4.9 (5.5 – 4.9)
Mosaicity (degrees)	0.22
Number of observations	44174 (12777)
Number of unique reflections	8016 (2237)
R_{meas}	0.169 (0.910)
R_{merge}	0.152 (0.824)
I/σ(I)	7.9 (2.7)
Completeness (%)	99.8 (100.0)
$CC_{1/2}$	0.996 (0.855)
Multiplicity	5.5 (5.7)
Refinement Statistics	
R_{work}	0.28
R_{free}	0.38
Mean overall isotropic B factor ($Å^2$)	226
Protein residues in gene	331
Protein assembly in asymmetric unit (AU)	4 monomers
Protein residues modelled	326
Modelled ligands	2 FAD
Added waters	7
Ramachandran plot (favoured/allowed/disallowed) (%)	85.8 / 11.7 / 2.5
RMSD bond lengths (Å)	0.002
RMSD bond angles (degrees)	1.350
Estimated overall coordinate error based on maximum likelihood (Å)	2.2

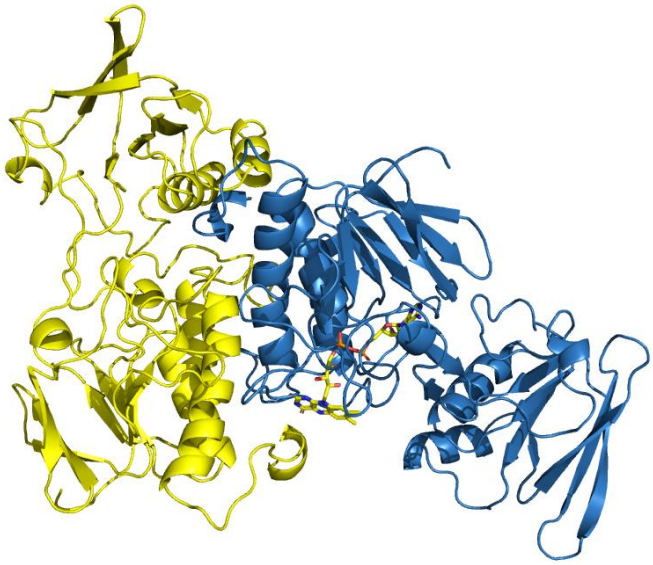

Figure 3.18. Final refined $FNR2_{mut}$ structure. Monomer with a new rotation of the NADPH-binding domain shown in yellow, and the monomer with the classical FNR2 rotation shown in blue, including the FAD cofactor shown in sticks.

From the final $FNR2_{mut}$ structure, the electron density map and the difference maps were exported and visualized around the FAD cofactor in PyMOL. Because of the diffraction data being of low quality, the resulting electron density map around the FAD cofactor was also poor, but it is clear that there is density corresponding to the FAD cofactor in one of the chains, but not in the other chain constituting the protein dimer. The electron density map and the difference maps around the FAD cofactor in the monomer with the classical FNR2 rotation of the NADPH-binding domain is shown in figure 3.19, where the carve of the electron density map is set to 2.0 (figure 3.19A) and 3.0 (figure 3.19B).

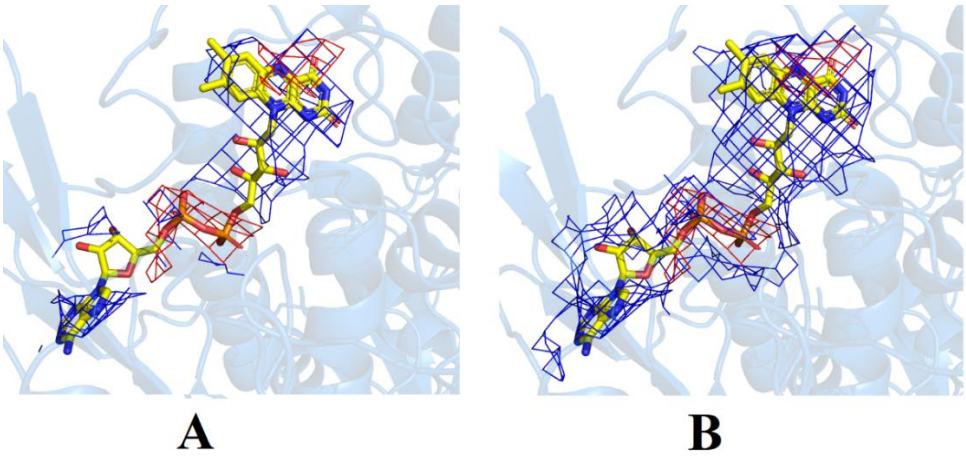

Figure 3.19. The electron density map (2fo-fc) coloured in blue and contoured at 1σ and the electron difference density maps (fo-fc) coloured in green and red respectively and contoured at +3σ and -3σ around the FAD cofactor in the resulting $FNR2_{mut}$ structure. Showed with 2fofc carve set to 2.0 (A) and 3.0 (B).

To verify the FAD electron density and justify the actual presence of the FAD cofactor in the monomers with the classical rotation, an omit map was calculated by removing the FAD cofactor from the PDB file before another round of refinement. Omit maps will exclude specific atoms in question from the model, in this case the FAD cofactor, and is therefore useful in verification of the ligand presence in protein structures [81]. An omit map was exported from the resulting structure, and the map display the electron density without the cofactor built into the model. The omit map in figure 3.20 shows that there is clear FAD density in the monomer with the classical FNR2 rotation, but not in the monomer displaying the new NADPH-binding domain rotation in the $FNR2_{mut}$ structure.

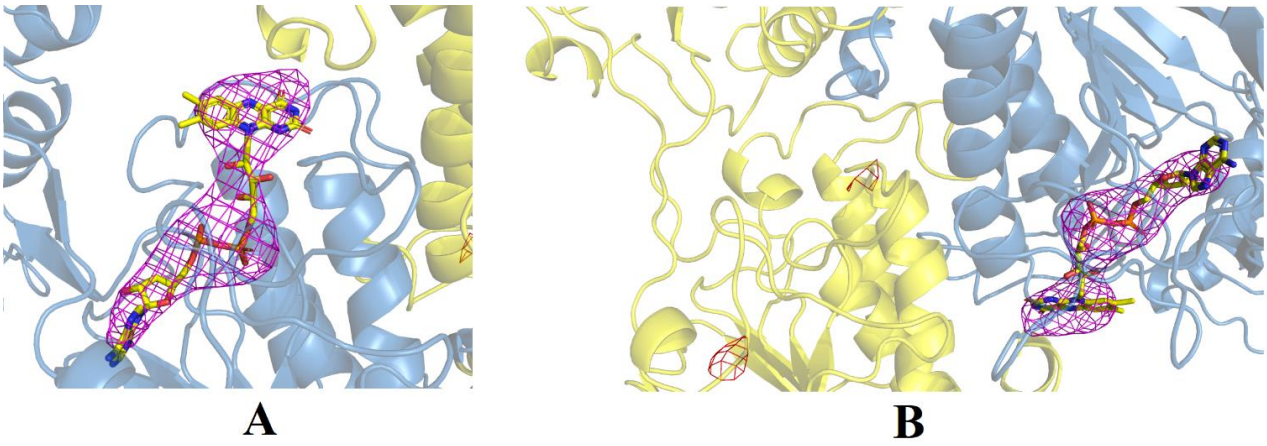

Figure 3.20. A) Omit-map surrounding the FAD cofactor in the $FNR2_{mut}$ monomer with classical rotation of the NADPH-binding domain, coloured in magenta and contoured at +3σ. B) Shows no electron density corresponding to the FAD cofactor in the $FNR2_{mut}$ monomer with a new rotation of the NADPH-binding domain (yellow cartoon).

3.3.2 Analysis of the structure

The resulting $FNR2_{mut}$ structure indicate some interesting findings considering rotation and FAD cofactor presence. As presented in the resulting structure figures, there are two different rotations of the NADPH-binding domain within the same crystal, where one monomer displays the classical FNR2 rotation while the other show a new alternative rotation. Another interesting observation is that the monomer with the alternative rotation has lost the FAD cofactor. Previous studies of TrxR-like FNRs have shown that the domains can rotate relative to each other and that different TrxR-like FNRs have crystallized in several different conformations. It is also previously shown that rotation between the FAD- and NADPH-binding domains most likely play an important role in the catalytical mechanism of TrxR-like FNRs, based on knowledge considering the distance between the NADPH-binding site and the FAD cofactor required for productive hydride transfer [16, 22]. It is therefore not surprising that different rotations may occur, but asymmetric rotation of the domains within a single dimer is not

considered to be a common feature in homodimeric FNRs. The only known observation of two different NADPH-domain rotations within a FNR homodimer was found by Muraki and co-workers, where the crystal structure of *C. tepidum* FNR had one NADPH-binding domain in closed conformation and the other in an open conformation [35]. Although a previous study has observed such asymmetric rotation of the domains in TrxR-like FNRs, this is not a common feature in the *B. cereus* FNRs and is most likely an effect caused by the His326Val mutation. However, it is not at this time possible to determine if the changed rotation is due to the loss of the FAD cofactor, or if the loss of the FAD cofactor is due to changed rotation caused by the introduced mutation. Thus, from the resulting structure of the $FNR2_{mut}$, it can be concluded that the mutation has influenced the protein structure, but the exact biochemical effect on the structure is still unclear. No conclusion can be drawn that the mutation induces a change in the rotation of the NADPH-binding domain, since this is only observed for some monomers, while others still have the FAD cofactor bound and display classical FNR2 rotation.

3.3.3 Solving the FNR1-$NADP^+$ co-crystallization structure

After data reduction using Aimless (CCP4 software package) with resolution cut at 4.50 Å, the resulting space group suggested was *I*2, which is different from the original FNR1 space group resulting in a different crystal packing. The resulting overall R_{meas} was 0.200. When solving the structure of the FNR1 co-crystallized with $NADP^+$, basic molecular replacement (Phaser) was performed by searching for the $FNR1_{wt}$ dimer. The resulting structure indicated a good fit with the FAD-binding domains, but there was positive green density indicating a different rotation of the NADPH-binding domains. Since no previous structures with this specific rotation was available, another round of basic molecular replacement was performed searching for eight copies of the NADPH-binding domain and four copies of the FAD-binding domain, resulting in the successful identification of the new NADPH/FAD binding domain orientation. The NADPH-binding domain showing the new orientation was manually connected with the corresponding FAD-binding domain, making a new alternative protein monomer. This structure was further used as starting model when performing a third round of molecular replacement searching for eight monomers, resulting in successful identification of four protein dimers. Based on this model, the structure of the FNR1 co-crystallized with $NADP^+$ was successfully solved. After adjustments of amino acid side chain rotamers and fitting the structure into the electron density, the resulting *R*-factor and R_{free} was 0.285 and 0.344, respectively. The structure was validated by investigating the Ramachandran plot and geometric analysis. The resulting Ramachandran plot had 74.8% in preferred regions and 15.9% in allowed regions, and there

were no geometry violations in the resulting structure. Due to the data showing low resolution, it proved difficult to model the structure correctly into the electron density with correct placement of all the amino acid side chains. The resulting solved FNR1 structure, as well as overlays with the previous solved FNR1 and FNR2 wild type structures, are shown in figure 3.21. The data collection parameters as well as the refinement statistics are listed in table 3.4.

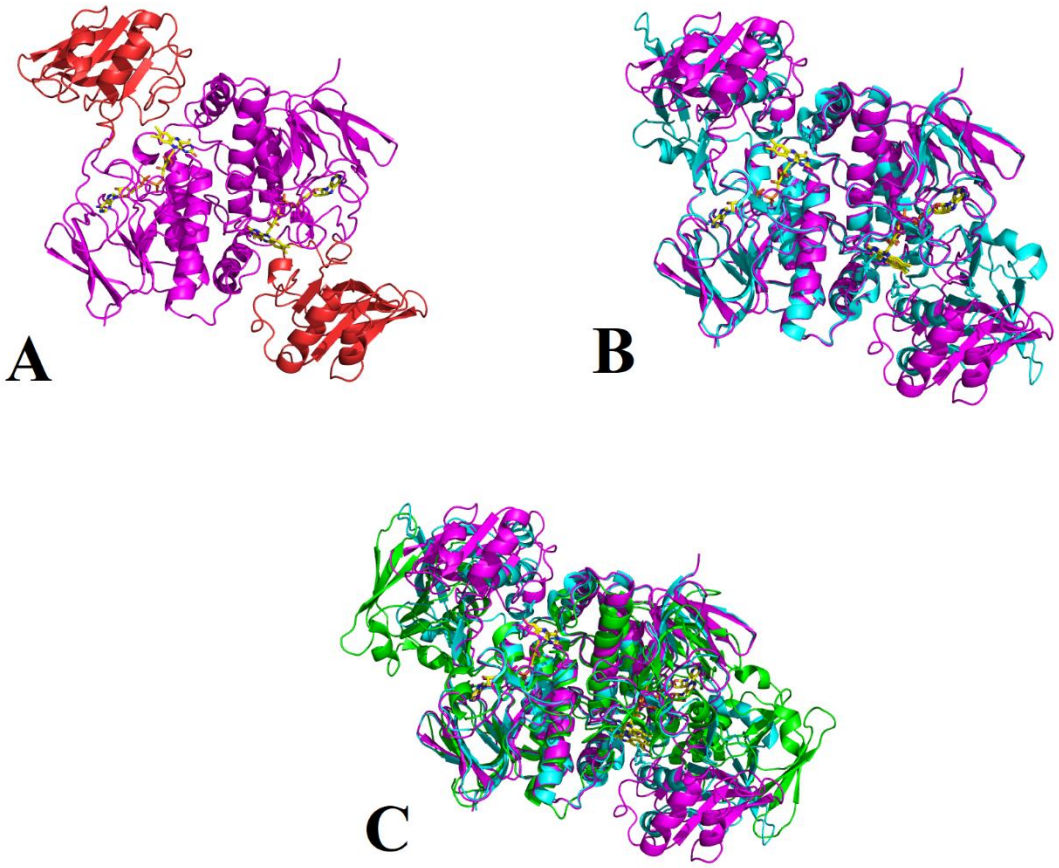

Figure 3.21. A) Solved structure of FNR1 co-crystallized with $NADP^+$, with NADPH-binding domains coloured in red and FAD-binding domains coloured in magenta. B) Solved FNR1 structure (magenta) in overlay with previously solved FNR1 structure (cyan), clearly showing different rotation of the NADPH-binding domain. C) Overlay showing the solved FNR1 structure, previously solved FNR1 structure and wild type FNR2 structure (green).

Table 3.4. Crystal data collection and refinement statistics for FNR1 co-crystallized with $NADP^+$

Data collection	**FNR1-$NADP^+$**
X-ray source	ID30B (ESRF)
Wavelength (Å)	0.9763
Space group	$I1_21$
a, b, c, (Å)	190.6, 215.8, 191.2
α, β, γ (degrees)	90, 111, 90
Resolution range (Å)	157.4 – 4.5 (4.7 – 4.5)
Mosaicity (degrees)	0.12
Number of observations	141578 (15565)
Number of unique reflections	42620 (4447)
R_{meas}	0.200 (1.651)
R_{merge}	0.168 (1.398)
I/σ(I)	4.6 (1.0)
Completeness (%)	99.6 (99.8)
$CC_{1/2}$	0.994 (0.486)
Multiplicity	3.3 (3.5)
Refinement Statistics	
R_{work}	0.29
R_{free}	0.34
Mean overall isotropic B factor ($Å^2$)	185.4
Protein residues in gene	349
Protein assembly in asymmetric unit (AU)	8 monomers
Protein residues modelled (per monomer)	345
Modelled ligands	8 FAD
Added waters	252
Ramachandran plot (favoured/allowed/disallowed) (%)	74.8 / 15.9 / 9.3
RMSD bond lengths (Å)	0.003
RMSD bond angles (degrees)	1.618
Estimated overall coordinate error based on maximum likelihood (Å)	1.2

It is clear, from the solved FNR1 structure co-crystallized with $NADP^+$, that the NADPH-binding domains have a different orientation than the previously solved structure of both FNR1 and FNR2. When investigating the structure, there was indication of positive difference density around the NADPH-binding domain that could correspond to $NADP^+$ bound in the structure. In attempts to verify that the positive density was due to $NADP^+$ binding, the FNR2 structure from *B. subtilis* with NADPH bound to the structure was imported to Coot, and the NADPH-binding domains of the two structures were aligned. It was observed that the phosphate groups of the NADPH molecules in *B. subtilis* FNR2 matched some of the positive difference density in three of the chains in the FNR1 structure, indicating that the density could belong to the co-crystallized $NADP^+$. When inserting the NADPH structure into the relevant areas of the FNR1 structure, followed by refinement (REFMAC5) the resulting *R*-factor and R_{free} was 0.290 and 0.345, respectively. The resulting structure showed negative difference density around the inserted NADPH molecule. The NADPH occupancy was set to 0.5 before a new round of refinement, resulting in *R*-factor 0.288 and R_{free} 0.344, a small reduction indicating a better fit. This step also reduced the amount of negative density around the inserted NADPH molecule, resulting in a somewhat unclear result. The overall electron density around the FAD cofactor in the solved FNR1 structure, as well as the electron density around the NADPH molecule in FNR1, based on the NADPH placement in *B. subtilis* FNR2, is shown in figure 3.22.

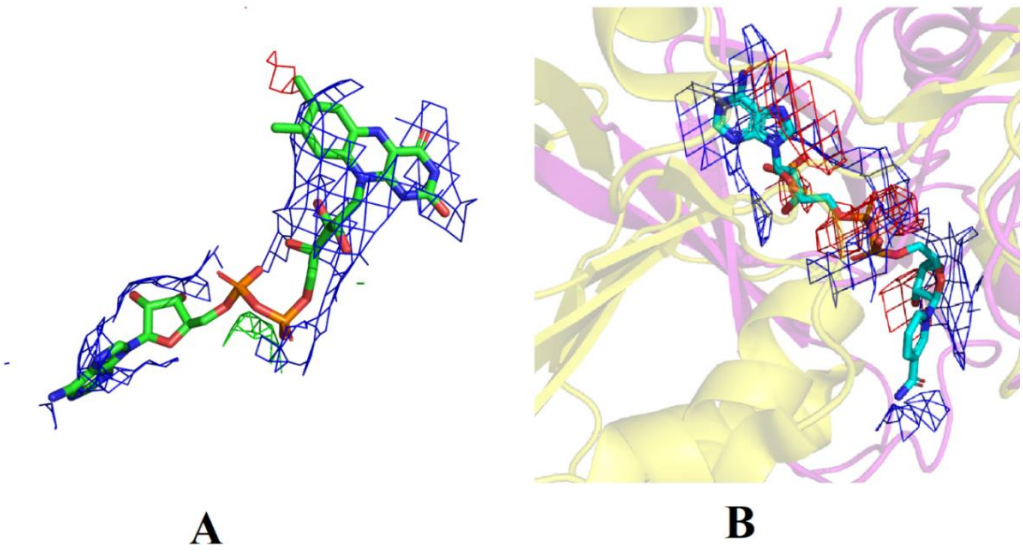

Figure 3.22. A) Electron density map (blue) contoured at 1σ as well as the difference density maps (green and red) contoured at +3σ and -3σ around the FAD cofactor of the solved FNR1 structure, respectively. B) The electron density map (blue) contoured at 1σ as well as the difference density maps (green and red) contoured at +3σ and -3σ around the NADPH-binding site in the solved FNR1 structure, respectively. *B. subtilis* FNR2 NADPH-binding site used as reference.

From investigation of the electron density in the resulting FNR1 structure co-crystallized with $NADP^+$, it was clear that there was some positive density in the area normally bound by NADPH before inserting the molecule into the structure. This green density also showed a satisfactory fit to the phosphates of the NADPH molecule, indicating that the NADPH had been successfully co-crystallized into the FNR1 structure. However, when modelling the NADPH molecule into the structure, the negative density appearing around the molecule may indicate the opposite. Thus, the results are not clear enough to conclude that the $NADP^+$ molecule has been successfully co-crystallized into the FNR1 structure, but the results show some indication that the experiment could be successful. The difficulties in analyzing the actual presence of the $NADP^+$ molecule in the structure is due to the low resolution and poor quality of the X-ray diffraction data.

3.4 Activity measurements

The FNR2 His326Val mutant activity was tested by performing several reactions with increasing substrate concentrations in the presence of NADPH, using both Fld-like protein NrdI and Fld1 from *B. cereus* as substrates in two separate assays. In addition, activity measurements with NrdI as substrate was performed using the $FNR2_{wt}$, to compare the efficiency of the mutant and the wild type enzyme. Alle reactions were, as described in section 2.9, performed in an anaerobic glovebox to prevent spontaneous re-oxidation of the substrates. During the experiments, the relevant wavelengths corresponding to λ_{max} for the oxidized and reduced forms of the substrates were investigated, and the resulting UV-vis spectroscopy data was used to obtain Michaelis-Menten plots and the kinetic parameters of the reactions.

By using a constant $FNR2_{mut/wt}$ concentration of 0.5 µM and NrdI concentrations ranging from 1-70 µM, a Michaelis-Menten plot was obtained as well as the kinetic parameters of the reactions. In addition to comparing the activity of the $FNR2_{mut}$ and $FNR2_{wt}$, the data obtained by Lofstad *et. al.* using the $FNR2_{wt}$ from *B. cereus* with NrdI as substrate was included for an additional comparison of the activity measurements [3]. The resulting Michaelis-Menten curves, showing results for all three enzymes, are shown in figure 3.23, with the kinetic parameters listed in table 3.5.

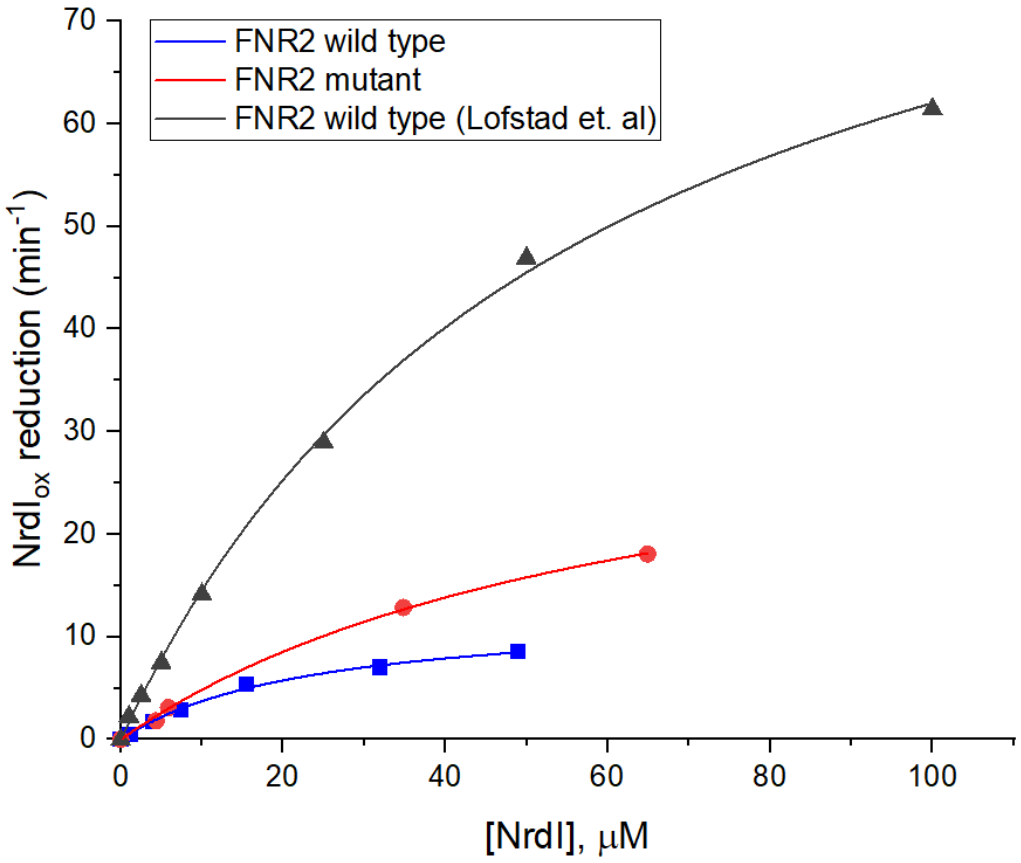

Figure 3.23. Resulting Michaelis-Menten curves from activity measurements of three different FNR2 proteins. Red curve corresponds to the $FNR2_{mut}$, blue curve corresponds to the $FNR2_{wt}$ used in this project, while the grey curve shows the results obtained by Lofstad et. al using the $FNR2_{wt}$ protein.

Table 3.5. Resulting kinetic parameters from the activity measurements using NrdI as substrate, measured for both the FNR2 H326V mutant and FNR2 wild type. Parameters obtained by Lofstad et. al using FNR2 wild type also included for comparison [3].

	k_{cat} (min^{-1})	K_M (µM)	k_{cat}/K_M (µM^{-1} min^{-1})
$FNR2_{mut}$	36 ± 3	64 ± 9	0.6 ± 0.1
$FNR2_{wt}$	12 ± 0.7	24 ± 3	0.5 ± 0.1
$FNR2_{wt}$ (Lofstad *et. al.*)	100 ± 4	61 ± 5	1.6 ± 0.2

From the results obtained in the activity measurement using the $FNR2_{mut}$, it is clear that the mutant is able to reduce NrdI in the presence of NADPH, and the data gives a satisfactory curve. Due to the high K_M value obtained for the mutant, using even higher substrate concentrations in the activity measurements would be beneficial to obtain a better curve fitting to the Michaelis-Menten model.

After the first activity measurement, using the $FNR2_{mut}$ and the $FNR2_{wt}$ enzymes with NrdI as substrate, the resulting efficiency of the $FNR2_{wt}$ was lower than expected based on previously

obtained values. Therefore, activity measurement data and kinetic parameters obtained by Lofstad *et. al*. with NrdI as substrate was included for comparison with both the mutant and the wild type used in this project [3]. The kinetic parameters from this study is also included in table 3.5 and show a big difference in the efficiency of the two wild type FNR2 enzymes. The k_{cat} obtained in this project show a 87.4% reduction from the previously obtained value, with the overall efficiency (k_{cat}/K_M) being 1/3 of the efficiency measured by Lofstad *et. al*. This difference may be due to the $FNR2_{wt}$ used in this project being stored at -80˚C for several years, and it is possible that the activity of the protein has declined considerably. Therefore, it was concluded that the data obtained using the $FNR2_{wt}$ is insufficient for comparison with the $FNR2_{mut}$ activity.

By comparing the kinetic parameters obtained using the $FNR2_{mut}$ with the parameters obtained by Lofstad et. al, there is a clear decrease in the efficiency of the mutant. With a higher k_{cat}, the results indicate that the wild type protein is able to convert more substrate per time unit than the $FNR2_{mut}$. The overall efficiency of the $FNR2_{mut}$ is 34.4% of the previously found $FNR2_{wt}$ efficiency, indicating that the His326Val mutation has had an effect on the activity of the protein, making it less efficient in the reduction of NrdI.

In the second activity measurement using Fld1 as substrate, the $FNR2_{wt}$ was not tested as for the first measurement with NrdI, due to the $FNR2_{wt}$ available showing reduced activity after the first experiment and is not suitable for comparison to the mutant activity. As for the first experiment, the data and kinetic parameters obtained by a previous study was included and used in comparing the $FNR2_{mut}$ activity with the $FNR2_{wt}$ [16], with Fld1 as substrate and substrate concentration ranging from 1-30 µM. The resulting Michaelis-Menten plots showing both the $FNR2_{mut}$ results and the $FNR2_{wt}$ results obtained by Gudim *et. al*. is shown in figure 3.24.

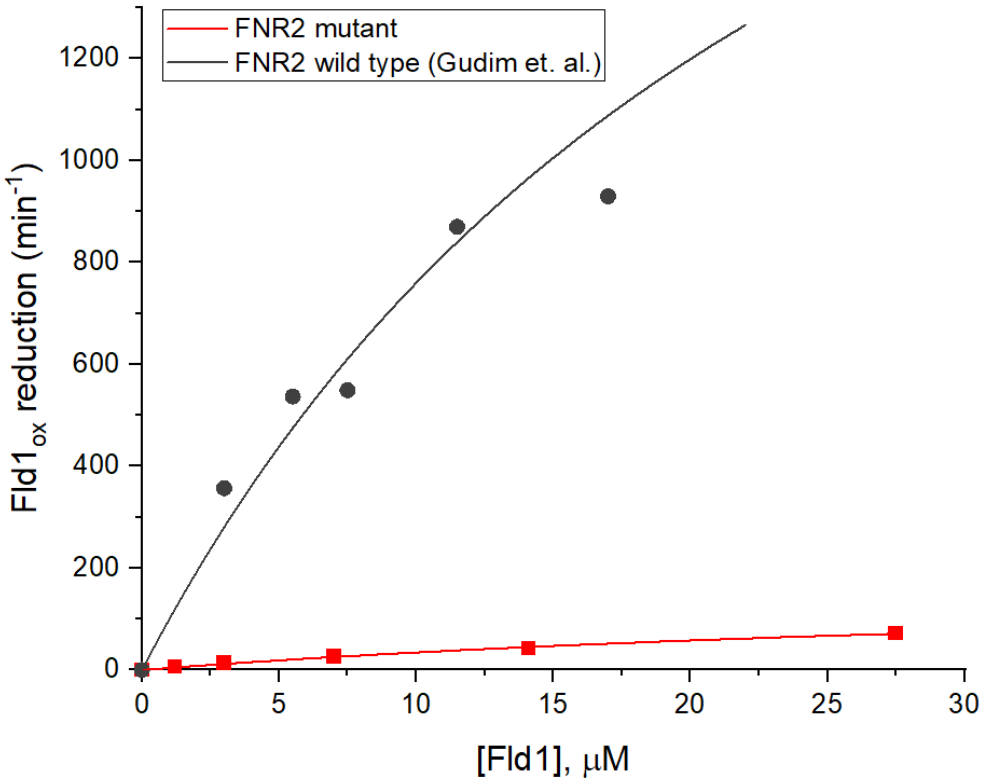

Figure 3.24. Resulting Michaelis-Menten plot showing the results from activity measurements with Fld1 as substrate. Red curve showing the results using the $FNR2_{mut}$, and grey curve showing results using the $FNR2_{wt}$ [16].

A figure of the resulting Michaelis-Menten fit of only the $FNR2_{mut}$ with Fld1 as substrate is shown in Appendix 7, indicating a satisfactory curve fit not clearly shown in figure 3.24. The curves obtained using the two different FNR2 enzymes indicate a clear difference in the activity of the $FNR2_{mut}$ and the $FNR2_{wt}$ with Fld1 as substrate. The kinetic parameters obtained using the mutant, as well as the parameters obtained by Gudim *et. al.*, is listed in table 3.6.

Table 3.6. Resulting kinetic parameters from the activity measurements using the $FNR2_{mut}$ with Fld1 as substrate. Parameters obtained by Gudim et. al using $FNR2_{wt}$ also included for comparison [16].

	k_{cat} (min^{-1})	K_M (µM)	k_{cat}/K_M (μM^{-1} min^{-1})
$FNR2_{mut}$	183 ± 31	43 ± 11	4 ± 2
$FNR2_{wt}$ (Gudim *et. al.*)	2778 ± 401	25 ± 7	111 ± 47

The values in table 3.6 indicate that the efficiency of the $FNR2_{mut}$ is considerably reduced compared the efficiency of the $FNR2_{wt}$ when using Fld1 a substrate, with the efficiency (k_{cat}/K_M) of the mutant being 3.8% of the wild type value. The k_{cat} value shows that the wild type is able to reduce considerably more substrate per time unit than the mutant, while the K_M value is approximately the same. As for the activity measurements obtained using NrdI as substrate, the

His326Val mutation appears to have a considerable effect on the proteins` ability to reduce the substrates. An overview over the activity measurement results using NrdI and Fld1 as substrates in reactions with the $FNR2_{mut}$ and the $FNR2_{wt}$ is shown in table 3.7.

Table 3.7. Overview over the kinetic parameters obtained by using NrdI and Fld1 as substrates in reactions with the $FNR2_{mut}$ and the $FNR2_{wt}$. The $FNR2_{wt}$ parameters included is found by Lofstad *et. al*. (NrdI) and Gudim *et. al*. (Fld1) [3, 16].

	$FNR2_{mut}$			**$FNR2_{wt}$ (Lofstad *et. al* / Gudim *et. al*)**		
	k_{cat} (min^{-1})	K_M (μM)	k_{cat}/K_M (μM^{-1} min^{-1})	k_{cat} (min^{-1})	K_M (μM)	k_{cat}/K_M (μM^{-1} min^{-1})
NrdI	36 ± 3	64 ± 9	0.6 ± 0.1	100 ± 4	61 ± 5	1.6 ± 0.2
Fld1	183 ± 31	43 ± 11	4 ± 2	2778 ± 401	25 ± 7	111 ± 47

As also indicated by previous studies of the FNR2 activity, where the $FNR2_{wt}$ was concluded to be more efficient with Fld1 as substrate than with NrdI, the $FNR2_{mut}$ also show considerably higher efficiency with Fld1 compared to NrdI as substrate. Thus, it is observed that the $FNR2_{mut}$ mostly follow the trend in activity as found in previous studies, but the overall activity of the mutated protein is considerably reduced, especially for the most effective pair (FNR2/Fld1). To verify this observation further, the mutant activity could be tested with Fld2 from *B. cereus* as substrate, which is the substrate found to be most efficiently reduced by the $FNR2_{wt}$ [16].

The main aim of this project was to investigate if the difference in the FNR1 and FNR2 efficiency was due to the different FAD-stacking residues in the two enzymes. It was therefore of interest to mutate the FAD-stacking histidine in FNR2 to valine, which is the corresponding FAD-stacking residue in FNR1. By performing this mutation and doing activity measurements on the resulting mutated FNR2, the activity of the $FNR2_{mut}$ can be compared to the wild type $FNR1_{wt}$ activity. If the mutation in the protein resulted in a reduction in FNR2 activity to the corresponding FNR1 activity, this could be a strong indication that the different FAD-stacking residues has implications on the enzyme activity and might be the reason for the difference in substrate reduction efficiency displayed by FNR1 and FNR2 from *B. cereus.*

The activity measurement results obtained for the $FNR2_{mut}$, with both NrdI and Fld1 as substrates, compared to previous results obtained for the $FNR1_{wt}$ with the same substrates is shown in figure 3.25. The $FNR1_{wt}$ activity data used in this thesis is from previous studies performed by Lofstad *et. al*. and Gudim *et. al*. [3, 16].

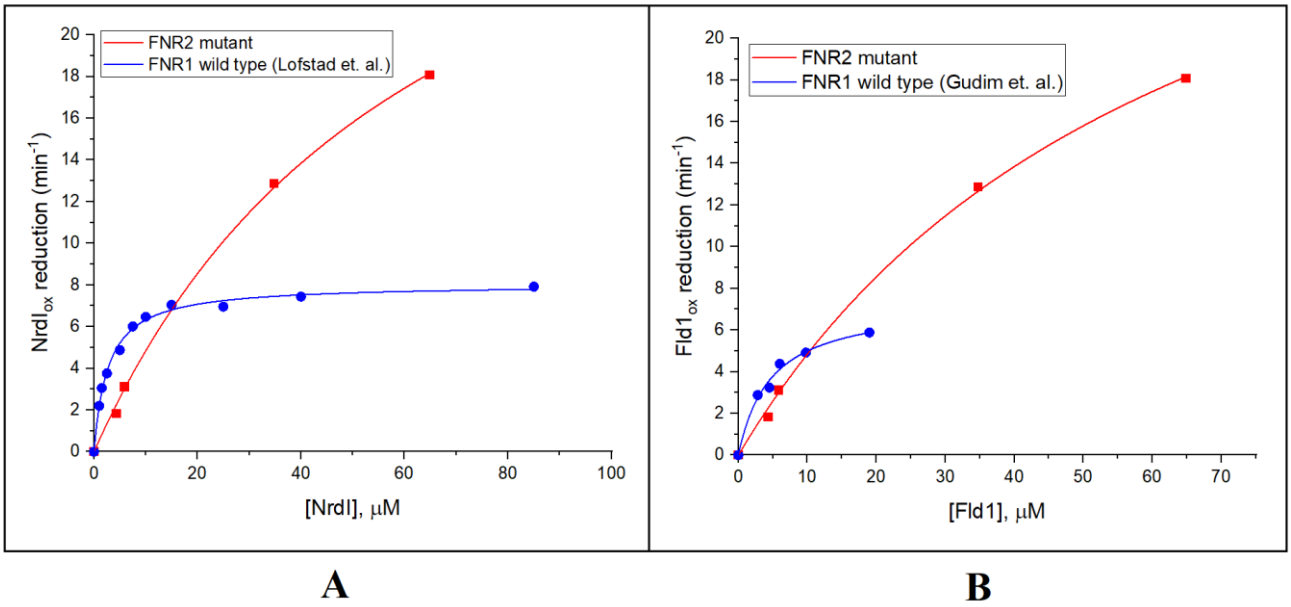

Figure 3.25. Michaelis-Menten plots showing the activity measurement results for the $FNR2_{mut}$ compared to the $FNR1_{wt}$. A) $FNR2_{mut}$ activity results with NrdI as substrate compared to the $FNR1_{wt}$ activity results obtained by Lofstad *et. al.* [3]. B) $FNR2_{mut}$ activity results with Fld1 as substrate compared to the $FNR1_{wt}$ activity results obtained by Gudim *et. al*. [16]. Red curves correspond to the data obtained with the $FNR2_{mut}$ and blue curves corresponds to the data obtained with the $FNR1_{wt.}$

An overview over the kinetic parameters obtained for the $FNR2_{mut}$ with both substrates, compared to the corresponding parameters previously obtained for the $FNR1_{wt}$ is listed in table 3.8.

Table 3.8. Overview over the kinetic parameters obtained by using NrdI and Fld1 as substrates in reactions with the $FNR2_{mut}$ and the $FNR1_{wt}$. The $FNR1_{wt}$ parameters included is found by Lofstad *et. al.* (NrdI) and Gudim *et. al*. (Fld1) [3, 16].

	$FNR2_{mut}$			**$FNR1_{wt}$**		
	k_{cat} (min^{-1})	K_M (µM)	k_{cat}/K_M (µM^{-1} min^{-1})	k_{cat} (min^{-1})	K_M (µM)	k_{cat}/K_M (µM^{-1} min^{-1})
NrdI	36 ± 3	64 ± 9	0.6 ± 0.1	8 ± 0.1	2.7 ± 0.2	3 ± 0.2
Fld1	183 ± 31	43 ± 11	4 ± 2	7.3 ± 0.5	4.7 ± 0.8	1.5 ± 0.3

The kinetic parameters shown in table 3.8 indicate that there are differences in the activity and substrate reduction efficiency for the $FNR2_{mut}$ and the $FNR1_{wt}$ enzymes. For both substrates, the k_{cat} is higher for the $FNR2_{mut}$, indicating that despite the mutation, the FNR2 protein is still able to reduce more substrate per time unit than the $FNR1_{wt}$ enzyme. However, when looking at the K_M values, it is clear that the $FNR2_{mut}$ requires higher substrate concentrations to work with high efficiency than the $FNR1_{wt}$. The resulting overall efficiency for the two enzymes is different for the two substrates. The k_{cat}/K_M value for the $FNR2_{mut}$ is slightly higher than the $FNR1_{wt}$ value when Fld1 is used as substrate, but lower than the $FNR1_{wt}$ value with NrdI as substrate. In other words, the $FNR2_{mut}$ is the most efficient Fld1 reductase, while the $FNR1_{wt}$ is the most efficient NrdI reductase when comparing the two enzymes. These results indicate the same trend as the results obtained by Lofstad *et. al*. and Gudim et. al when investigating the wild type FNR1 and FNR2 enzymes with NrdI and Fld1 as substrates [3, 16]. However, in these previous studies, the overall efficiency (k_{cat}/K_M) of the $FNR2_{wt}$ in NrdI reduction was ~53% of the $FNR1_{wt}$ efficiency, while using the $FNR2_{mut}$, the NrdI reduction efficiency is reduced to ~18% of the $FNR1_{wt}$ efficiency. Conversely, by using Fld1 as substrate, the overall efficiency (k_{cat}/K_M) of the $FNR1_{wt}$ enzyme is 1.35% of the $FNR2_{wt}$ efficiency and 35.4% of the $FNR2_{mut}$ efficiency. It may therefore be concluded that the His326Val mutation has resulted in a decreased efficiency of the FNR2 enzyme, but the activity is not reduced in the extent that would be required to reach the corresponding $FNR1_{wt}$ activity.

By calculating the percentage difference between the mutant and the two wild type enzymes, it is observed that the $FNR2_{mut}$ is still closer to the $FNR2_{wt}$ activity level than the $FNR1_{wt}$ (table 3.9). Thus, since the $FNR2_{mut}$ does not show the corresponding activity observed for the $FNR1_{wt}$, the difference in the FAD-stacking residue cannot be the only factor contributing to the difference in the activities of FNR1 and FNR2. Although the mutation has led to a reduced FNR2 activity, other structural features most likely play an important role when discussing the difference in FNR1 and FNR2 catalysis.

Table 3.9. Percentage difference in the kinetic parameters comparing the $FNR2_{mut}$ to the wild type FNR1 and FNR2 proteins in *B. cereus*.

	Parameter	$FNR2_{mut}$ vs. $FNR1_{wt}$	$FNR2_{mut}$ vs. $FNR2_{wt}$
NrdI	k_{cat}	+353,8 %	-63.7 %
	K_M	+2303 %	+6.39 %
	k_{cat}/ K_M	-81.7 %	-65.6 %
Fld1	k_{cat}	+2414 %	-93.4 %
	K_M	+820 %	+73.0 %
	k_{cat}/ K_M	+183 %	-96.2 %

In addition to using UV-vis spectroscopy in activity measurements, a full UV-vis spectrum was recorded for both the $FNR2_{wt}$ and $FNR2_{mut}$ for comparison. The spectrum is shown in figure 3.26.

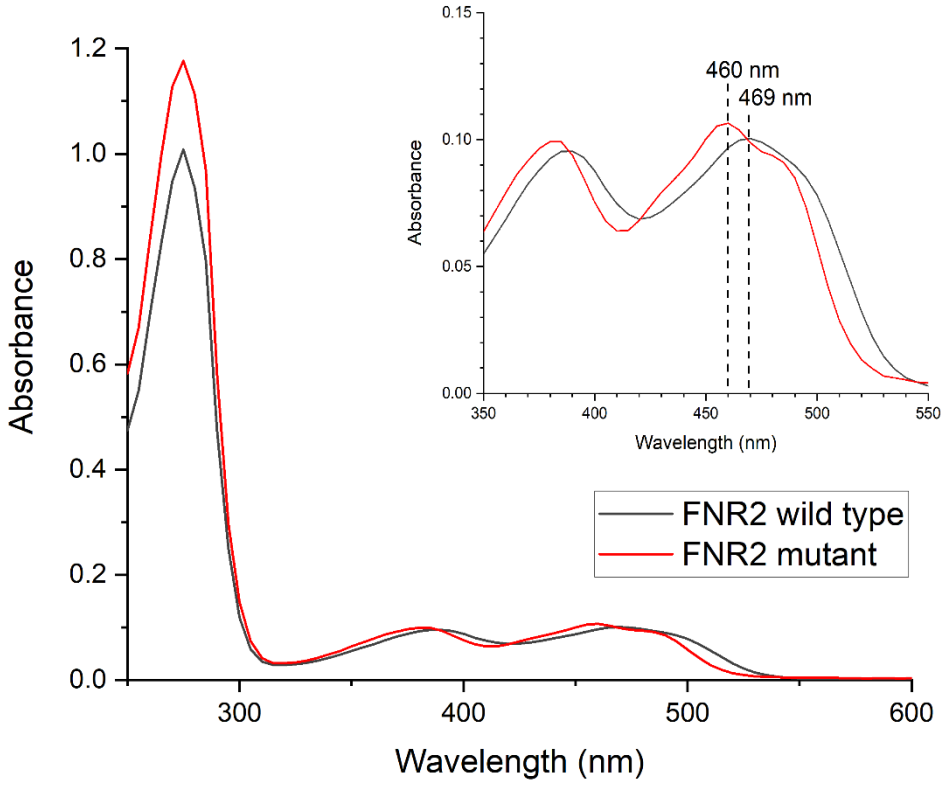

Figure 3.26. UV-vis spectrum showing the absorption at different wavelengths. The grey line corresponds to the $FNR2_{wt}$, while the red line shows the $FNR2_{mut}$ absorption.

From analyzing the structures (section 3.3.2) it became clear that the $FNR2_{mut}$ structure had one monomer with FAD cofactor bound, while the other monomer did not have the FAD cofactor. When measuring the concentration of the $FNR2_{mut}$ before crystallization and activity

measurements, the absorption at λ_{max}= 460 nm was noted and used in calculating the concentration using Beer-Lambert law. This corresponds to the absorption by the FAD cofactor. With the knowledge that approximately half of the cofactors may be missing from the mutant sample, these concentration measurements corresponds to the concentration of active enzyme in the purified sample. By looking at figure 3.26, where the 450-460 nm absorption by the wild type and mutant proteins is approximately aligned, it is observed that the 280 nm absorption is higher for the $FNR2_{mut}$ than the $FNR2_{wt}$, indicating that the protein concentration is higher for the mutant sample.

Another interesting observation is that the λ_{max} for the $FNR2_{mut}$ corresponding to the FAD cofactor is shifted to the left in the UV-vis spectrum in figure 3.26. The previously determined λ_{max} for the $FNR2_{wt}$ is 469 nm, while the λ_{max} for the $FNR1_{wt}$ has been found to be 462 nm [3]. Thus, the λ_{max} for the $FNR2_{mut}$, being reduced to 460 nm, is now closer to the $FNR1_{wt}$ value than the $FNR2_{wt}$ value. This confirms that the electronic environment of the FAD cofactor in the FNR2 enzyme has, in fact, been changed as a consequence of the His326Val mutation.

4. Conclusion

By performing activity measurements, as well as solving the structure of the His326Val mutated FNR2 protein, several interesting findings considering the structure and function of the $FNR2_{mut}$ allows for some conclusions of the project. The $FNR2_{mut}$ display a unique domain rotation not seen in *B. cereus* FNRs before and allows for the conclusion that the mutation has had structural effects with implications on the enzymes` efficiency in substrate reduction. The results also show that the mutation have led to the loss of the FAD cofactor in half of the protein monomers, where the monomers having lost the cofactor also display a different orientation of the NADPH-binding domain. As the activity measurements has been based on the active protein monomers, having bound the FAD cofactor, there may also be a possibility that the reduced efficiency displayed by the $FNR2_{mut}$ could partly be a consequence of the additional time the substrate may use to encounter the active protein monomers for reduction. The extent of this effect on the protein efficiency could be investigated by performing binding studies using both the apo- and holoprotein, and thereby obtain information about the possible substrate binding to the inactive protein monomers lacking the FAD cofactor.

The reason for the loss of the FAD cofactor in half of the protein monomers cannot be concluded as this time, but one possible explanation could be that the apparent reduced stability of the $FNR2_{mut}$ may have affected the binding of the FAD cofactor. Another interesting point is that the mutated protein may display some sort of negative cooperativity in the binding of the cofactor, leading to reduced affinity for the FAD cofactor in one of the monomers constituting the FNR2 dimer. This cooperative binding of the FAD cofactor in the *B. cereus* FNRs has not been addressed in previous studies, but there is a possibility that there exists some degree of negative cooperativity in FAD binding by the FNRs that could be enhanced the mutation, leading to the loss of one FAD cofactor in the $FNR2_{mut}$ dimer.

From the activity measurements using the mutated FNR2 protein, it is clear that the efficiency of the $FNR2_{mut}$ is considerably reduced compared to the $FNR2_{wt}$. However, the mutation has not affected the FNR2 activity and efficiency in the degree that would be required to match the $FNR1_{wt}$ activity. Thus, the reason for the difference in substrate reduction efficiency by the wild type FNR1 and FNR2 from *B. cereus* cannot be concluded to be the difference in the FAD-stacking residues alone. Although the mutation of this residue has had a considerable effect on the FNR2 activity, some other structural factors may also be of importance when discussing the difference in the enzyme catalysis observed for these two enzymes. One obvious suggestion for

further studies of the FNR1 and FNR2 activity, is to investigate the effect of the longer C-terminal helix in the FNR1 structure, which is not present in the structure of FNR2.

5. Appendices

5.1 Appendix 1: Abbreviations

B. cereus, Bacillus cereus

E. coli, Escherichia coli

RNR, Ribonucleotide Reductase

DNA, deoxyribonucleic acid

$NADP^+$, nicotinamide adenine dinucleotide phosphate, oxidized

NADPH, nicotinamide adenine dinucleotide phosphate, reduced

S•, cysteinyl radical

Y•, tyrosyl radical

FAD, flavin adenine dinucleotide cofactor

FMN, flavin mononucleotide cofactor

FNR, ferredoxin/flavodoxin $NADP^+$ oxidoreductase

$FNR2_{mut}$, FNR2 mutant

$FNR2_{wt}$, FNR2 wild type

$FNR1_{wt}$, FNR1 wild type

Fld, flavodoxin

Fd, ferredoxin

TrxR, thioredoxin reductase

Trx, thioredoxin

Redox, reduction-oxidation

Sq, semiquinone

Hq, hydroquinone

Ox, oxidized

IEX, Ion-exchange chromatography

SEC, Size exclusion chromatography

GF, Gel filtration

UV-vis spectroscopy, Ultraviolet visible spectroscopy

SDS, Sodium dodecyl sulfate

SDS-PAGE, Sodium dodecyl sulfate polyacrylamide electrophoresis

LB medium, Lysogeny Broth medium

TB medium, Terrific Broth medium

EDTA, Ethylenediaminetetraacetate

DTT, Dithiothreitol

TCEP, Tris(2-carboxyethyl)Phosphine Hydrochloride

Table 5.1.1. Amino acids

Amino Acid	Three-Letter Abbreviation	One-Letter Abbreviation
Alanine	Ala	A
Arginine	Arg	R
Asparagine	Asn	N
Aspartate	Asp	D
Cysteine	Cys	C
Glutamate	Glu	E
Glutamine	Gln	Q
Glycine	Gly	G
Histidine	His	H
Isoleucine	Ile	I
Leucine	Leu	L
Lysine	Lys	K
Methionine	Met	M
Phenylalanine	Phe	F
Proline	Pro	P

Serine	Ser	S
Threonine	Thr	T
Tryptophan	Trp	W
Tyrosine	Tyr	Y

5.2 Appendix 2: DNA constructs

Gene name: BC4926
Vector name: pET-22b(+)
Cloning sites: NdeI/HindIII
Additional 5' sequence: CAT
Additional 3' sequence: AAGCTT

B. cereus FNR2 (BC4926) sequence:

```
ATGAAAGTGGCAGAAAATCAAAAAGTTTACGACATAACAATTATT
GGTGGTGGTCCAACAGGGCTGTTCACAGCATTTTATGGCGGTATG
AGACAAGCAAGTGTAAAAATCATTGAAAGCTTACCTCAACTTGGA
GGACAATTATCCGCACTCTACCCTGAAAAATACATTTATGATGTA
GCTGGATTCCCAAAAGTGCGCGCACAAGAATTAGTTGATAACTTA
AAAGAGCAAATGAAGAAATTTGACCCAACCGTTTGTTTAGAAGAA
GCTGTCGATACGCTTGAGAAACAAGCTGACGGTATATTTAAACTT
GTTACGAATAAGCAAACTCACTATTCTAAATCAGTTATTATTACT
GCTGGCAATGGTGCTTTCCAACCACGCCGCTTAGAATTAGAAGGT
ACAGCAAAGTATGAAAAGAAAAACTTACATTATTTCGTTGATGAT
ATGAATAAATTTGCCGGTAAGCGCGTCGTAGTATTTGGCGGCGGC
GATTCAGCTGTTGATTGGACAATGATGTTAGAACCGATCGCTGAA
AAAGTTACAATCGTTCATCGCCGCGATAAATTCCGTGCGCATGAA
CATAGCGTCGAAAACTTAATGAATTCTCGTGCAGAAGTAAGTACA
CCGTATGTTCCAGTTGAACTCATTGGTGATGACAAAATTGAACAA
GTCGTTCTTCAGCACGTAAAAACGGAAGAAAAAGTTATCATCGAT
GTTGATGACGTAATTGTAAACTATGGCTTCGTTTCTTCTCTTGGC
CCAATTAAAAACTGGGGCTTAGATATACAAAAAAACAGCATCCTT
GTAAATTCAAAAATGGAAACAAATATTCCTGGCATTTACGCTGCT
GGTGACATTTGTACATATGAAGGAAAAGTAAAACTCATTGCTTGC
GGCTTCGGTGAAGCACCAACAGCAGTAAACAATGCAAAAGCTTAC
TTCGATCCAAATGCAAAACTTCAACCAATGCATAGCTCAAGCATG
TTT
```

B. cereus FNR2 (BC4926) codon optimized sequence:

```
CATATGAAGGTTGCGGAGAACCAGAAAGTGTACGACATCACCATC
ATTGGTGGCGGTCCGACCGGTCTGTTCACCGCGTTTTATGGCGGT
ATGCGTCAAGCGAGCGTTAAAATCATTGAGAGCCTGCCGCAGCTG
GGCGGTCAACTGAGCGCGCTGTACCCGGAAAAATACATTTATGAT
GTTGCGGGTTTCCCGAAAGTGCGTGCGCAGGAGCTGGTTGACAAC
CTGAAGGAACAAATGAAGAAATTTGATCCGACCGTGTGCCTGGAG
GAAGCGGTTGACACCCTGGAGAAACAGGCGGATGGTATCTTCAAG
CTGGTGACCAACAAACAAACCCACTATAGCAAGAGCGTTATCATT
ACCGCGGGTAACGGTGCGTTTCAGCCGCGTCGTCTGGAGCTGGAA
```

GGTACCGCGAAATACGAAAAGAAAAACCTGCACTATTTCGTTGAC
GATATGAACAAGTTTGCGGGTAAACGTGTGGTTGTGTTCGGCGGT
GGCGACAGCGCGGTGGATTGGACCATGATGCTGGAGCCGATCGCG
GAAAAAGTTACCATTGTGCACCGTCGTGACAAGTTTCGTGCGCAC
GAGCACAGCGTGGAAAACCTGATGAACAGCCGTGCGGAAGTGAGC
ACCCCGTACGTTCCGGTGGAGCTGATCGGCGACGATAAGATTGAA
CAGGTTGTGCTGCAACACGTGAAGACCGAGGAAAAAGTTATCATT
GACGTGGACGATGTTATCGTGAACTATGGTTTCGTTAGCAGCCTG
GGCCCGATTAAGAACTGGGGTCTGGATATCCAGAAAAACAGCATT
CTGGTGAACAGCAAGATGGAAACCAACATCCCGGGTATTTACGCG
GCGGGCGACATCTGCACCTATGAGGGCAAGGTGAAACTGATTGCG
TGCGGTTTCGGTGAAGCGCCGACCGCGGTTAACAACGCGAAAGCG
TACTTTGATCCGAACGCGAAGCTGCAACCGATGGTGAGCAGCAGC
ATGTTTTAA**AAGCTT**

FNR2 protein sequence ($FNR2_{wt}$):

MKVAENQKVYDITIIGGGPTGLFTAFYGGMRQASVKIIESLPQLGGQLSALYPEKYIYDVAGFPKVRAQELVDNLKE
QMKKFDPTVCLEEAVDTLEKQADGIFKLVTNKQTHYSKSVIITAGNGAFQPRRLELEGTAKYEKKNLHYFVDDMNKF
AGKRVVVFGGGDSAVDWTMMLEPIAEKVTIVHRRDKFRAHEHSVENLMNSRAEVSTPYVPVELIGDDKIEQVVLQ
HVKTEEKVIIDVDDVIVNYGFVSSLGPIKNWGLDIQKNSILVNSKMETNIPGIYAAGDICTYEGKVKLIACGFGEAPTA
VNNAKAYFDPNAKLQPM**H**SSSMF-

Mutated FNR2 protein sequence (His326Val):

MKVAENQKVYDITIIGGGPTGLFTAFYGGMRQASVKIIESLPQLGGQLSALYPEKYIYDVAGFPKVRAQELVDNLKE
QMKKFDPTVCLEEAVDTLEKQADGIFKLVTNKQTHYSKSVIITAGNGAFQPRRLELEGTAKYEKKNLHYFVDDMNKF
AGKRVVVFGGGDSAVDWTMMLEPIAEKVTIVHRRDKFRAHEHSVENLMNSRAEVSTPYVPVELIGDDKIEQVVLQ
HVKTEEKVIIDVDDVIVNYGFVSSLGPIKNWGLDIQKNSILVNSKMETNIPGIYAAGDICTYEGKVKLIACGFGEAPTA
VNNAKAYFDPNAKLQPM**V**SSSMF

5.3 Appendix 3: Buffers and media

Table A3.1: Transformation, bacterial growth, and protein expression

LB-medium:

4 g NaCl

4 g peptone

2 g yeast extract

8 g Agar (for Agar plates)

mqH_2O to final volume 400 ml

Sterilized

TB-medium:

150,6 g TB-mix

mqH_2O to 4,0 L

4.2 ml glycerol (100%)/L

Sterilized

Ampicillin (stock, 100 mg/ml):

1.5 g ampicillin

15 ml mqH_2O

IPTG (stock, 0,8M):

3.30 g IPTG (238.3 g/mol)

17 ml mqH_2O

Table A3.2: Protein purification

Buffer A (IEX):

50 mM Tris-HCl

2 mM DTT

Adjusted to pH 8.0 with 12 M HCl

Degassed

Buffer B (IEX):

50 mM Tris-HCl

1 M KCl

2 mM DTT

Adjusted to pH 8.0 with 10 M HCl

Degassed

Buffer C (GF):

50 mM HEPES

100 mM KCl

2 mM DTT

Adjusted to pH 8.0 with 10 M KOH

Degassed

Buffer D (IEX):

50 mM Tris-HCl

2 mM TCEP

Adjusted to pH 7.5 with 12 M HCl

Degassed

Buffer E (IEX):

50 mM Tris-HCl

1 M KCl

2 mM TCEP

Adjusted to pH 7.5 with 12 M HCl

Degassed

Buffer F (GF):

50 mM HEPES

100 mM KCl

2 mM TCEP

Adjusted to pH 7.5 with 10 M KOH

Degassed

Buffer G (IEX):

50 mM HEPES

2 mM DTT

Adjusted to pH 7.5 with 10 M KOH

Degassed

Buffer H (IEX):

50 mM HEPES

1M KCl

2 mM DTT

Adjusted to pH 7.5 with 10 M KOH

Degassed

Buffer I (GF):

50 mM HEPES

100 mM KCl

2 mM DTT

Adjusted to pH 7.5 with 10 M KOH

Degassed

Table A3.3: Bacterial lysis

Buffer J:

100 mM Tris-HCl

2 mM DTT

1 mM EDTA

Protease inhibitor

DNase I

Adjusted to pH 8.0 with 12 M HCl

Table A3.4: NativePAGE

Anode buffer:

50 ml Running Buffer (20X)

950 ml mqH_2O

Cathode buffer:

20 ml Running Buffer (20X)

20 ml Cathode Additive (20X)

360 ml mgH_2O

Fix solution:

40% Methanol

10% Acetic Acid

mqH_2O to 100 ml total volume

Destain solution:

8% Acetic Acid

mgH_2O to 100 ml total volume

Table A3.5: Activity measurements

Buffer K:

50 mM HEPES

50 mM KCl

pH 7.5

Degassed with Argon (99.99%)

5.4 Appendix 4: Crystallization conditions

Table A4.1: Morpheus additive mixes

Mix name	Composition
Halogens	0.3 M Sodium fluoride; 0.3 M Sodium bromide; 0.3 M Sodium iodide
Alcohols	0.2 M 1,6-Hexanediol; 0.2 M 1-Butanol 0.2 M 1,2-Propanediol; 0.2 M 2-Propanol; 0.2 M 1,4-Butanediol; 0.2 M 1,3-Propanediol
Ethylene glycols	0.3 M Diethylene glycol; 0.3 M Triethylene glycol; 0.3 M Tetraethylene glycol; 0.3 M Pentaethylene glycol
Monosaccharides	0.2 M D-Glucose; 0.2 M D-Mannose; 0.2 M D-Galactose; 0.2 M L-Fucose; 0.2 M D-Xylose; 0.2 M N-Acetyl-D-Glucosamine
Amino acids	0.2 M DL-Glutamic acid monohydrate; 0.2 M DL-Alanine; 0.2 M Glycine; 0.2 M DL-Lysine monohydrochloride; 0.2 M DL-Serine

Table A4.2: Morpheus buffer systems

Mix name	Concentration	pH	Composition
Buffer system 1	1.0 M	6.5	Imidazole; MES monohydrate (acid)
Buffer system 2	1.0 M	7.5	Sodium HEPES; MOPS (acid)
Buffer system 3	1.0 M	8.5	Tris (base); BICINE

Table A4.3: Morpheus precipitant mixes

Mix name	Composition
60% Precipitant Mix 1	40% v/v PEG 500 MME; 20% w/v PEG 20000
60% Precipitant Mix 2	40% v/v Ethylene glycol; 20% w/v PEG 8000
60% Precipitant Mix 3	40% v/v Glycerol; 20% w/v PEG 4000
75% Precipitant Mix 4	25% v/v MPD; 25% PEG 1000; 25% w/v PEG 3350

5.5 Appendix 5: Materials

Table A5.1. Materials and equipment.

Material/Equipment	**Manufacturer**
Amicon Ultra Centrifugal Filters (10 K and 30 K)	Merck
Äkta Fraction Collector Frac-950 Tube Rack	GE Healthcare
BD Plastipak Syringes (20 ml and 15 ml)	BD Plastipak
Cell Culture Petri Dishes	Merck
Centrifugal Tubes (50 ml and 15 ml)	VWR
Cryo loops	Hampton Research
Crystallization strips (for optimization, sitting drop)	Douglas Instruments
Cuvettes (quartz, 10 mm)	Hellma
Disposable Transfer Pipet (sterile, 1 mL)	VWR
Eppendorf Tubes (5.0 ml)	Merck
HiTrap Desalting Column	GE Healthcare
HiTrap Q HP Anion Exchange Column	GE Healthcare
Inoculating Loop (10 µl)	Merck
Rainin Pipet-Lite XLS (0.5-1000 µl)	Mettler Toledo
Sterile 0.45 µm filter	Sarstedt
Superose 12 10/300 column GL column	GE Healthcare
Swissci 96-well 3-drop crystallization plates	Molecular Dimensions
Teflon Discs (0.3-3.5 ml and 3.0-5.0 ml)	Thermo Scientific

Table A5.2. Chemicals.

Chemical	**Manufacturer**
Agar, Bacteriological	VWR
Ammonium Sulphate	Merck
Ampicillin	Sigma
Argon (gas)	Praxair
DNaseI	Merck
DTT	VWR
EDTA	Sigma
Ethanol	Arcus
Glycerol (99.5%)	VWR
HEPES	ITW Reagents

InstantBlue Coomassie Protein Stain	Expedeon
IPTG	VWR
Bolt LDS Sample Buffer (4x)	Invitrogen
Mixed gas (9 % H_2, 91 % N_2)	Praxair
Morpheus Alcohols	Molecular Dimensions
Morpheus Amino Acids	Molecular Dimensions
Morpheus Buffer System 3	Molecular Dimensions
Morpheus Ethylene Glycols	Molecular Dimensions
Morpheus Halogens	Molecular Dimensions
Morpheus Monosaccharides	Molecular Dimensions
Morpheus Precipitant mix 2 and 3	Molecular Dimensions
$NADP^+$	Sigma
NADPH	Sigma
NativePAGE Bolt 4-16% Bis-Tris, 1.0 mm Mini Protein Gel	Invitrogen
NativePAGE Cathode Buffer Additive (20x)	Invitrogen
NativeMark Unstained Protein Standard	Invitrogen
NativePAGE Running Buffer (20x)	Invitrogen
NativePAGE Sample Buffer (4x)	Invitrogen
Nitrogen (liquid)	Praxair
NuPAGE 4-12 % Bis-Tris, 1.0 mm Mini Protein Gel	Invitrogen
NuPAGE MOPS SDS Running Bugger	Invitrogen
One Shot BL21 Star (DE3) competent *E. coli* cells	Invitrogen
Peptone (from meat)	Fluka Analytical
Potassium Chloride	VWR
Protease Inhibitor Cocktail Tablets	Roche
SeeBlue Plus2 Pre-Stained Protein Standard	Invitrogen
Sodium Chloride	VWR
TCEP	Sigma
Terrific Broth EZMix (powder)	Sigma
Tris(hydroxymethyl)aminomethane	VWR
Yeast extract (granulated)	Merck

Table A5.3. Hardware.

Hardware	**Manufacturer**
8453 Diode-array UV-vis Spectrophotometer	Agilent Technologies
855-AC/EXP Controlled Atmosphere Anaerobic Glove Box	Plan-Labs
Äkta purifier System	GE Healthcare
AT250 (analytical balance scale)	Mettler Toledo
Avanti J-20 XP Centrifuge	Beckman Coulter
Bolt Mini Gel Tank	Invitrogen
Cary 60 UV-vis Spectrophotometer	Agilent Technologies
Eppendorf Centrifuge 5415 R	Merck
EPS 600 Electrophoresis Power Supply	Pharmacia Biotech
JA-10 rotor	Beckman Coulter
JA-25.50 rotor	Beckman Coulter
Milli-Q plus (water purification system)	Merck
MeterLab PHM240 (pH/ion meter)	Radiometer Analytical
Mosquito Crystallization Robot	SPT Labtech
MS1 Minishaker (Vortex)	Heigar
VC-750 Vibra-Cell Ultrasonic Processor	Sonics & Materials
Xcell SureLock Mini-Cell Chamber	Life Technologies

Table A5.4. Crystallization screens.

Crystallization Screen	**Manufacturer**
Index	Hampton Research
JCSG+	Molecular Dimensions
Morpheus	Molecular Dimensions
PGA	Molecular Dimensions

5.6 Appendix 6: FNR1-$NADP^+$ co-crystallization and structure solving procedure

The FNR1 wild type protein (already expressed and purified) was crystallized (Mosquito crystallization robot, SPT Labtech) with three different concentrations of $NADP^+$, by using the crystallization screens Morpheus (Molecular Dimensions), $JCSG^+$ (Molecular Dimensions) and SaltRx (Hampton Research) and the sitting drop method as described in section 2.6.1.1. For each of the crystal screens, three crystallization drops (250 nl + 250 nl) was set up with FNR1: $NADP^+$ concentration ratios 1:5, 1:10 and 1:15. After 1-2 weeks, cubic crystals were observed in the SaltRx condition F12, and the resulting crystals were soaked in cryo-solution, to increase the lifetime of the crystals, and frozen in liquid nitrogen before X-ray data collection.

The obtained diffraction data was indexed and integrated by auto-processing at the synchrotron as described for the FNR2 mutant. The data was further processed using the CCP4 software, with scaling and merging in Aimless to obtain the correct space group and quality parameters. Molecular replacement was used to solve the structure with the wild type FNR1 from *B. cereus* as starting model (Phaser). The FNR1 structure co-crystallized with $NADP^+$ was modelled into the electron density in Coot with cycles of refinement using REFMAC5, while monitoring the *R*-factor and R_{free} values. Validation of the resulting structure was performed by investigating the Ramachandran plot and geometry validation in Coot. The modelling process included adjustments of side chain rotamers and adjustment to the electron density. The resulting protein structure was visualised using PyMol (Schrödinger, LCC).

5.7 Appendix 7: Michaelis-Menten plot of $FNR2_{mut}$ with Fld1

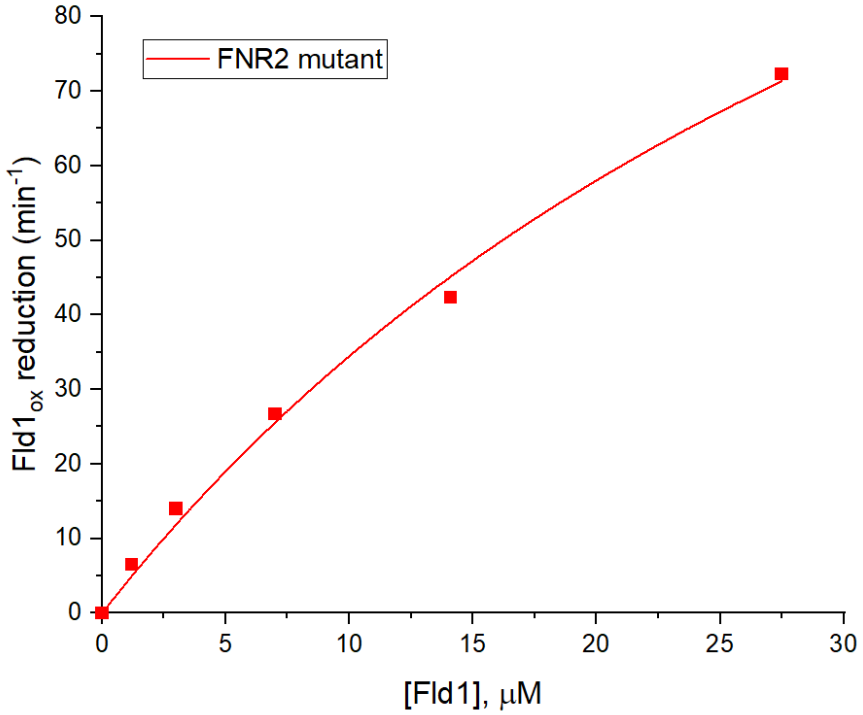

Figure 4.1. Resulting Michaelis-Menten plot showing the results from activity measurements of the $FNR2_{mut}$ with Fld1 as substrate. Results indicate good fit to the Michaelis-Menten model.

6 Reference list

1. Hammerstad, M., Hersleth, H.-P., Tomter, A.B., Røhr, Å.K., and Andersson, K.K., *Crystal Structure of Bacillus cereus Class Ib Ribonucleotide Reductase Di-iron NrdF in Complex with NrdI.* ACS Chem. Biol., 2014. **9**(2): p. 526-537.
2. Torrents, E., *Ribonucleotide reductases: essential enzymes for bacterial life.* Front. Cell Infect. Microbiol., 2014. **4**(1): p. 52.
3. Lofstad, M., Gudim, I., Hammerstad, M., Røhr, Å.K., and Hersleth, H.-P., *Activation of the Class Ib Ribonucleotide Reductase by a Flavodoxin Reductase in Bacillus cereus.* Biochemistry, 2016. **55**(36): p. 4998-5001.
4. Cotruvo, J.A. and Stubbe, J., *Class I ribonucleotide reductases: metallocofactor assembly and repair in vitro and in vivo.* Annu. Rev. Biochem., 2011. **80**: p. 733-767.
5. Stubbe, J. and Seyedsayamdost, M.R., *Discovery of a New Class I Ribonucleotide Reductase with an Essential DOPA Radical and NO Metal as an Initiator of Long-Range Radical Transfer*. Biochemistry, 2019. **58**(6): p. 435-437.
6. Cotruvo, J.A., Jr. and Stubbe, J., *An active dimanganese(III)-tyrosyl radical cofactor in Escherichia coli class Ib ribonucleotide reductase.* Biochemistry, 2010. **49**(6): p. 1297-1309.

7. Boal, A.K., Cotruvo, J.A., Stubbe, J., and Rosenzweig, A.C., *Structural Basis for Activation of Class Ib Ribonucleotide Reductase.* Science, 2010. **329**(5998): p. 1526-1530.
8. Rayner-Canham, G. and Overton, T., *Descriptive inorganic chemistry*. Sixth edition. 2014, New York: W.H. Freeman and Company, a Macmillan Higher Education Company. 1 volume.
9. Dempsey, J.L., Winkler, J.R., and Gray, H.B., *Proton-Coupled Electron Flow in Protein Redox Machines.* Chem. Rev., 2010. **110**(12): p. 7024-7039.
10. Ichiye, T., *Electron Transfer Proteins: Overview*, in *Encyclopedia of Biophysics*, G.C.K. Roberts, Editor. 2013, Springer: Berlin Heidelberg. p. 614-621.
11. Tymoczko, J.L., Berg, J.M., and Stryer, L., *Biochemistry, a short course*. Third ed. 2015, New York: W.H. Freeman & Company, a Macmillan Education imprint. 1 volume.
12. Bashir, Q., Scanu, S., and Ubbink, M., *Dynamics in electron transfer protein complexes.* FEBS J., 2011. **278**(9): p. 1391-1400.
13. Li, W., Baldus, I.B., and Gräter, F., *Redox Potentials of Protein Disulfide Bonds from Free-Energy Calculations.* J. Phys, Chem. B, 2015. **119**(17): p. 5386-5391.
14. Page, C.C., Moser, C.C., and Dutton, P.L., *Mechanism for electron transfer within and between proteins.* Curr. Opin. Chem. Biol., 2003. **7**(5): p. 551-556.
15. Prabhulkar, S., Tian, H., Wang, X., Zhu, J.J., and Li, C.Z., *Engineered proteins: redox properties and their applications.* Antioxid. Redox Signal., 2012. **17**(12): p. 1796-1822.
16. Gudim, I., Hammerstad, M., Lofstad, M., and Hersleth, H.P., *The Characterization of Different Flavodoxin Reductase-Flavodoxin (FNR-Fld) Interactions Reveals an Efficient FNR-Fld Redox Pair and Identifies a Novel FNR Subclass.* Biochemistry, 2018. **57**(37): p. 5427-5436.
17. McLendon, G. and Hake, R., *Interprotein electron transfer.* Chem. Rev., 1992. **92**(3): p. 481-490.
18. Marcus, R.A. and Sutin, N., *Electron transfers in chemistry and biology.* Biochim. Biophys. Acta, Rev. Bioenerg., 1985. **811**(3): p. 265-322.
19. Joosten, V. and van Berkel, W.J.H., *Flavoenzymes.* Curr. Opin. Chem. Biol., 2007. **11**(2): p. 195-202.
20. Kao, Y.T., Saxena, C., He, T.F., Guo, L., Wang, L., Sancar, A., and Zhong, D., *Ultrafast dynamics of flavins in five redox states.* J. Am. Chem. Soc., 2008. **130**(39): p. 13132-13139.
21. Macheroux, P., Kappes, B., and Ealick, S.E., *Flavogenomics--a genomic and structural view of flavin-dependent proteins.* FEBS J., 2011. **278**(15): p. 2625-2634.
22. Hammerstad, M. and Hersleth, H.-P., *Overview of structurally homologous flavoprotein oxidoreductases containing the low Mr thioredoxin reductase-like fold – A functionally diverse group.* Arch. Biochem. Biophys., 2021. **702**: 108826.

23. Leys, D. and Scrutton, N.S., *Sweating the assets of flavin cofactors: new insight of chemical versatility from knowledge of structure and mechanism.* Curr. Opin. Struc. Biol, 2016. **41**: p. 19-26.
24. Sancho, J., *Flavodoxins: sequence, folding, binding, function and beyond.* Cell. Mol. Life. Sci., 2006. **63**(7-8): p. 855-864.
25. Chowdhury, N.P., Klomann, K., Seubert, A., and Buckel, W., *Reduction of Flavodoxin by Electron Bifurcation and Sodium Ion-dependent Reoxidation by NAD+ Catalyzed by Ferredoxin-NAD+ Reductase (Rnf)*.* J. Biol. Chem., 2016. **291**(23): p. 11993-12002.
26. Pierella Karlusich, J.J. and Carrillo, N., *Evolution of the acceptor side of photosystem I: ferredoxin, flavodoxin, and ferredoxin-NADP+ oxidoreductase.* Photosynth. Res., 2017. **134**(3): p. 235-250.
27. Aliverti, A., Pandini, V., Pennati, A., de Rosa, M., and Zanetti, G., *Structural and functional diversity of ferredoxin-NADP(+) reductases.* Arch. Biochem. Biophys., 2008. **474**(2): p. 283-291.
28. Komori, H., Seo, D., Sakurai, T., and Higuchi, Y., *Crystal structure analysis of Bacillus subtilis ferredoxin-NADP(+) oxidoreductase and the structural basis for its substrate selectivity.* Protein Sci., 2010. **19**(12): p. 2279-2290.
29. Seo, D., Okabe, S., Yanase, M., Kataoka, K., and Sakurai, T., *Studies of interaction of homo-dimeric ferredoxin-NAD(P)+ oxidoreductases of Bacillus subtilis and Rhodopseudomonas palustris, that are closely related to thioredoxin reductases in amino acid sequence, with ferredoxins and pyridine nucleotide coenzymes.* Biochim. Biophys. Acta, Proteins Proteomics, 2009. **1794**(4): p. 594-601.
30. Seo, D., Soeta, T., Sakurai, H., Sétif, P., and Sakurai, T., *Pre-steady-state kinetic studies of redox reactions catalysed by Bacillus subtilis ferredoxin-NADP+ oxidoreductase with NADP+/NADPH and ferredoxin.* Biochim. Biophys. Acta, Bioenerg., 2016. **1857**(6): p. 678-687.
31. Hammerstad, M., Gudim, I., and Hersleth, H.-P., *The Crystal Structures of Bacillithiol Disulfide Reductase Bdr (YpdA) Provide Structural and Functional Insight into a New Type of FAD-Containing NADPH-Dependent Oxidoreductase.* Biochemistry, 2020. **59**(51): p. 4793-4798.
32. Lennon, B.W., Williams, C.H., and Ludwig, M.L., *Twists in Catalysis: Alternating Conformations of Escherichia coli Thioredoxin Reductase.* Science, 2000. **289**(5482): p. 1190-1194.
33. Mulrooney, S.B. and Williams, C.H., *Evidence for two conformational states of thioredoxin reductase from Escherichia coli: Use of intrinsic and extrinsic quenchers of flavin fluorescence as probes to observe domain rotation.* Protein Sci., 2008. **6**(10): p. 2188-2195.

34. Moser, C.C., Anderson, J.L.R., and Dutton, P.L., *Guidelines for tunneling in enzymes.* Biochim. Biophys. Acta, Bioenerg., 2010. **1797**(9): p. 1573-1586.
35. Muraki, N., Seo, D., Shiba, T., Sakurai, T., and Kurisu, G., *Asymmetric Dimeric Structure of Ferredoxin-NAD(P)+ Oxidoreductase from the Green Sulfur Bacterium Chlorobaculum tepidum: Implications for Binding Ferredoxin and NADP+*. J. Mol. Biol., 2010. **401**(3): p. 403-414.
36. Brown, T.A., *Gene Cloning and DNA Analysis: An Introduction*. 2016, Somerset: John Wiley & Sons. 353 p.
37. Clark, D.P., Pazdernik, N.J., and McGehee, M.R., *Chapter 23 - Plasmids*, in *Molecular Biology (Third Edition)*, D.P. Clark, N.J. Pazdernik, and M.R. McGehee, Editors. 2019, Academic Cell. p. 712-748.
38. Drlica, K. and Gennaro, M.L., *Plasmids*, in *Encyclopedia of Genetics*, S. Brenner and J.H. Miller, Editors. 2001, Academic Press: New York. p. 1485-1490.
39. Davis, L.G., Dibner, M.D., and Battey, J.F., *SECTION 5-4 - Restriction Endonucleases (REs) and Their Use*, in *Basic Methods in Molecular Biology*, L.G. Davis, M.D. Dibner, and J.F. Battey, Editors. 1986, Elsevier. p. 51-57.
40. Lodish, H.F., *Molecular cell biology*. 4th ed. 2000, New York: W.H. Freeman. xxxix, 1084 p.
41. Redondo-Salvo, S., Fernández-López, R., Ruiz, R., Vielva, L., de Toro, M., Rocha, E.P.C., Garcillán-Barcia, M.P., and de la Cruz, F., *Pathways for horizontal gene transfer in bacteria revealed by a global map of their plasmids.* Nat. Commun., 2020. **11**(1): 3602.
42. Chen, I. and Dubnau, D., *DNA uptake during bacterial transformation.* Nat. Rev. Microbiol., 2004. **2**(3): p. 241-249.
43. Johnston, C., Martin, B., Fichant, G., Polard, P., and Claverys, J.-P., *Bacterial transformation: distribution, shared mechanisms and divergent control.* Nat. Rev. Microbiol., 2014. **12**(3): p. 181-196.
44. Tabor, S., *Expression using the T7 RNA polymerase/promoter system.* Curr. Protoc. Mol. Biol., 2001. Chapter 16: Unit 16.2.
45. Angius, F., Ilioaia, O., Amrani, A., Suisse, A., Rosset, L., Legrand, A., Abou-Hamdan, A., Uzan, M., Zito, F., and Miroux, B., *A novel regulation mechanism of the T7 RNA polymerase based expression system improves overproduction and folding of membrane proteins.* Sci. Rep., 2018. **8**(1): 8572.
46. Studier, F.W. and Moffatt, B.A., *Use of bacteriophage T7 RNA polymerase to direct selective high-level expression of cloned genes.* J. Mol. Biol., 1986. **189**(1): p. 113-130.
47. Saranya, N., Devi, P., Nithiyanantham, S., and Jeyalaxmi, R., *Cells Disruption by Ultrasonication.* Bio. NanoSci,, 2014. **4**(4): p. 335-337.

48. Duong-Ly, K.C. and Gabelli, S.B., *Chapter Seven - Salting out of Proteins Using Ammonium Sulfate Precipitation*, in *Methods in Enzymology*, J. Lorsch, Editor. 2014, Academic Press. p. 85-94.
49. Wingfield, P., *Protein precipitation using ammonium sulfate.* Curr. Protoc. Protein Sci., 2016. **84**(1): A.3F.1-A.3F.9.
50. Sheehan, D., *Physical biochemistry : principles and applications*. 2nd ed. 2009, Chichester, UK ; Hoboken, NJ: Wiley-Blackwell. xiv, 407 p.
51. Pringels, L., Broeckx, V., Boonen, K., Landuyt, B., and Schoofs, L., *Abundant plasma protein depletion using ammonium sulfate precipitation and Protein A affinity chromatography.* J. Chromatogr. B, 2018. **1089**: p. 43-59.
52. Coskun, O., *Separation techniques: Chromatography.* North. Clin. Istanb., 2016. **3**(2): p. 156-160.
53. Jungbauer, A. and Hahn, R., *Chapter 22 Ion-Exchange Chromatography*, in *Methods in Enzymology*, R.R. Burgess and M.P. Deutscher, Editors. 2009, Academic Press. p. 349-371.
54. Ó'Fágáin, C., Cummins, P.M., and O'Connor, B.F., *Gel-Filtration Chromatography*, in *Protein Chromatography: Methods and Protocols*, D. Walls and S.T. Loughran, Editors. 2017, Springer New York: New York, NY. p. 15-25.
55. Nowakowski, A.B., Wobig, W.J., and Petering, D.H., *Native SDS-PAGE: high resolution electrophoretic separation of proteins with retention of native properties including bound metal ions.* Metallomics, 2014. **6**(5): p. 1068-1078.
56. Au - Fiala, G.J., Au - Schamel, W.W.A., and Au - Blumenthal, B., *Blue Native Polyacrylamide Gel Electrophoresis (BN-PAGE) for Analysis of Multiprotein Complexes from Cellular Lysates.* JoVE, 2011(48): e2164.
57. Wittig, I., Braun, H.-P., and Schägger, H., *Blue native PAGE.* Nat. Protoc., 2006. **1**(1): p. 418-428.
58. McPherson, A. and Gavira, J.A., *Introduction to protein crystallization.* Acta Crystallogr. F Struct. Biol. Commun., 2014. **70**(1): p. 2-20.
59. Asherie, N., *Protein crystallization and phase diagrams.* Methods, 2004. **34**(3): p. 266-272.
60. Chayen, N.E. and Saridakis, E., *Protein crystallization: from purified protein to diffraction-quality crystal.* Nat. Methods, 2008. **5**(2): p. 147-153.
61. Forsythe, E.L., Maxwell, D.L., and Pusey, M., *Vapor diffusion, nucleation rates and the reservoir to crystallization volume ratio.* Acta Crystallogr. D, 2002. **58**(10-1): p. 1601-1605.
62. Russo Krauss, I., Merlino, A., Vergara, A., and Sica, F., *An overview of biological macromolecule crystallization.* Int. J. Mol. Sci., 2013. **14**(6): p. 11643-11691.
63. Alberts, B., *Molecular biology of the cell*. 4th ed. 2002, New York: Garland Science. xxxiv, 1548 p.

64. Slabinski, L., Jaroszewski, L., Rodrigues, A.P., Rychlewski, L., Wilson, I.A., Lesley, S.A., and Godzik, A., *The challenge of protein structure determination--lessons from structural genomics.* Protein Sci., 2007. **16**(11): p. 2472-2482.
65. Wlodawer, A., Minor, W., Dauter, Z., and Jaskolski, M., *Protein crystallography for aspiring crystallographers or how to avoid pitfalls and traps in macromolecular structure determination.* FEBS J., 2013. **280**(22): p. 5705-5736.
66. Balerna, A. and Mobilio, S., *Introduction to Synchrotron Radiation*, in *Synchrotron Radiation: Basics, Methods and Applications*, S. Mobilio, F. Boscherini, and C. Meneghini, Editors. 2015, Springer: Berlin Heidelberg. p. 3-28.
67. De Graef, M., *Basic quantum mechanics, Bragg's Law and other tools*, in *Introduction to Conventional Transmission Electron Microscopy*, M. De Graef, Editor. 2003, Cambridge University Press: Cambridge. p. 79-135.
68. Powell, Harold R., *X-ray data processing.* Biosci. Rep., 2017. **37**(5).
69. Kabsch, W., *XDS.* Acta Crystallogr. D Biol. Crystallogr., 2010. **66**(2): p. 125-132.
70. Winn, M.D., Ballard, C.C., Cowtan, K.D., Dodson, E.J., Emsley, P., Evans, P.R., Keegan, R.M., Krissinel, E.B., Leslie, A.G., McCoy, A., McNicholas, S.J., Murshudov, G.N., Pannu, N.S., Potterton, E.A., Powell, H.R., Read, R.J., Vagin, A., and Wilson, K.S., *Overview of the CCP4 suite and current developments.* Acta Crystallogr. D Biol. Crystallogr., 2011. **67**(4): p. 235-242.
71. Mccoy, A., Grosse-Kunstleve, R.W., Adams, P., Winn, M., Storoni, L.C., and Read, R., *Phaser crystallographic software.* J. Appl. Crystallogr., 2007. **40**: p. 658 - 674.
72. Atkins, P.W. and De Paula, J., *Atkins' Physical chemistry*. Tenth ed. 2014, Oxford: Oxford University Press. xxv, 1008 p.
73. Brøndsted Nielsen, S. and Wyer, J.A., *Photophysics of Ionic Biochromophores*, in *Physical Chemistry in Action*,. 2013: Springer: Berlin Heidelberg.
74. Berg, J.M., Tymoczko, J.L., and Stryer, L., *Biochemistry*. 5th ed. 2002, New York: Freeman. 1100 p.
75. Robinson, P.K., *Enzymes: principles and biotechnological applications.* Essays Biochem, 2015. **59**: p. 1-41.
76. Magnusson, A.O., Szekrenyi, A., Joosten, H.J., Finnigan, J., Charnock, S., and Fessner, W.D., *nanoDSF as screening tool for enzyme libraries and biotechnology development.* FEBS J., 2019. **286**(1): p. 184-204.
77. McPherson, A. and Cudney, B., *Optimization of crystallization conditions for biological macromolecules.* Acta Crystallogr. F Struct. Biol. Commun., 2014. **70**(Pt 11): p. 1445-67.
78. Bergfors, T., *Succeeding with seeding: some practical advice*. 2007, Springer Netherlands. p. 1-10.

79. Murshudov, G.N., Skubák, P., Lebedev, A.A., Pannu, N.S., Steiner, R.A., Nicholls, R.A., Winn, M.D., Long, F., and Vagin, A.A., *REFMAC5 for the refinement of macromolecular crystal structures.* Acta Crystallogr. D Biol. Crystallogr., 2011. **67**(4): p. 355-367.
80. Emsley, P., Lohkamp, B., Scott, W.G., and Cowtan, K., *Features and development of Coot.* Acta Crystallogr. D Biol. Crystallogr., 2010. **66**(4): p. 486-501.
81. Liebschner, D., Afonine, P.V., Moriarty, N.W., Poon, B.K., Sobolev, O.V., Terwilliger, T.C., and Adams, P.D., *Polder maps: improving OMIT maps by excluding bulk solvent.* Acta Crystallogr. D Struct. Biol., 2017. **73**(2): p. 148-157.